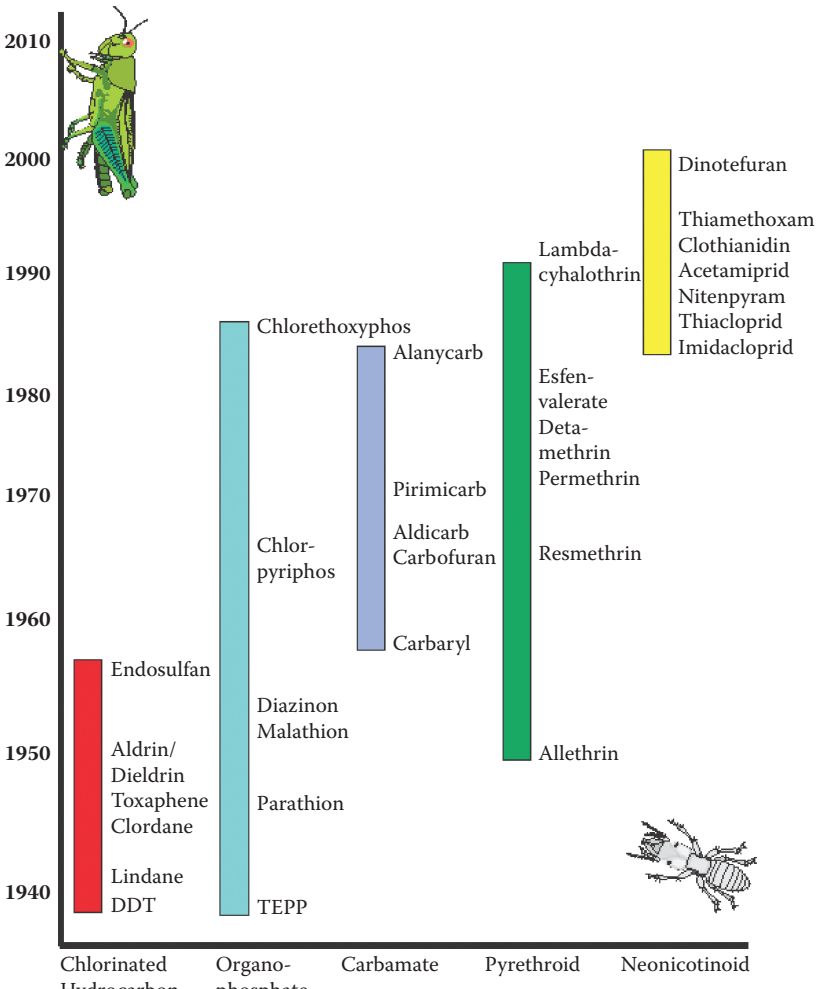

Figure 1.1 The general development chronology of the five major types of organic insecticides. The information in this figure was derived from Casida and Quistad (1998) (Figure 1), Jeschke and Nauen (2008), and Jeschke et al. (2011). The neonicotinoids are plotted with patent year, i.e., imidaclopid (1985), thiaclopid (1985), nitenpyram (1988), acetamiprid (1989), thiamethoxam (1992), and dinotefuran (1994).

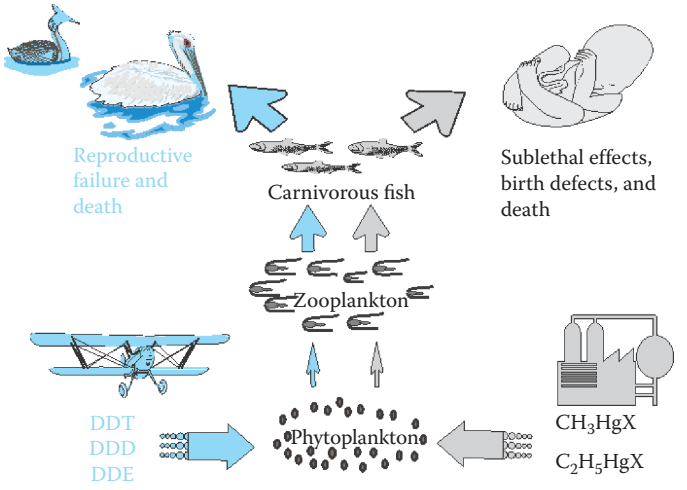

Figure 1.2 Two of the first pollutants to draw attention to the inadequacies of the dilution paradigm were DDT and methylmercury. They accelerated the emergence of the boomerang paradigm. Both chemicals were returned to humans or to valued wildlife species by transfer through food webs.

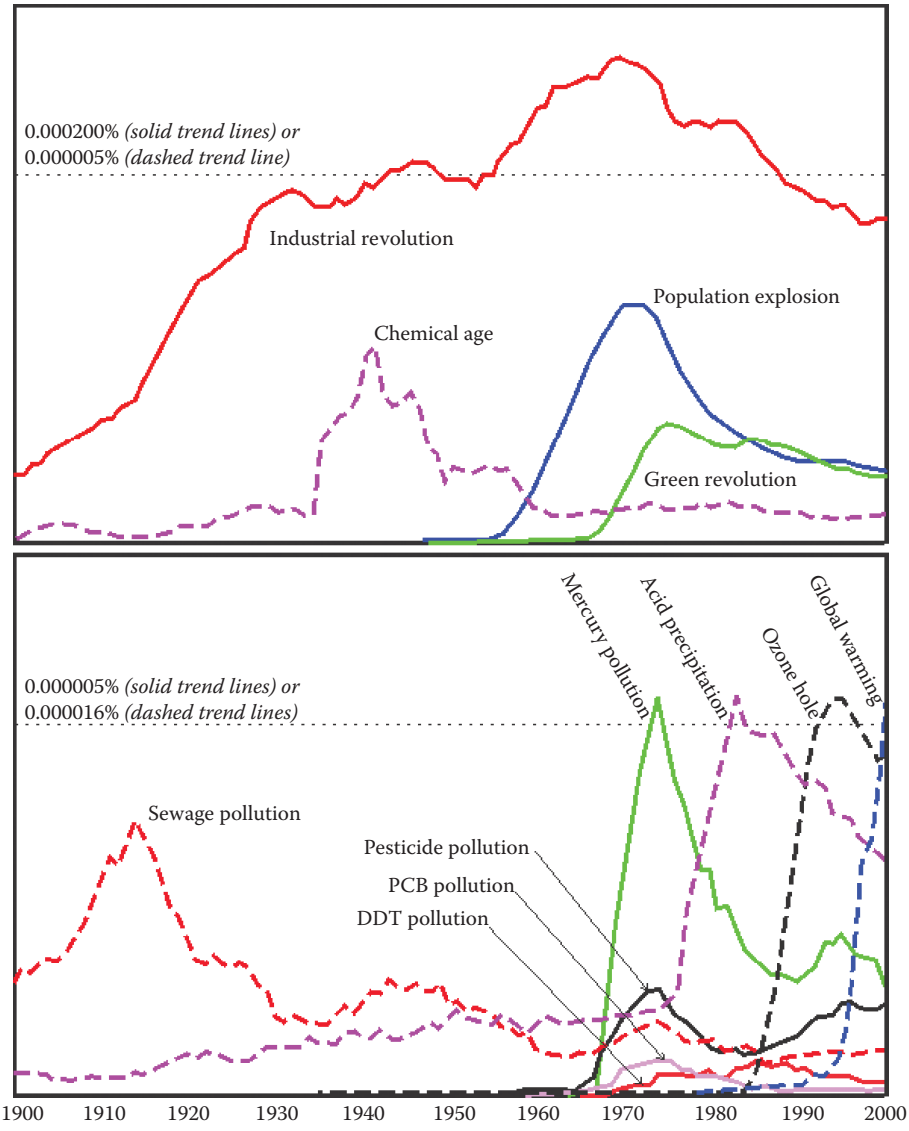

Figure 1.3 Results of an NGram analysis of several bigrams relevant to ecotoxicology. The top panel is the prevalence of bigrams related to social trends that were found in the millions of English books scanned to date by Google (see ngrams.googlelabs.com). The vertical axis reflects the occurrence of the bigram as a proportion of all of the bigrams in these books. The bottom panel depicts the same for bigrams related to impacts of environmental pollution. Clearly, a sequence of events occurring in the twentieth century established an awareness of a sequence of pollution types. An important theme to note is the expending scale for each in the temporal sequence of pollution types. For example, sewage pollution was usually associated with a water body. The more recent pollution types, e.g., the ozone hole or global warming, encompass scales of a continent and the entire biosphere. (Modified from Figure 8.1 in Newman, M. C., *Quantitative Ecotoxicology,* 2nd Edition, Taylor & Francis/CRC Press, Boca Raton, FL, 2013.)

Figure 1.4 Pervasive metal contamination exists in Poland's Olkusz mining region. Lead and zinc have been mined here since the medieval ages; however, industrial activities surged through the 1960s and 1970s in a manner typical of the times. Similar, widespread metal contamination was produced around the Avonmouth (UK), Gusum (north Sweden), Copperhill (Tennessee), and Flin Flon (Canada) smelters. In the early 1980s, releases at the Polish mining region decreased as production demand abated, and modern electrofilters and scrubbers were installed (top panel). (See Łagisz et al. [2002], Stone et al. [2001, 2002], and Niklińska et al. [2006] for details about ecotoxicological consequences.)

Figure 1.5 Mercury being used to extract gold from ore mined in Portovelo, Ecuador (June 2007). Pulverized ore is agitated with a puddle of mercury (arrows) to form a gold–mercury amalgam, which in this picture, is being placed into a piece of cloth. Mercury is hand-squeezed from the amalgam and remaining mercury is driven off by heating with a propane torch. This process results in substantial human exposure and mercury release into the environment. (Note that the person wringing the mercury from the amalgam has a silver bracelet into which the mercury will also readily dissolve to form a silver–mercury amalgam.) (Courtesy of Lane, K., College of William & Mary.)

Figure 1.6 Kuwaiti oil wells set afire by Iraqi troops as seen from a U.S. space shuttle flight. Oil wells are seen burning north of the Bay of Kuwait and immediately south of Kuwait City. (Courtesy of NASA.)

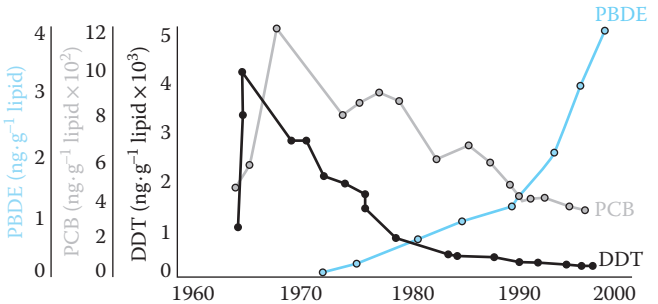

Figure 1.7 Trends in three persistent organic pollutants (POPs) in Swedish breast milk. DDT was banned in Sweden in the early 1970s, and accordingly, concentrations drop through the decades after peaking in the mid-1960s. A less obvious decline is seen for polychlorinated biphenyl (PCB) concentrations, resulting in continued concern about adverse PCB effects on humans and wildlife. Concentrations of brominated POPs used as fire retardants (polybrominated diphenyl ethers [PBDE]) increased rapidly through the decades; however, considerable effort is now being spent in the European Union to move away from PBDE use (Birnbaum and Staskal, 2004; Betts, 2007; Blum, 2007). Note that the scales for DDT, PCB, and PBDE are $ng{\cdot}g^{-1}$ of milk lipid $\times 10^3$, $\times 10^2$, and $\times 10^0$, respectively. (Data extracted from Figures 3, 9, and 11 in Solomon, G. M. and Weiss, P. M., *Environ. Health Perspec.*, 110, A339–A347, 2002.)

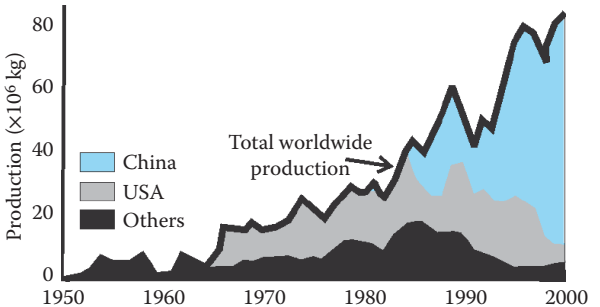

Figure 1.8 China's rapid rise to dominance in rare earth element production (redrawn from Figure 1 of the USGS Fact Sheet 087-02 [USGS, 2002]). These elements are essential components of modern color television screens, liquid-crystal displays of computer screens, optical networks, glass polish systems, and magnet technologies.

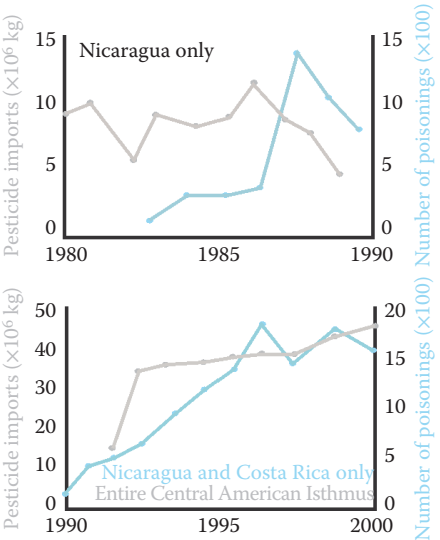

Figure 1.9 Pesticide use and effects in Central American countries. Exemplary of trends during the 1980s are those shown in the top panel for Nicaragua (from Figure 3-3 and Table 4-3 of Murray [1994].) The bottom panel depicts the same themes today of increasing pesticide importation into the Central American isthmus (Pan American Health Organization, 2002) and consequent acute human poisoning, e.g., that for Costa Rica and Nicaragua. (From Wesseling, C. M. et al. *Toxicol. Appl. Pharm.*, 207, S697–S705, 2005.)

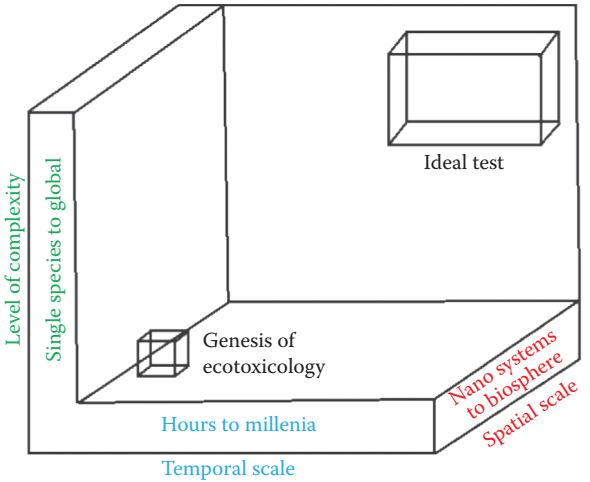

Figure 1.10 Schematic depiction of the genesis of ecotoxicology and the ideal goal about which one can,at present, only speculate. All three major components should be matched to the problem of interest to achieve the goal.

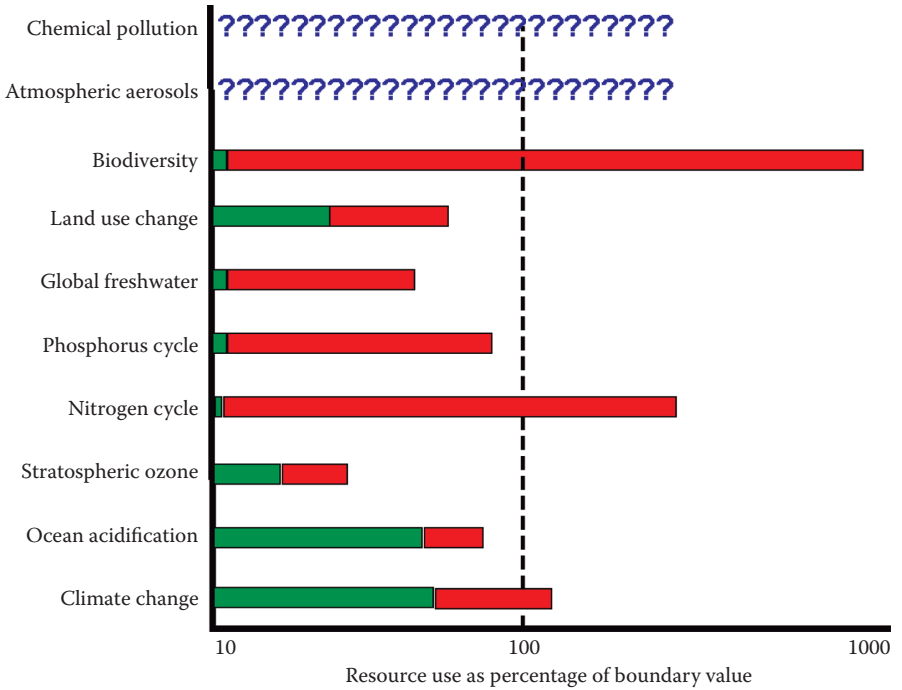

FIGURE 1.11 **Planetary boundary values** and estimates of preindustrial (green) and current values (red). Information extracted from Table S2 of Rockström et al. (2009b). According to these authors, humanity "has the freedom to pursue long-term social and economic development" only if these boundary values are not exceeded. Climate change units: carbon dioxide concentration; Ocean acidification: aragonite saturation ratio; Stratospheric ozone: ozone expressed in Dobson unit; Nitrogen cycle: Metric tonnes removed from the atmosphere for human use annually; Phosphorus cycle: Metric tonnes of flow into oceans annually; Global freshwater use: consumptive use of runoff as km^3 annually; Land use change: percentage of land cover converted to cropland; Biodiversity: number of species lost per million species annually.

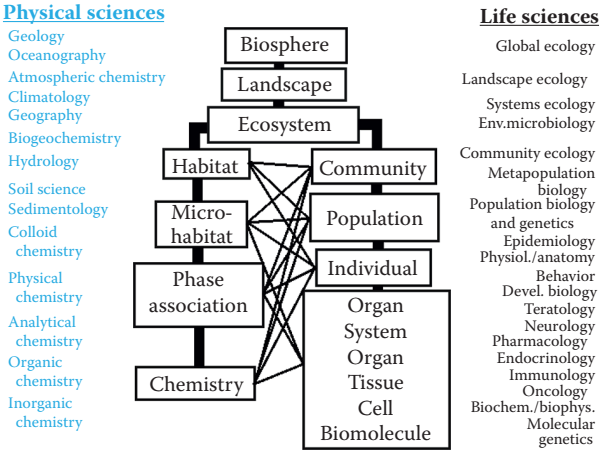

Figure 1.12 Hierarchical organization of topics addressed by ecotoxicology. Disciplines contributing to understanding abiotic interactions are listed on the left side of the diagram and those contributing to understanding biotic interactions are listed on the right. Important interactions, denoted by lines connecting components, occur between biotic and abiotic components.

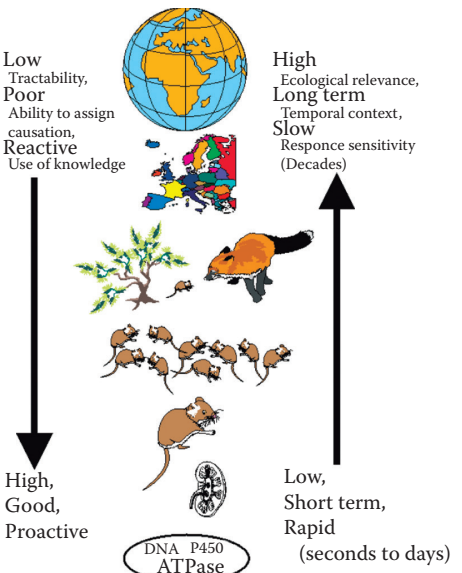

Figure 1.13 Hierarchical organization of topics in ecotoxicology relative to ecological relevance, general tractability, ability to assign causation, general use of knowledge, temporal context of consequence, and temporal sensitivity of response.

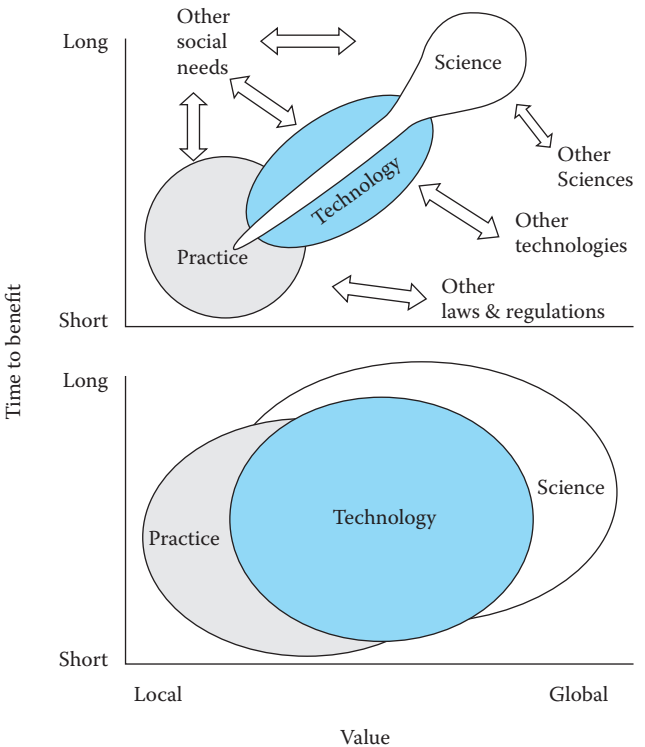

Figure 1.14 Present (top panel) and ideal (bottom panel) balance among scientific, technological, and practical components of ecotoxicology. The relative amount of effort in each is reflected by area on the plots of scale of value (local to global) and time to realize (short to long term) benefit from these components of the field.

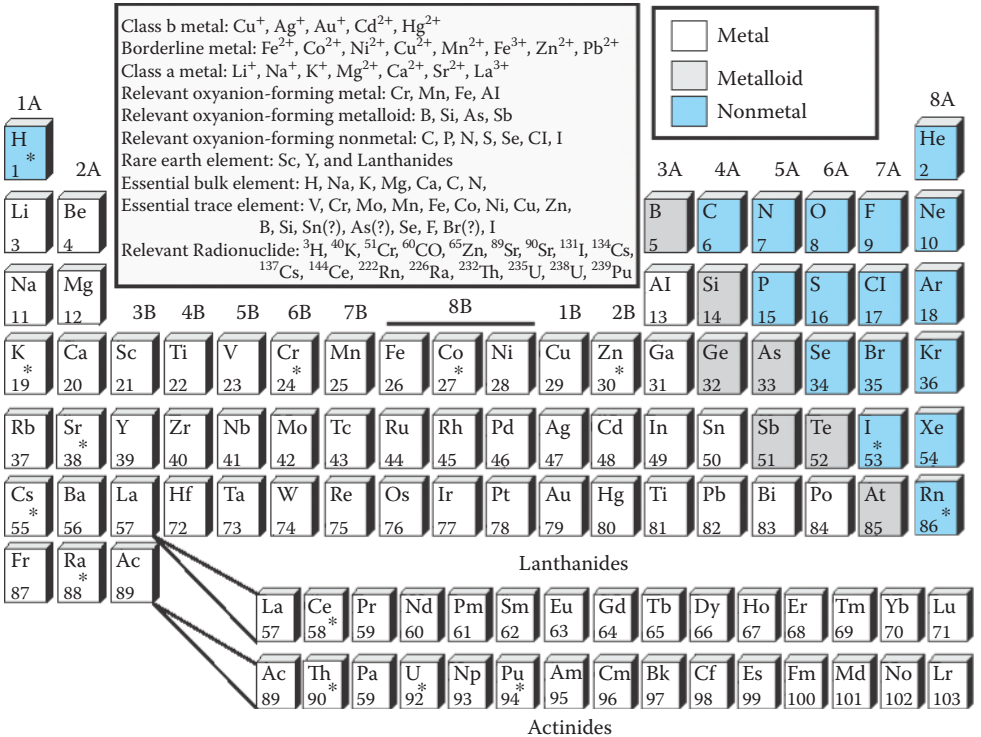

Figure 2.1 The periodic table is modified slightly here by the addition of an inset that highlights different clusters of elements relative to ecotoxicological features. The metals (white boxes) make up the majority of elements. The nonmetals (blue boxes) are fewer in number than the metals but include the major elements of life. The metalloids (gray boxes) have properties intermediate between the metals and nonmetals. Those elements for which environmentally relevant radioactive isotopes are discussed later in this chapter are indicated with an asterisk (*).

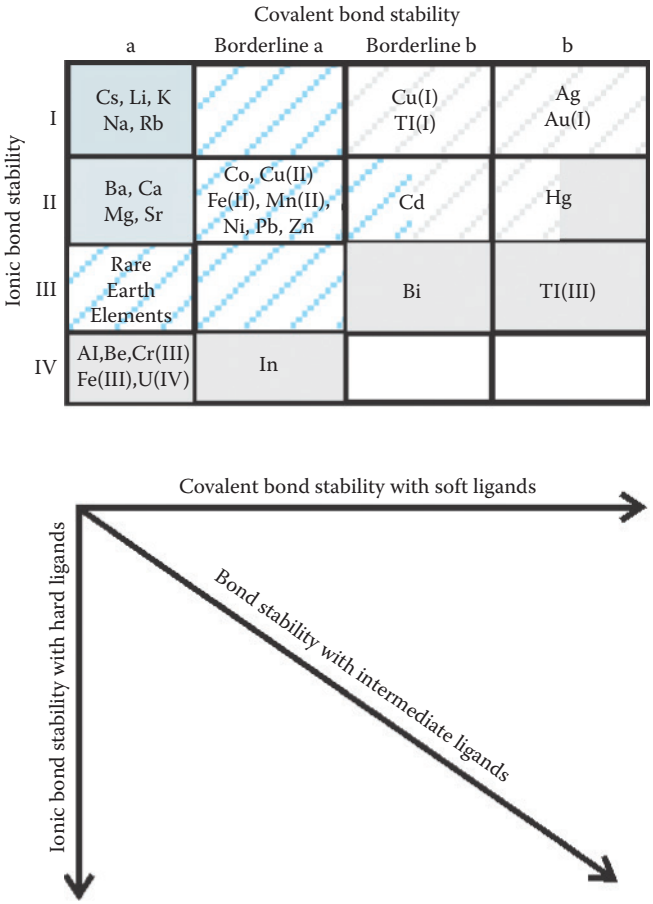

Figure 2.2 A modified complexation field diagram for cationic metals. The diagram is based on Figures 1 and 2 in Newman and Jagoe (1994), which, in turn, drew on Figure 12 and the associated text from Turner et al. (1981), which dealt with cation–ligand complexes in salt and fresh water bodies. The headings across the top refer to an element's Hard Soft Acid Base status and the I–IV down the right side of the diagram refer to single charged (I), double charged (II), triple charged (III), or hydrolysis-dominated (IV) cations. Roman numerals after an elemental symbol indicates the oxidation state if relevant. Solid blue, weakly complexed cation; striped blue, cations with widely variable complexation dependent on ionic conditions; striped gray, chloro-dominated cations; and solid gray, cations with hydrolysis-dominated complexation.

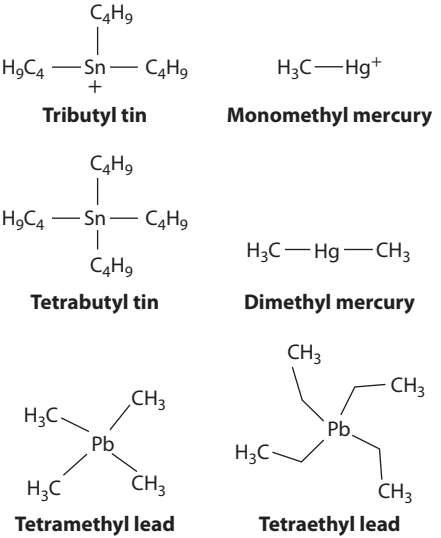

Figure 2.3 Chemical structures of the organometallic compounds that are currently of most concern to ecotoxicologists. Note that the four branches of the tetraethyl lead are C_2H_5.

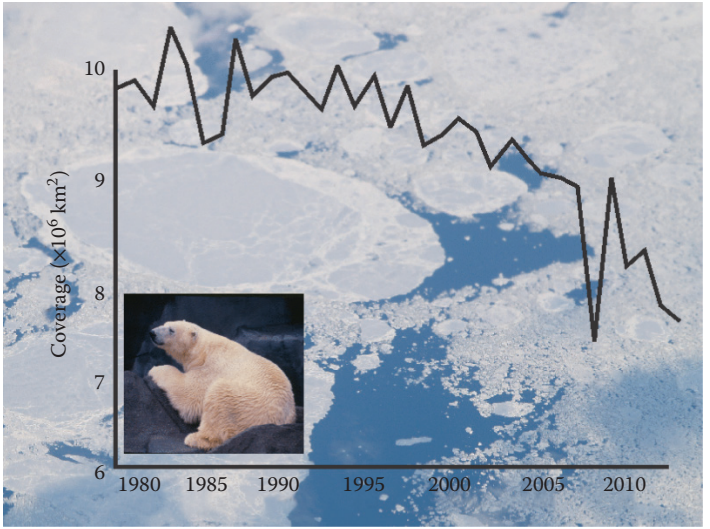

Figure 2.4 Decrease in October Arctic ice extent from 1979 to 2012 as documented by the U.S. National Snow and Ice Data Center (http://nsidc.org/arcticseaicenews/). The background photograph is pack ice in Ungava Bay of the Arctic Ocean (northeast Canada) as photographed on July 1, 2007 during a historically thin summer polar ice condition. Pack ice melt is normally slow until mid-July when it then accelerates in this part of the Arctic Ocean. Because feeding by polar bears on seals is strongly influenced by pack ice dynamics, scientist and Native American Inuit groups have begun to focus on potential impacts of global warming trends on the persistence of polar bear populations (Derocher et al. 2004; Wiig, 2005; Stirling and Parkinson, 2006). Some predictions indicate the potential for substantial thinning (Bluhm and Gradinger, 2008; Walsh, 2008) or even complete disappearance of summer ice (Kerr, 2007; Serreze et al. 2007; Stroeve et al. 2007). Like the penguins shown later in Figure 12.1, polar bears can accumulate high concentrations of persistent organic pollutants (Kumar et al. 2002), which suggests a complex situation exists for polar bears at this time. (Photograph by M. C. Newman.)

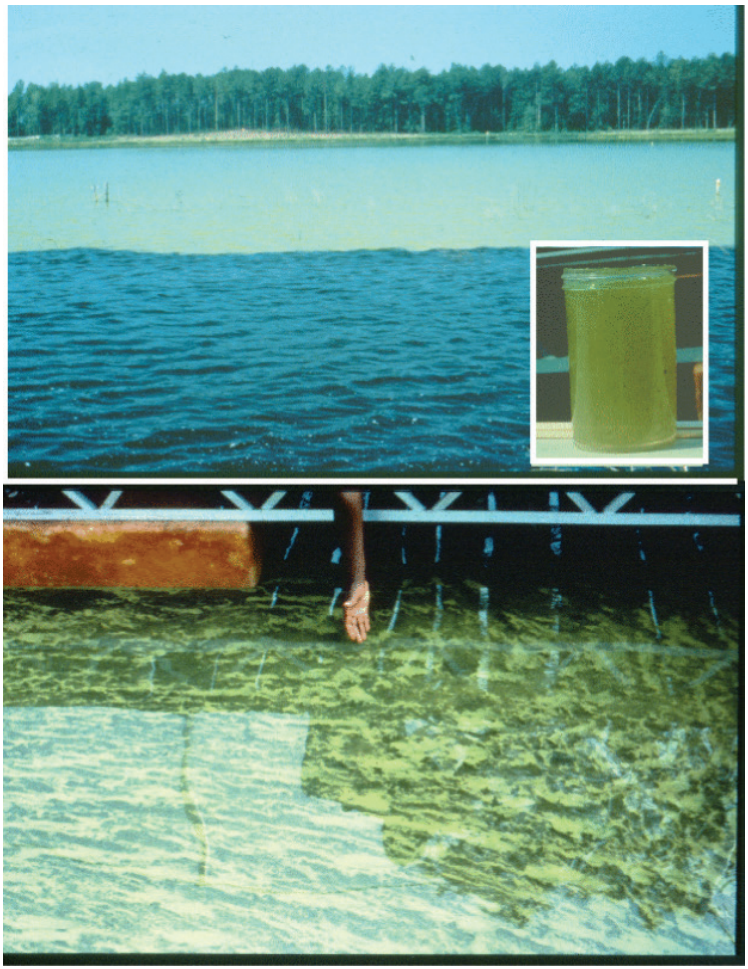

Figure 2.5 Blue-green algal bloom in a nuclear reactor cooling reservoir resulting from high phosphorus loadings. The top panel shows cool, nutrient-rich river water entering the lake from the reactor when nuclear production was stopped (foreground). The river water is cooler than the lake water so it sank below the resident lake water within a 100 m of the point of discharge. The lake water in the background is distinctly greener in color because of the dense blue-green algal growth realized after the nutrient-rich water was allowed to reside for a few days in the summer sunlight. The top panel inset and bottom panel are closer views of the dense blue-green algal growth.

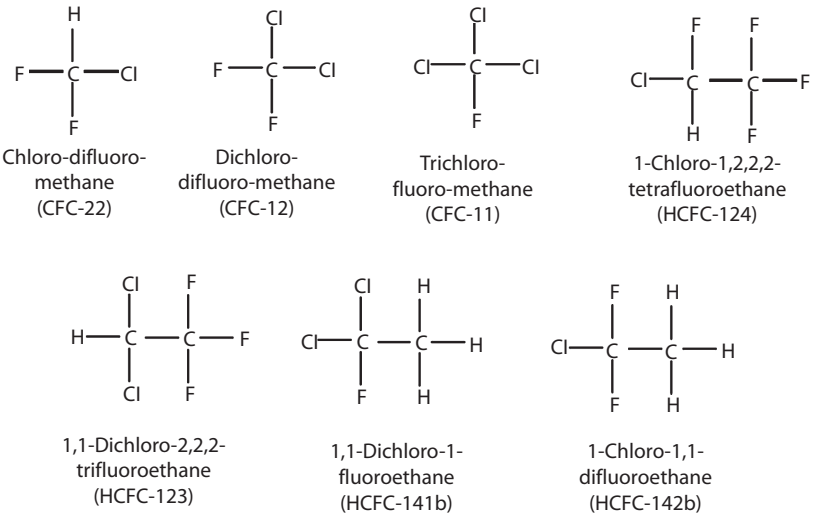

Figure 2.6 Examples of chlorofluorocarbons (CFCs) and hydrochlorofluorcarbons (HCFCs) including their commercial designations, e.g., CFC-22, which is also called R-22.

Figure 2.7 Two important organochlorine alkenes contributing to Dense, NonAqueous Phase Liquids (DNAPLs) contamination.

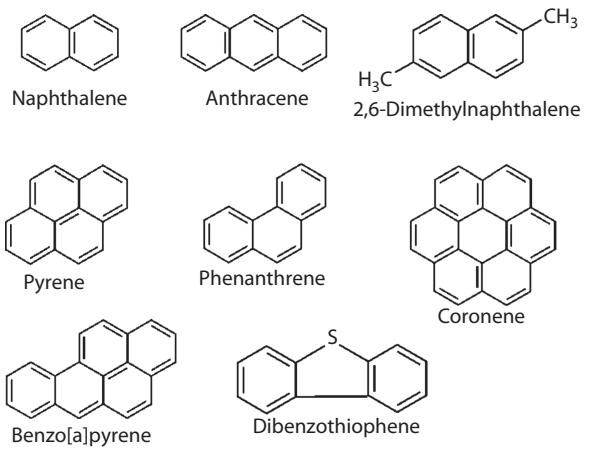

Figure 2.8 Examples of polycyclic aromatic hydrocarbons ranging from the two-ringed naphthalene to the seven-ringed coronene. These hydrocarbons can possess alkyl groups as shown for 2,6-dimethylnaphthalene. Although not a polycyclic aromatic hydrocarbon, the sulfur heterocyclic aromatic compound, dibenzothiophene, is also shown here because it commonly contributes to the aromatic hydrocarbon-related toxicity of spilt oils.

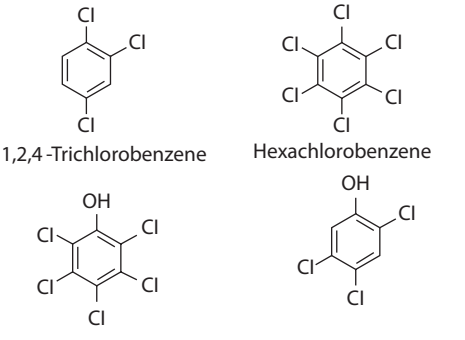

Figure 2.9 Examples of polychlorinated benzenes and phenols.

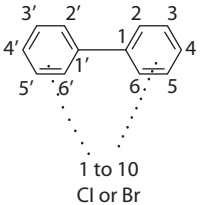

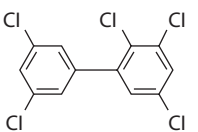

2,3,5,3′,5′-Pentachloro-biphenyl

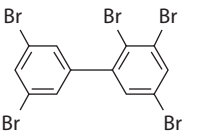

2,3,5,3′,5′-Pentabromo-biphenyl

Figure 2.10 The general structure of polychlorinated or polybrominated biphenyls is shown at the top of this figure. One to 10 of either chlorine or bromine atoms are placed along the two rings. Two examples are provided below this general structure.

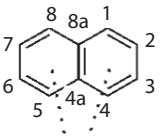

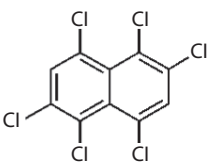

1,2,4,5,6,8-Hexachloronaphthalene

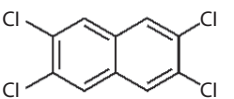

2,3,6,7-Tetrachloronaphthalene

Figure 2.11 The general structure of polychlorinated naphthalenes in which one to eight chlorine atoms are substituted into the molecule. Two examples of polychlorinated naphthalenes are also shown.

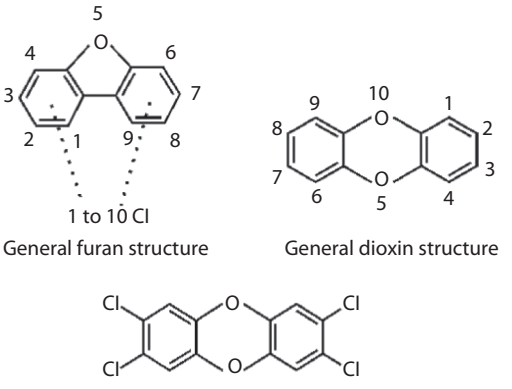

Figure 2.12 The general structures of polychlorinated dibenzofurans and dibenzodioxins. The dioxin shown (2,3,7,8-tetrachloro-dibenzo-p-dioxin) is one of the most toxic organic contaminants known and is often simply referred to as "dioxin" in regulatory and popular publications.

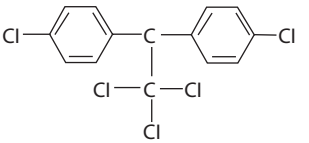

DDT

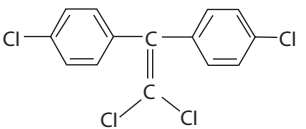

DDE

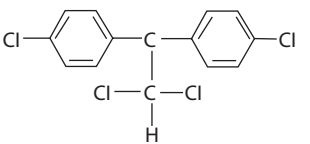

DDD

Figure 2.13 DDT and two closely related chlorinated contaminants with aromatic (diphenyl) and aliphatic (ethane or ethene) components.

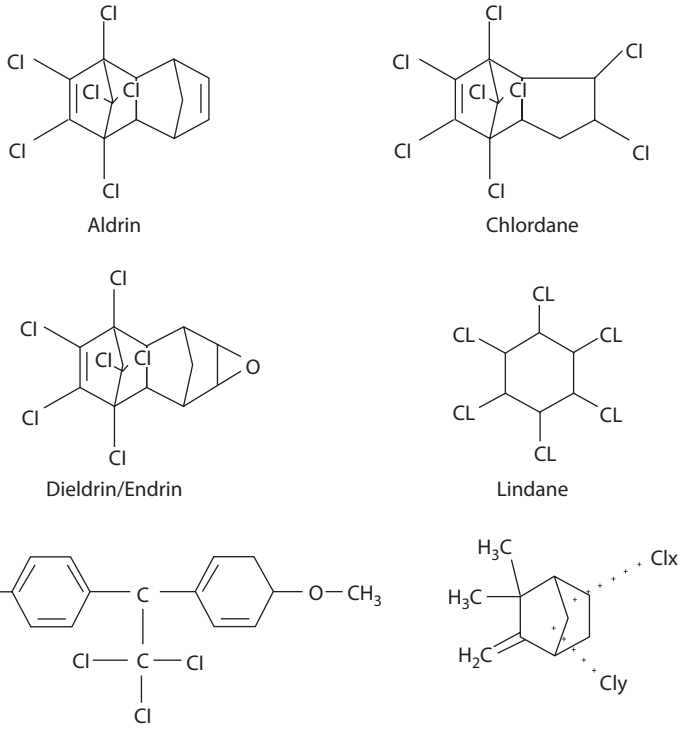

Figure 2.14 Seven prominent organochlorine pesticides including dieldrin and endrin, which are isomers of each other. Notice how similar the structure of methoxychlor is to that of dichlorodiphenyltrichloroethane. Toxaphene has different numbers of chlorine atoms attached to the ring shown on the plane of the page (x) and the ring extending upward from the plane of the page (y). Toxaphene (along with strobane) is a polychloroterpene insecticide. Aldrin and chlordane also are shown with rings flat on and perpendicular to the plane of the page. Note that the carbon ring of lindane is not an aromatic ring. For an organochlorine pesticide, lindane degrades relatively rapidly in the environment (Kennish, 1997). Note that these pesticides are actually used as mixtures of isomers.

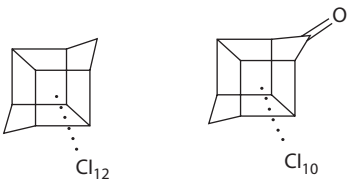

Figure 2.15 Two similar organochlorine pesticides, mirex (dodecachlorooctahydro-1,3,4-methano-1H-cyclobuta [cd]pentalene) and kepone (chlordecone).

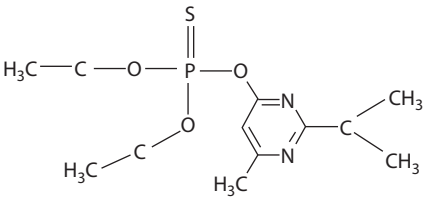

Diazinon

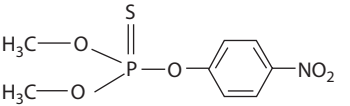

Methyl parathion

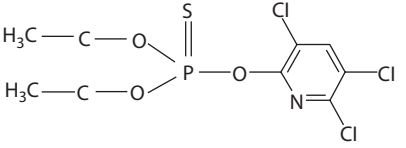

Chloryrifos

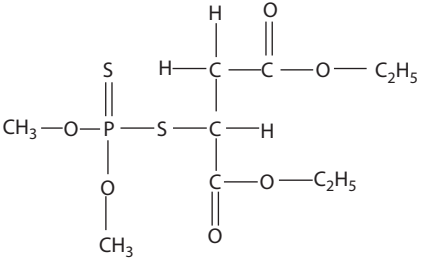

Malathion

Figure 2.16 Four common organophosphate pesticides.

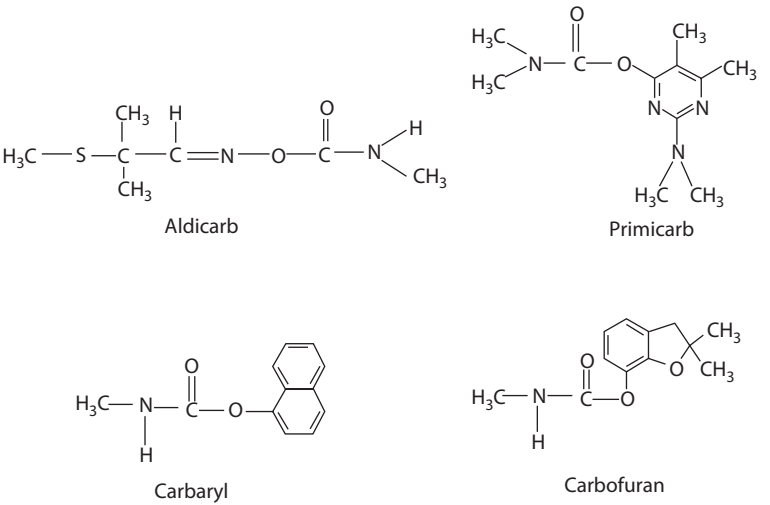

Figure 2.17 Representative carbamate pesticides including the widely used carbaryl (Sevin).

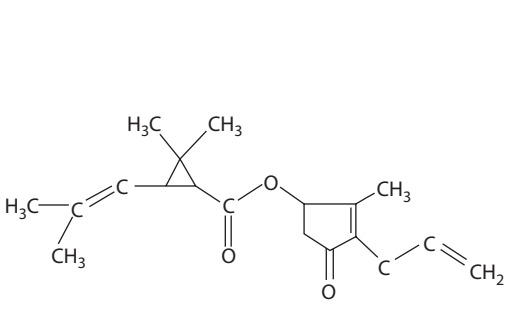

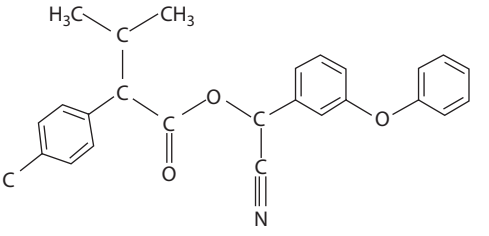

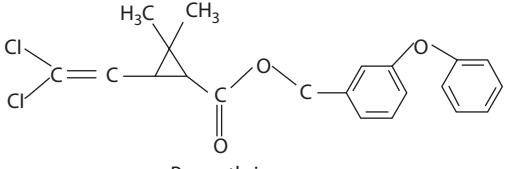

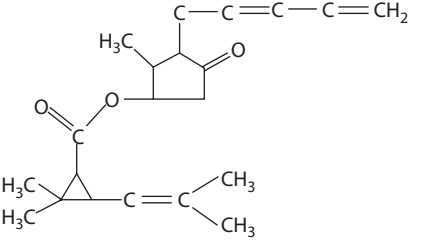

Figure 2.18 Representative pyrethrin (pyrethrin 1) and pyrethroid (allethrin, fenvalerate, and permethrin) pesticides. The cyano group in fenvalerate distinguishes it as a Type II pyrethroid and the absence of this group from allethrin and permethrin make them Type I pyrethroids.

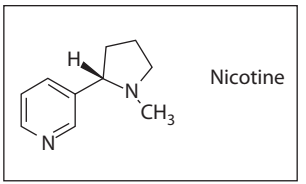

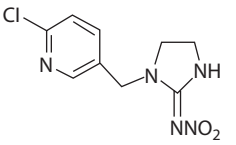

Imidacloprid

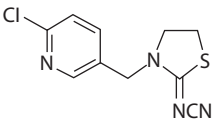

Thiacloprid

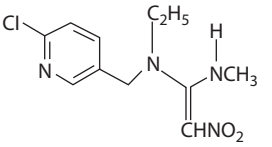

Nitenpyram

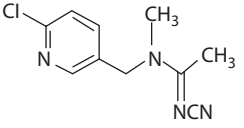

Acetamiprid

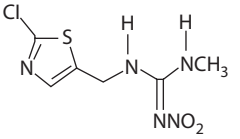

Clothianidin

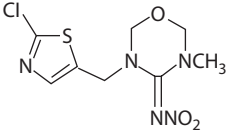

Thiamethoxam

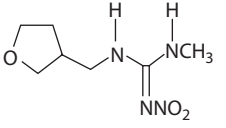

Dinotefuran

Figure 2.19 Members of the neonicotinoid class of pesticides are shown here in addition to the naturally produced nicotine molecule. The nicotine structure is shown boxed on the top left of the figure.

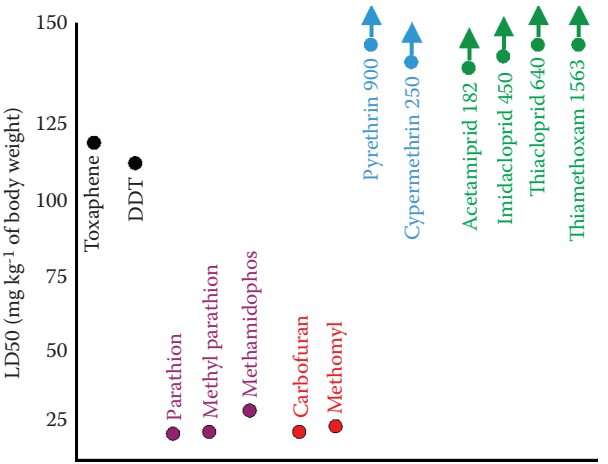

Figure 2.20 LD50 values for orally dosed rats. (Organochlorine [black], organophosphate [purple], and carbamate [red] pesticide data taken from Table of Murray [1994]; pyrethroid [blue] pesticide data taken from Kagabu [1997]; and neonicotinoid [green] pesticide data were obtained from Table 3 of Tomizawa and Casida [2005]. The actual LD50 values for the pyrethroid and neonicotinoid pesticides are given after the insecticide name. The arrow indicates an LD50 that is higher than the maximum value for the *y* axis.)

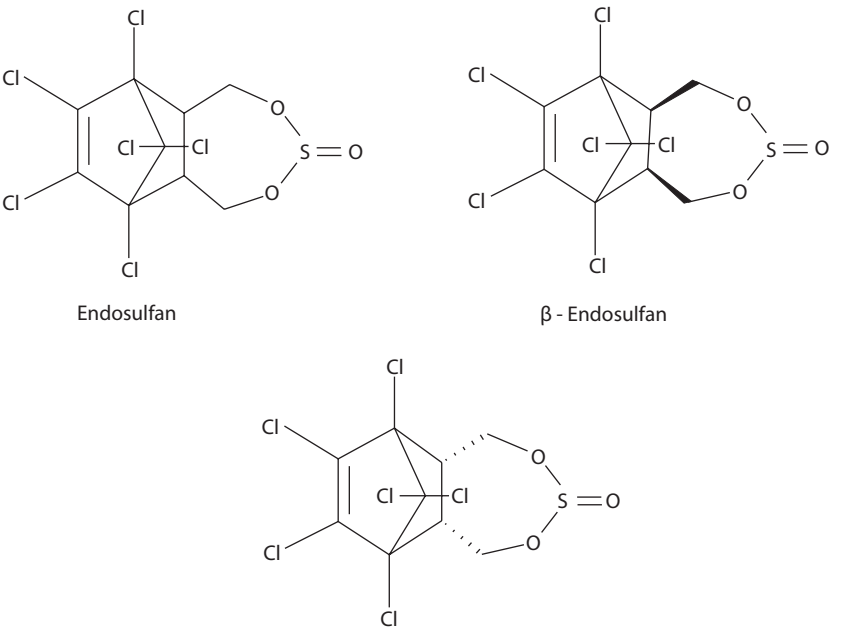

Figure 2.21 Molecular structures of endosulfan, α-endosulfan, and β-endosulfan.

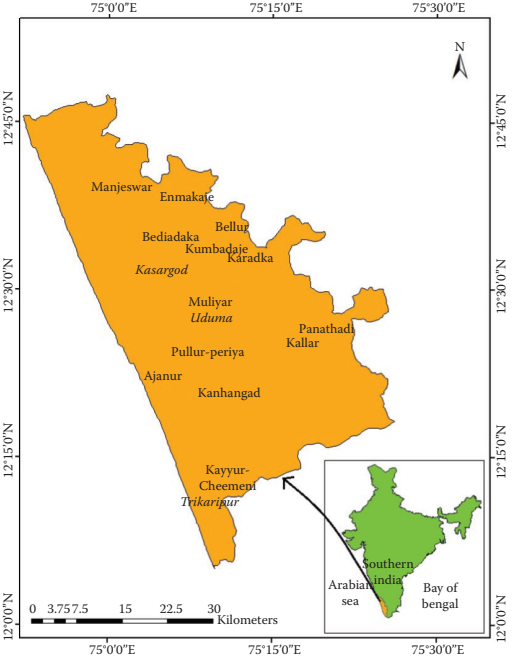

Figure 2.22 The endosulfan-impacted panchayaths of the Kasargod district of Kerala are shown in the left map. The map of southern India on the right shows the general location of Kerala in orange with the box around the general location of the Kasargod district. (Map of panchayaths modified from the Kerala State Council for Science, Technology and Environment report of monitoring of endosulfan residues in the panchayaths of Kasargod.)

Figure 2.23 Photographs of children from Kasargod affected by the aerial spraying of endosulfan. The young man was born with deformed hands and the young woman was born with what are called stag-horn hands and also a deformed leg. (Photographs reproduced with permission from the materials. Photographs of children in Kasargod living around plantations where endosulfan was sprayed for 24 years since 1976, developed and circulated by the Thanal Conservation Action and Information Network, Trivandrum, Kerala, India.)

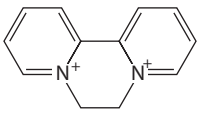

Diquat

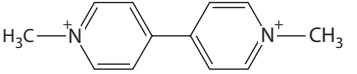

Paraquat

Figure 2.24 Two important bipyridium herbicides. Notice that both carry positive charges associated with the nitrogen atoms in their rings.

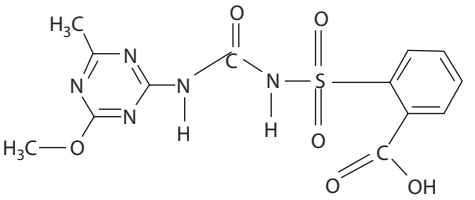

Metsulfuron

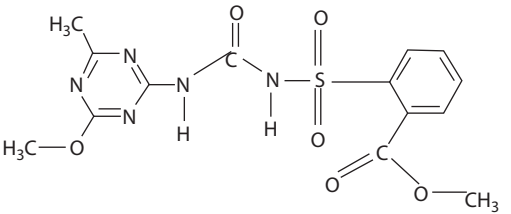

Metsulfuron-methyl

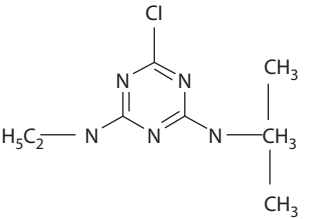

Atrazine

Figure 2.25 Three triazine herbicides including atrazine, which is a very widely used herbicide.

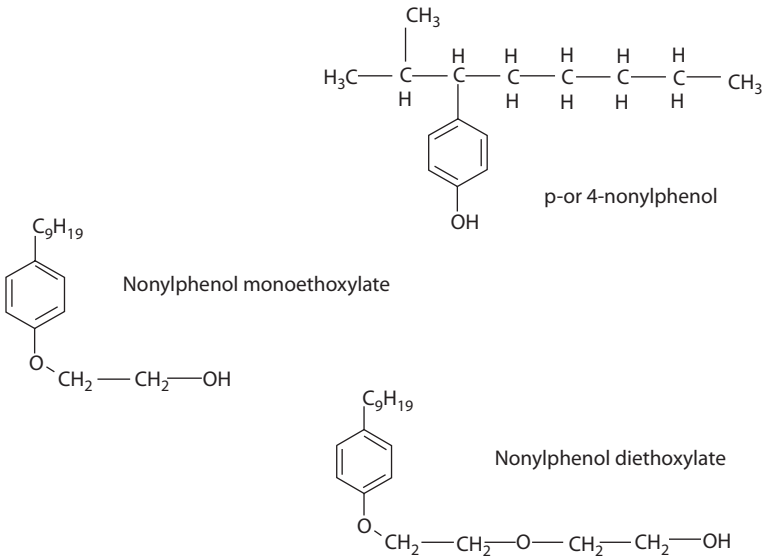

Figure 2.26 The structure of p- or 4-nonylphenol (top) and also two nonylphenol ethoxylates, nonylphenol mono- and diethoxylate. (The C_9H_{19} in these two nonylphenol ethoxylates represent the nine-carbon alkane part of a nonylphenol such as p-nonylphenol.) The commercial nonylphenol ethoxylates degrade to relatively persistent, degradation products such as these three compounds (Cox, 1996). The depicted mono- and diethoxylates degradation products have one and two ethylene oxide groups, respectively. Much of the nonylphenol present in the environment comes from the degradation of 4-nonylphenol polyethoxylates with nine or more ethylene oxide groups in their structures. Generally, the more highly ethoxylated 4-nonylphenol polyethoxylates are the most readily degraded. (From Hale, R.C. et al. *Environ. Toxicol. Chem.,* 19, 946–952, 2000.)

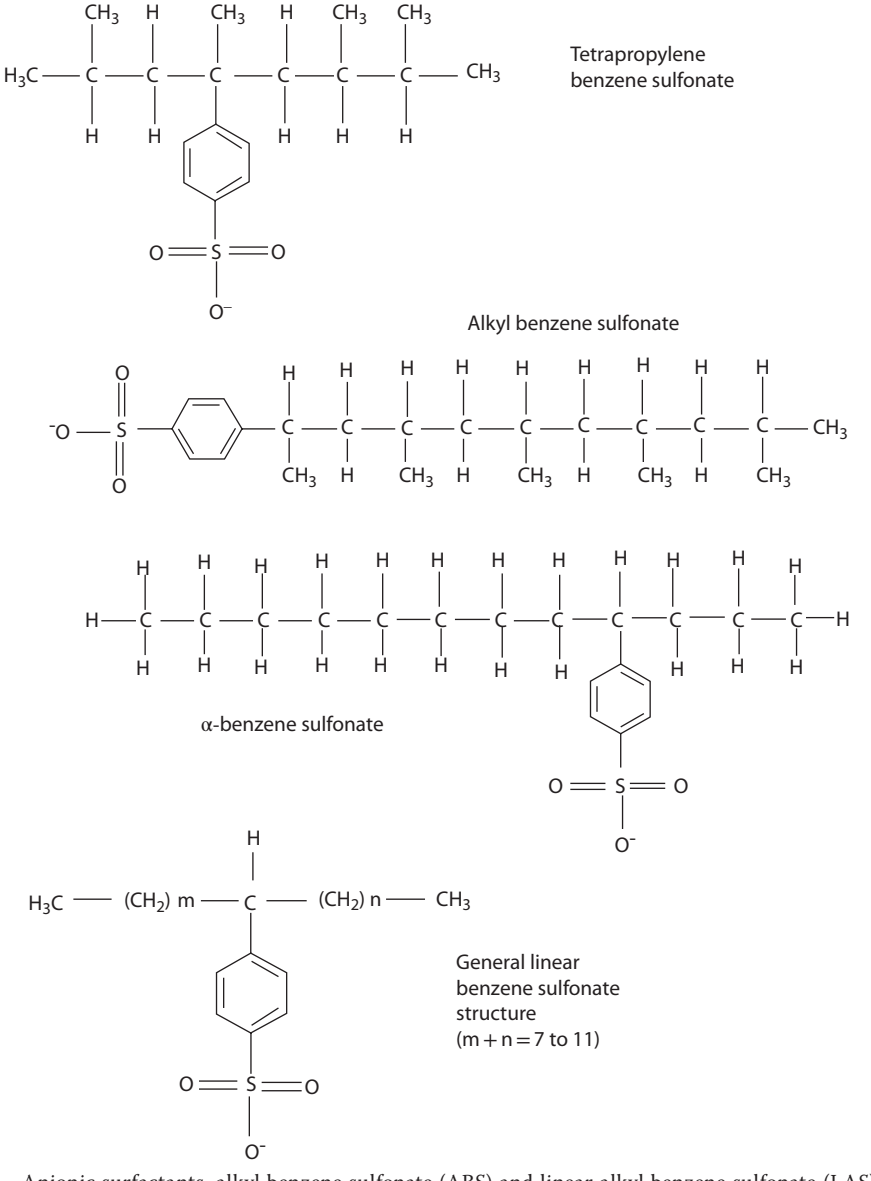

Figure 2.27 Anionic surfactants, alkyl benzene sulfonate (ABS) and linear alkyl benzene sulfonate (LAS), used in cleansers and detergents. The tetrapropylene benzene sulfonate and alkyl benzene sulfonate with the aromatic group on the terminal carbon are more resistant to degradation than the LAS, α-benzene sulfonate shown here. The general structure of LAS is shown at the bottom of this figure.

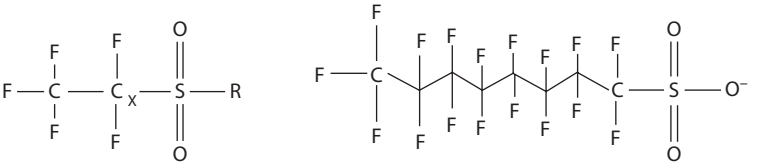

Figure 2.28 The general structure of a perfluoroalkyl sulfonate and an example (PFOS).

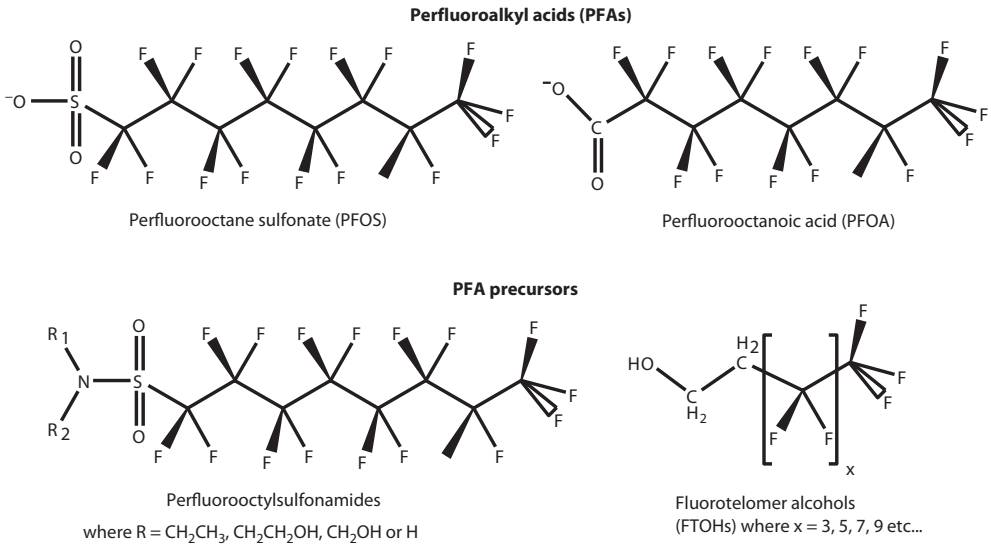

Figure 2.29 Structures of some representative perfluoroalkyl substances.

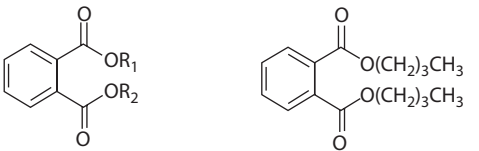

General phthalate structure

Di-n-butyl-phthalate

Figure 2.30 The general phthalate structure and the example of di-n-butyl-phthalate.

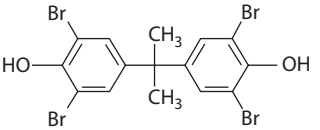

Tetrabromobisphenol A (TBBPA)

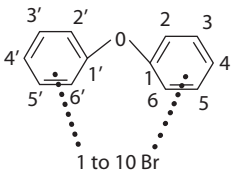

General polybrominated diphenyl ether (PBDE) structure

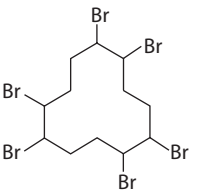

Hexabromocyclododecane (HBCD)

Figure 2.31 The brominated fire retardants including the polybrominated biphenyl ether general structure, tetrabromobisphenol A (TBBPA), and hexabromocyclododecane (HBCD). Note that another brominated flame retardant (polybrominated biphenyl in Figure 2.10) has already been discussed.

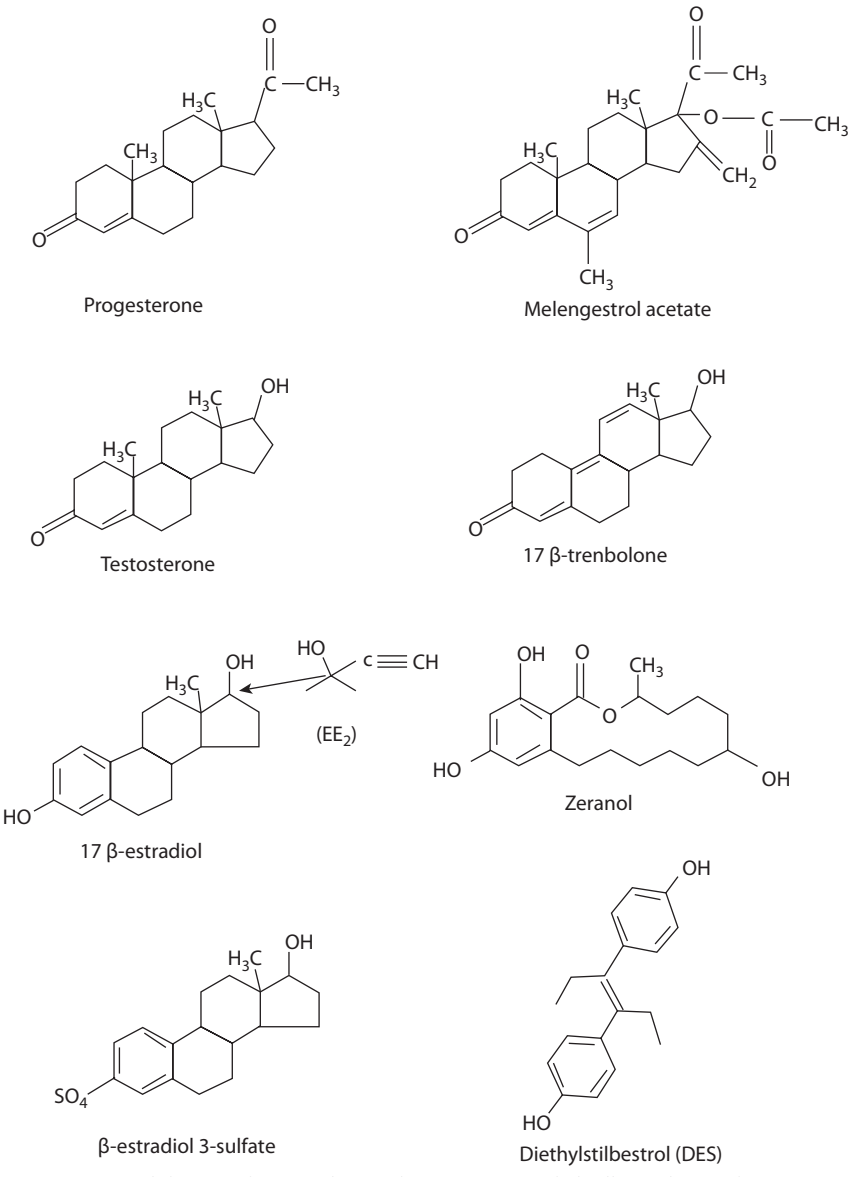

Figure 2.32 Hormones and their synthetic analogs and conjugates. Diethylstilbestrol, a synthetic estrogen, was used until the 1970s to reduce the risk of spontaneous abortions in pregnant women with unanticipated detrimental consequences. Progesterone, testosterone, and 17 β-estradiol are natural hormones. Examples of their synthetic analogs are shown to their right (modified from Figure 1 of Meyer [2001]). Zeranol, a synthetic estrogen, and trenbolone, a synthetic androgen, are used to enhance livestock growth. Similarly, melengestrol acetate is provided for growth enhancement of female livestock as well as for regulating reproduction (Meyer, 2001). 17 β-ethynylestradiol (EE2 or EE_2), a 17 β-estradiol analog used for birth control purposes by women, is similar to 17 β-estradiol but has an additional $^{-}C{\equiv}CH$ group as shown in this figure. Both, 17 β-ethynylestradiol and 17 β-estradiol are conjugated with $^{-}SO_4$ in the body and eliminated in the bile as discussed in Chapter 3.

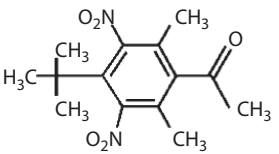

Musk ketone

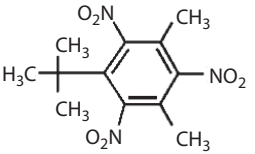

Musk xylene

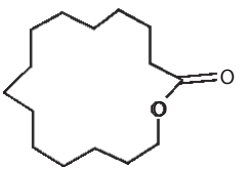

Macrocyclic musk

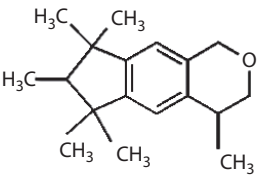

Polycyclic musk

Figure 2.33 Large amounts of synthetic musks are produced annually and used widely in products like toiletries, laundry products, cosmetics, and perfumes. Osemwengie and Steinberg (2001) quote a 1999 worldwide musk production estimate of 6 million kilograms. The musk ketone and xylene shown at the top are nitro musks. At the bottom are examples of macrocyclic and polycyclic musks. Many synthetic musks and their metabolites are not readily biogradable and are lipophilic enough to raise concerns about bioaccumulation in biota including humans (Osemwengie and Steinberg, 2001). (Note that xylene refers to the presence of a benzene ring with two attached methyl groups. Ketone refers to the presence of a carbon atom with a double bond to an oxygen atom and its remaining two bonds with other organic structures, that is, RR'CO.)

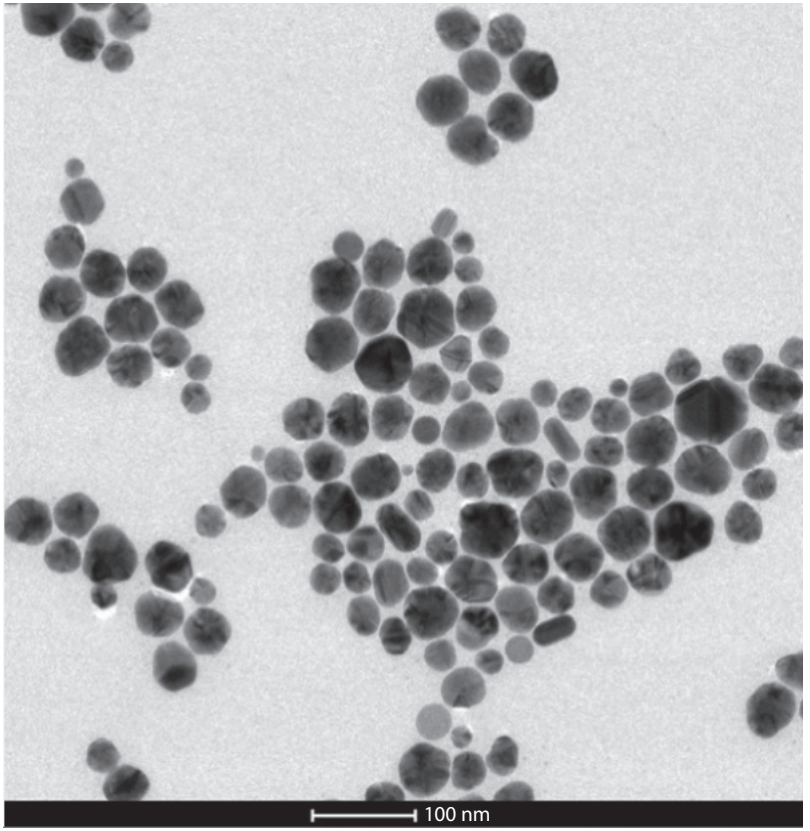

Figure 2.34 Silver nanoparticles that are increasingly used as antimicrobial agents in medical products. Yang et al. (2012) exposed the soil nematode, *Caenorhabditis elegans*, to these particles, finding that oxidative dissolution of silver contributed to nanoparticle toxicity. (Transmission electron micrograph courtesy of S. Marinakos, Duke University, Durham, NC.)

Reactor state	
Hot	**Cold**
Temperature (°C)	
61	16
(30–68)	(8–24)
Dissolved O_2 (mg L^{-1})	
3.9	9.3
(2.7–6.7)	(7.1–11.5)

Temperature (°C)	
52	17
(31–60)	(7–28)
Dissolved O_2 (mg L^{-1})	
4.4	9.0
(3.3–6.7)	(7.0–11.0)

Temperature (°C)	
39	20
(25–46)	(8–25)
Dissolved O_2 (mg L^{-1})	
6.7	9.5
(5.5–8.7)	(6.4–12.3)

Figure 2.35 Thermal pollution associated with a nuclear production reactor (K-Reactor on Pen Branch, U.S. Department of Energy Savannah River Site, South Carolina, 1985–1986). Arithmetic means and ranges of water temperature (°C) and dissolved oxygen concentration (mg $O_2 \cdot L^{-1}$) are provided for times when the reactor was active (Hot) and inactive (Cold) (Newman, 1986). Due to pump engineering issues, water flow was maintained through the system regardless of reactor production status. Photographs and water quality information are those from approximately 2 km below the K-reactor discharge into Indian Grave Creek (top), 9 km below the discharge (middle), and 12 km below the reactor discharge where the discharged waters entered the extensively damaged 40.5 km^2 bald cypress-tupelo river swamp adjoining the Savannah River (bottom). (Photograph by M. C. Newman.)

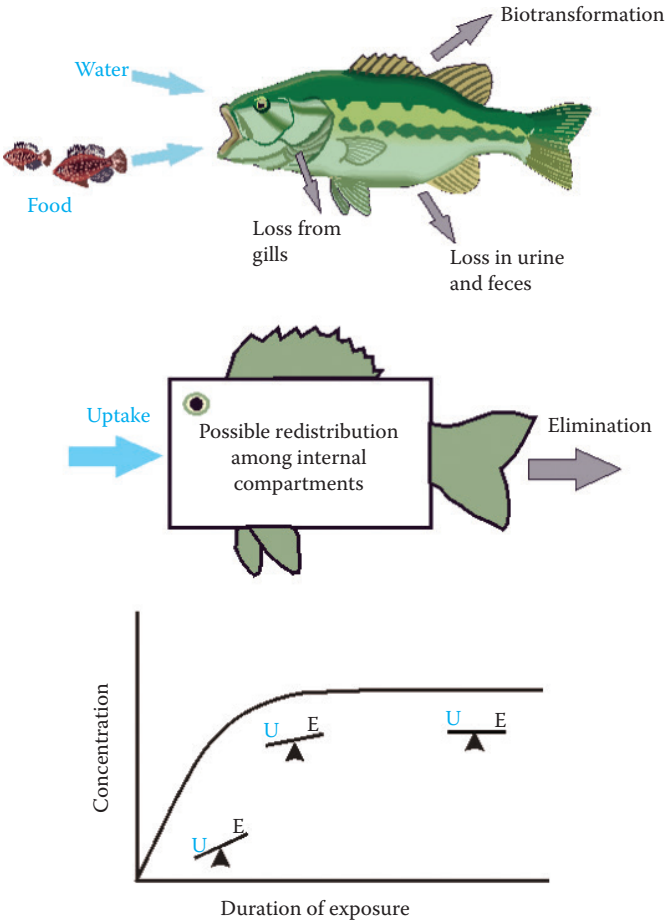

Figure 3.1 A simplified conceptualization of bioaccumulation. At the top of this figure, the fish (largemouth bass) is thought to potentially take in a substance from its food and water, and lose it through the gills, urine, and feces. There might be internal redistribution or biotransformation of the contaminant. This process is rendered to a simple box and arrow diagram (middle graph). Here, only uptake from water is assumed to be significant, and all elimination processes are described by one elimination component. The most common mathematical description of this model predicts a gradual increase in contaminant in the fish until a steady-state concentration is obtained as depicted in the graph at the bottom of this figure. (U, uptake; E, elimination.)

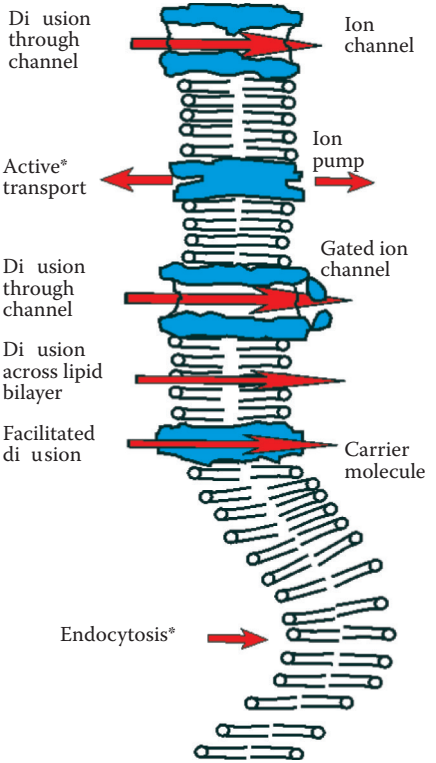

Figure 3.2 Mechanisms of uptake of contaminants into cells. Simple diffusion can occur across the lipid bilayer or through an ion channel formed by a channel protein. Channels may be gated and their functioning influenced by chemical and electrical conditions. Facilitated diffusion occurs through a carrier protein. Active transport moves the solute up an electrochemical gradient. Here, the Na^+, K^+-ATPase pump is illustrated. Potassium is pumped into the cell as sodium is pumped out. The last mechanism for cellular uptake is endocytosis. As indicated by an asterisk, endocytosis and active transport require energy.

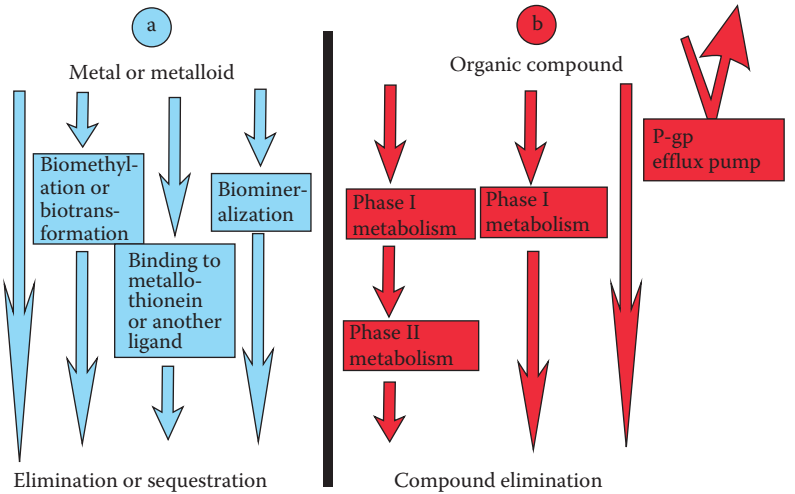

Figure 3.3 General mechanisms of biotransformation and detoxification of inorganic (a, blue) and organic (b, red) contaminants (see text for explanation).

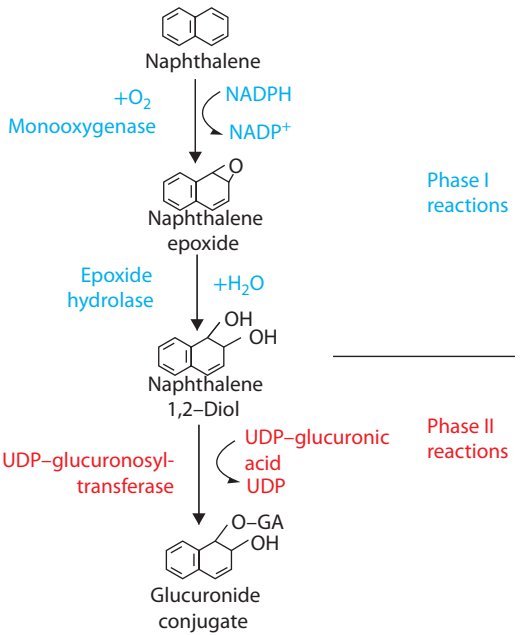

Figure 3.4 Metabolism of naphthalene including Phase I (blue) and Phase II (red) reactions. The first Phase I reaction (naphthalene → napthalene epoxide) is an oxidation reaction and the second Phase I reaction (naphthalene epoxide → naphthalene 1,2-diol) is a hydrolysis reaction. UDP-glucuronic acid is formed by condensation of UTP (high-energy nucleotide, uridine triphosphate) with glucose-6-phosphate. UDP, uridine diphosphate; GA, glucuronic acid. (Composite Figures 1, 5, and 14 of Lech, J.J. and M.J. Vodicnik, *Fundamentals of Aquatic Toxicology*, Rand, G.M. and S.R. Petrocelli, Eds., Hemisphere Publishing Corp., Washington, DC, 1985.)

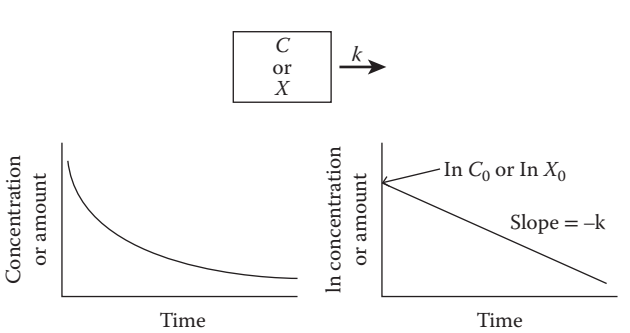

Figure 3.5 Elimination of a contaminant under a depuration scenario including linearization to extract k and C_0 or X_0.

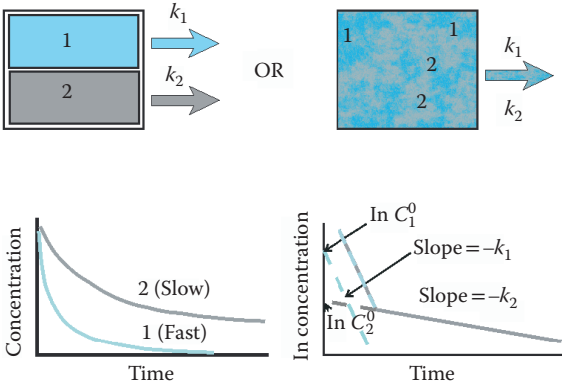

Figure 3.6 Elimination involving two compartments and two elimination constants including backstripping to calculate k_1, k_2, C_1, and C_2. The upper left is the most idealized and least realistic visualization: the upper right is a more realistic visualization involving two discrete compartments (blue and gray) that are interspersed as might occur for contaminants in discrete bone compartments.

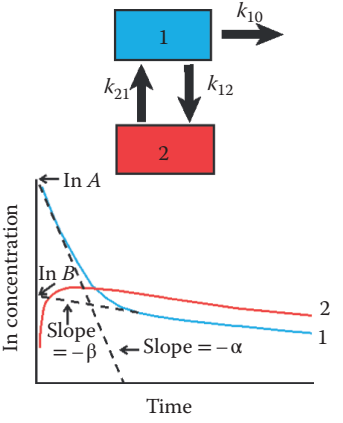

Figure 3.7 Elimination from a two compartment model after bolus introduction of the contaminant into compartment 1. A, B, α, and β are used to estimate k_{12}, k_{10}, and k_{21} as described in the text.

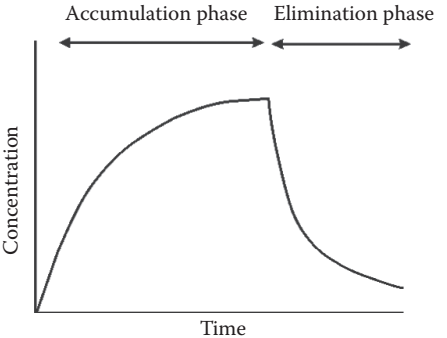

Figure 3.8 Simple bioaccumulation through time as described by Equation 3.20 followed by elimination as described by Equation 3.9. Data of this type are generated with an accumulation–elimination experiment. In the accumulation phase, kinetics is dictated by both uptake and elimination. The organism is then allowed to depurate and kinetics in this elimination phase is solely a consequence of elimination.

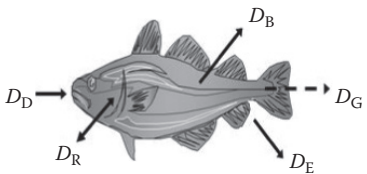

Figure 3.9 An illustration of chemical transport and transformation processes (D values) for bioaccumulation in fish.

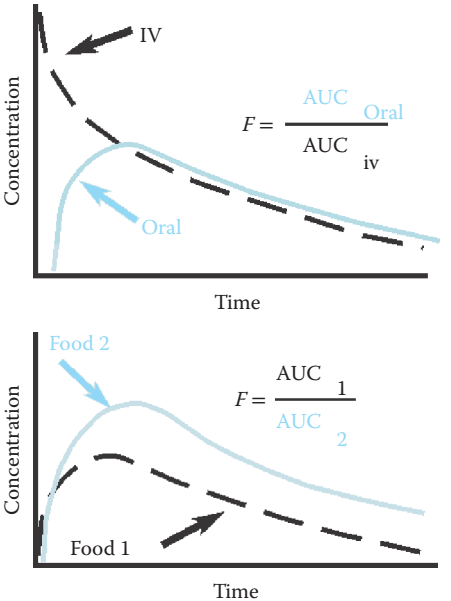

Figure 4.1 Estimation of absolute bioavailability of an ingested dose by comparison of AUCs for ingestion and intravenous injection (top panel), and relative bioavailability by AUC comparison for the same dose administered in two different foods (bottom panel).

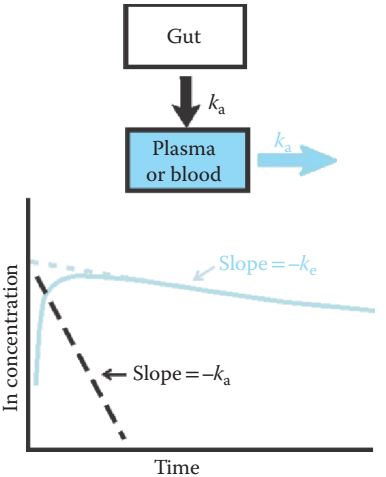

Figure 4.2 A visual illustration of absorption rate constant estimation using the method of residuals (bottom panel is a modification from Figure 4.12 of Renwick [2008]). Assuming first-order elimination and absorption from the gut, the concentration in the blood or plasma is plotted after dosing via ingestion (solid blue curve). As done in Figure 3.7, a linear model is fit to the terminal, linear part of this curve (dashed blue line). The differences are then plotted between measured concentrations and corresponding predicted concentrations for all points taken before the linear portion of the (blue) plasma/blood concentration–time curve (black dashed line). The absorption rate constant ($-k_a$) is derived from the slope of this derived line.

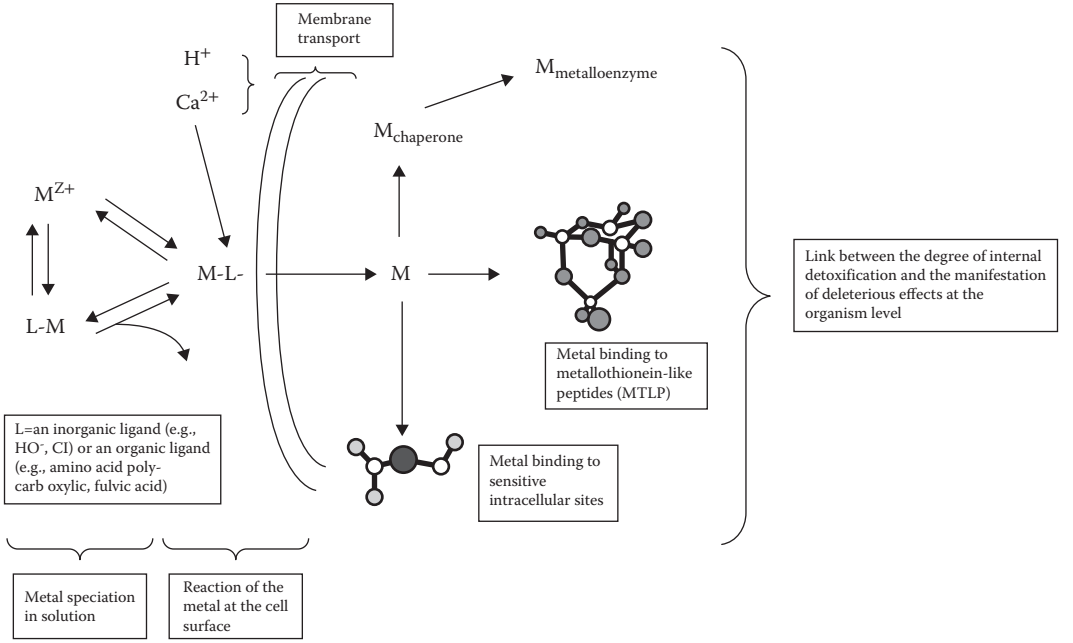

Figure 4.3 Metal (M) speciation in water (left), the interaction of the metal at an external biological membrane, and metal transport into the cell (right) where it is partitioned among various cellular fractions.

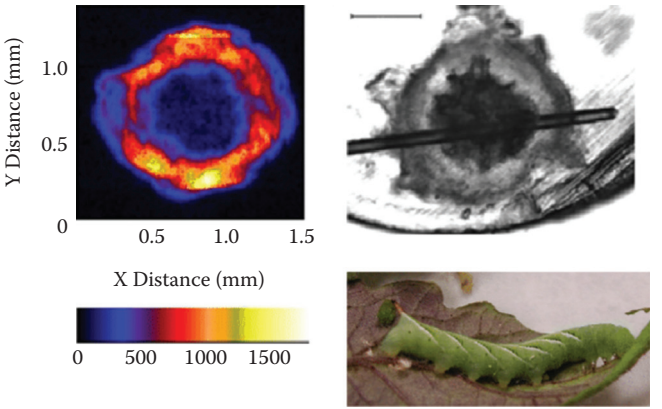

Figure 4.4 Synchrotron x-ray fluorescence microprobe (μXRF) map of fluorescence from the Au L-α edge of gold (upper left) and corresponding light micrograph of a cross-section (upper right) from a tobacco hornworm (*Manduca sexta*, lower right) fed plants exposed to 5-nm nanoparticles. The fluoresence intensity legend (counts per second, lower left) indicates the relative amounts of gold in areas of the gut cross-section. (Images courtesy of Jonathan Judy. Study details in Judy, J.D., et al. *Environ. Sci. Technol.*, 45, 776–781, 2011; Judy, J.D., et al. *Environ. Sci. Technol.*, 46, 12672–12678, 2012.)

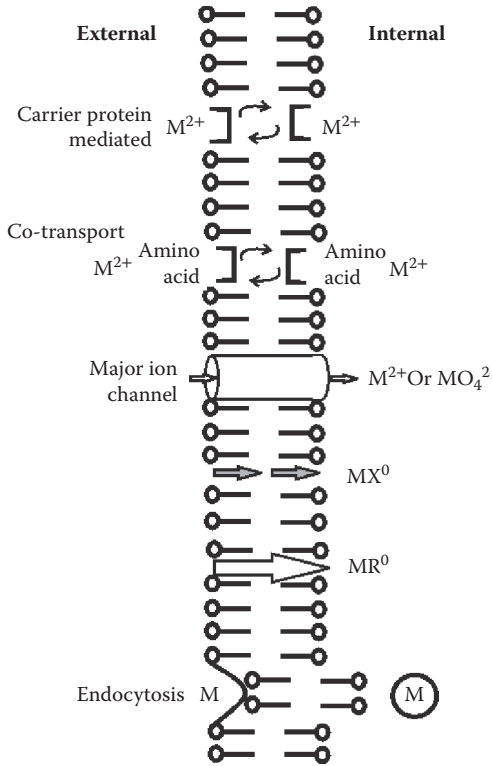

Figure 4.5 Means by which metals can move into cells.

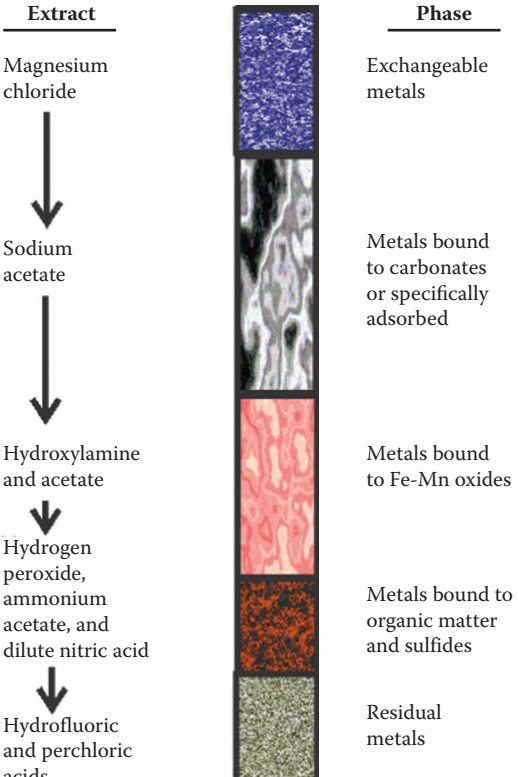

Figure 4.6 Fractionation of sediment-associated metals by sequential extraction. In the scheme shown here (Tessier et al. 1984), an aliquot of sediment is sequentially extracted with magnesium chloride, sodium acetate, hydroxylamine and acetate, hydrogen peroxide, ammonium acetate and nitric acid, and, finally, strong acid to produce five different extracts. These extracts are thought to grossly reflect the amount of metal in the forms noted at the right side of the figure. These are operational definitions and the phase descriptions often do not accurately reflect the true phase association of the extracted metals.

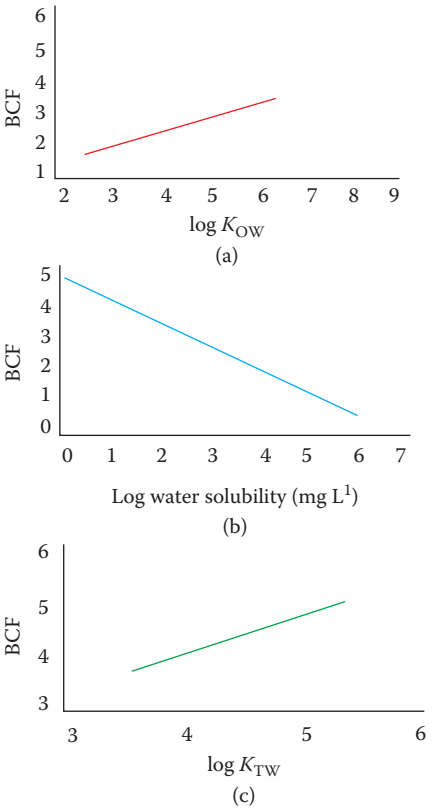

Figure 4.7 Relationships between bioconcentration factors for a variety of organic compounds and log K_{OW} (trout muscle), log water solubility (marine mussel), and K_{TW} or log of triolein–water partition coefficient (log K_{TW}, pooled data for rainbow trout and guppies). (Panels a, b, and c are modified from Figure 1 of Neely et al. (1974), Figure 1 of Geyer et al. (1982), and Figure 3 of Chiou (1985), respectively.)

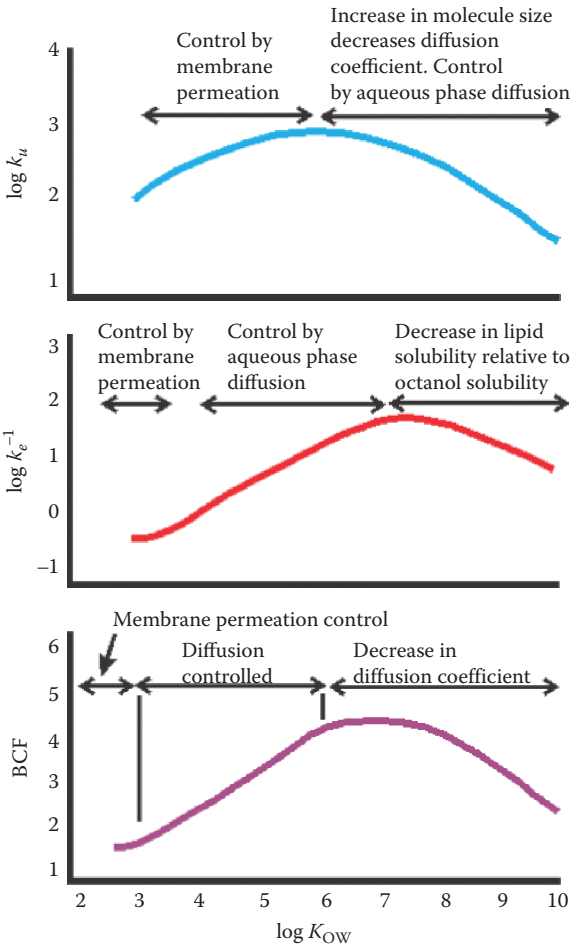

Figure 4.8 A summary of the changes in uptake, elimination, and bioaccumulation (bioconcentration factor) as related to K_{OW}. (Modified from Figures 3, 4, and 5 of Connell, D.W. and D.W. Hawker, *Ecotox. Environ. Safe.*, 16, 242–257, 1988.)

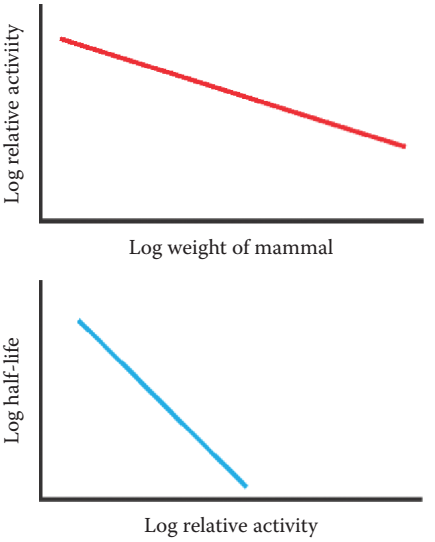

Figure 4.9 The scaling of monooxygenase activity (top panel) and the relationship between relative monooxygenase activity and biological half-life of xenobiotic metabolism (bottom panel). (Composite and modified from Figures 2 and 3 of Walker, C. H., *Drug Metab. Rev.*, 7, 295–323, 1978.)

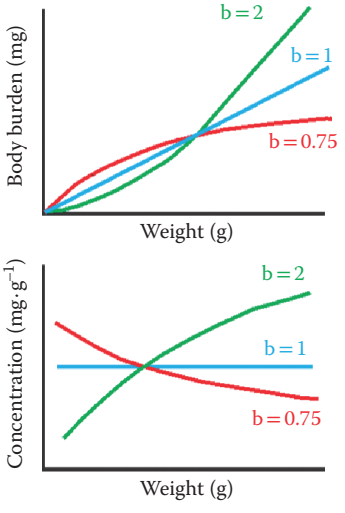

Figure 4.10 The relationships between organism size (weight) and body burden (amount per individual) (top panel) and concentration (amount per gram of tissue) of metal. Modified from Figure 13 of Newman (1995) with slight exaggeration of curvature of the concentration versus size plots to make clear the nonlinear nature of two of these curves ($b = 2$ and $b = 0.75$). The point of intersection for both plots occurs, where $X = 1$. (Reprinted with permission from Newman, M.C., *Quantitative Methods in Aquatic Ecotoxicology*, Lewis Publishers, Boca Raton, FL, 1995. Copyright Lewis Publishers, an imprint of CRC Press, Boca Raton, FL.)

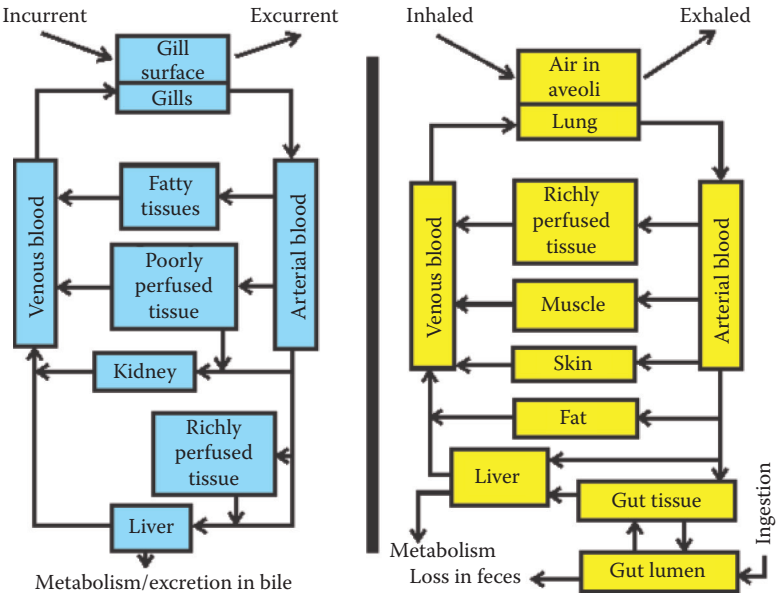

Figure 4.11 Two PBPK models. The model to the left involves the fish uptake of a xenobiotic across the gills, distribution among five compartments and blood, and loss via the liver (Nichols et al. 1990). The model on the right involves styrene inhalation and ingestion by a mammal, distribution into a series of compartments, and loss from liver metabolism and defecation (Paterson and Mackay, 1987). In the original publications, the fish model was formulated as a clearance volume-based model and the mammalian model was formulated as a fugacity-based model.

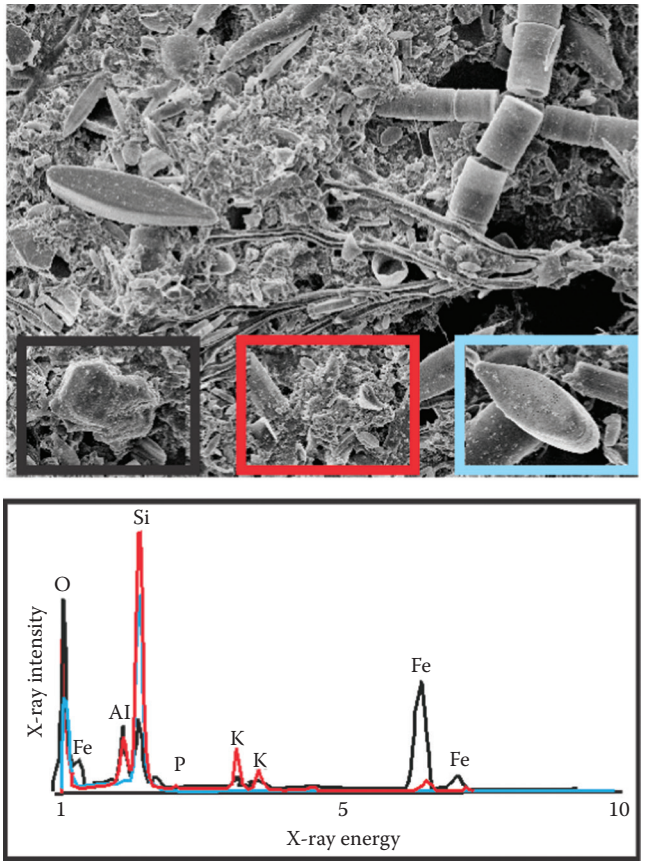

Figure 5.1 A scanning electron microscope image of procedurally defined periphyton removed from submerged surfaces of the South River (Virginia). The inserts are higher magnification images of selected areas. X-ray spectra obtained from three contrasting areas of peryphyton were generated during electron bombardment of the samples in the scanning electron microscope and are depicted at the bottom of this figure. The elements associated with each peak of characteristic x-rays are also shown and correspond in color to the framed micrograph regions. The spectra drawn with a black line was rich in Al, O, Si, K, and particularly iron, indicating mineral composition with considerable iron oxides. The spectrum drawn in red was from an area that was rich in Al, O, Si, and K, suggesting primarily mineral composition again with perhaps considerable quartzite and clays. The last (blue line) was taken from a diatom that has a frustule composed of silicon dioxide as is clear from the large Si and O x-ray peaks. (M. C. Newman, Unpublished micrographs and spectra.)

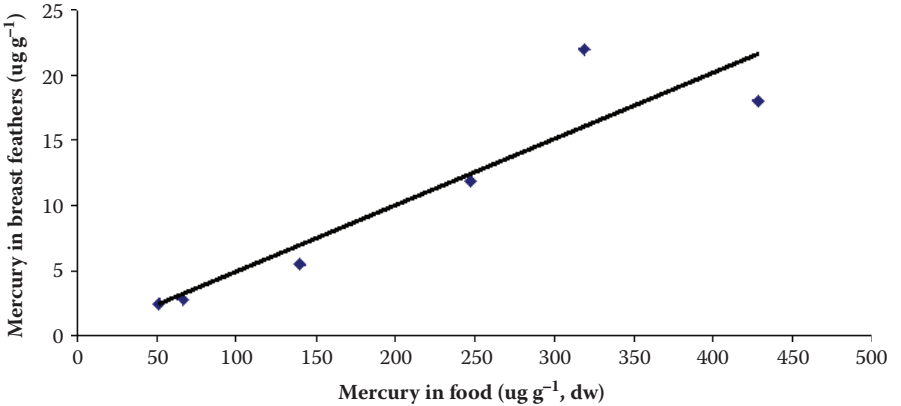

Figure 5.2 Relationship between mercury in body feathers and mercury in the diet for six species of seabirds in the Azores. (Redrawn from Monteiro, L. R. et al. *Mar. Ecol.- Prog. Ser.*, 166, 259–265, 1998.)

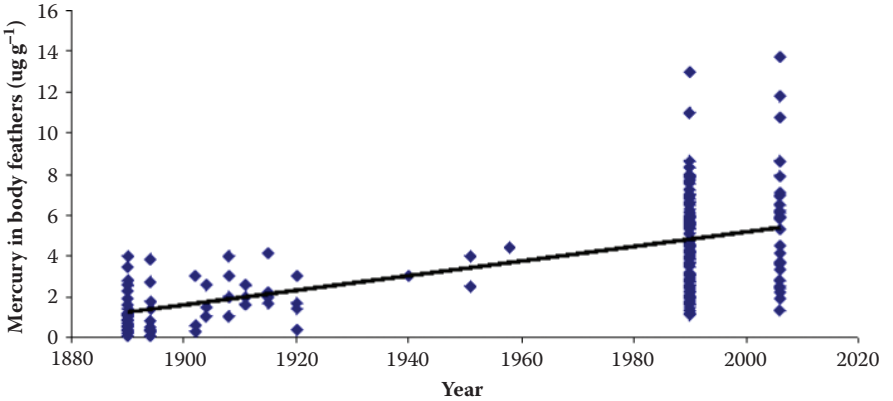

Figure 5.3 Mercury concentrations in pooled samples of several body feathers from Atlantic puffins from Scotland. (Data from Thompson, D.R. et al. *J. Appl. Ecol.*, 29, 79–84, 1992, updated with new data from 2006.)

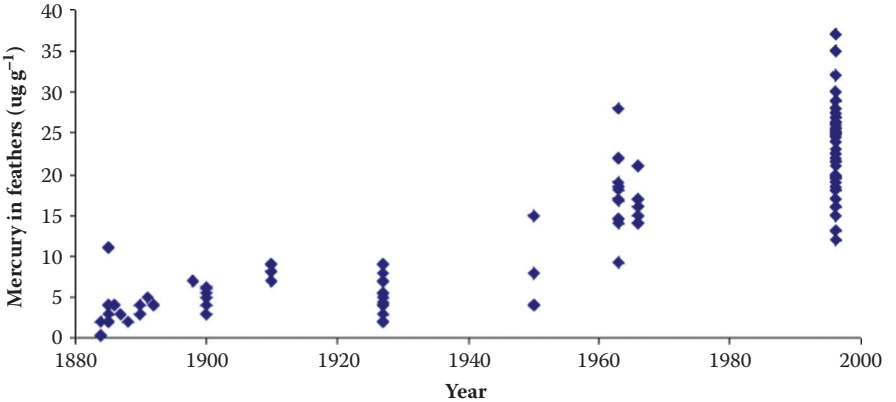

Figure 5.4 Mercury concentrations in pooled samples of several body feathers from Bulwer's petrels in the Azores. (Redrawn from Monteiro, L. R. and R. W. Furness, *Environ. Toxicol. Chem.*, 16, 2489–2493, 1997.)

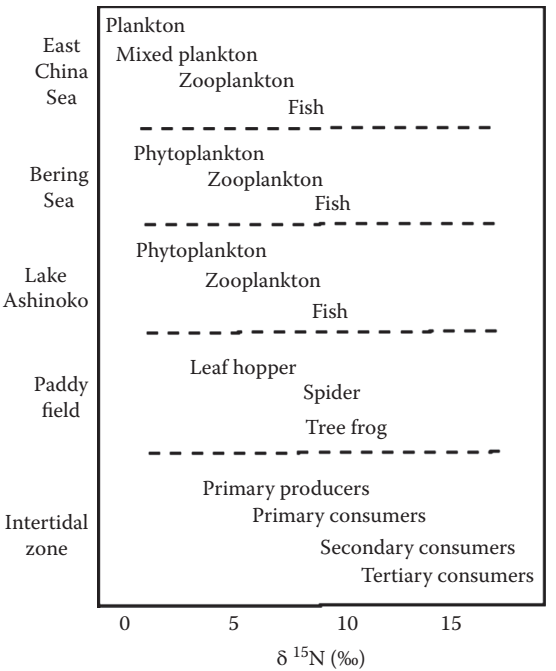

Figure 5.5 The change in $\delta\ ^{15}N$ (‰) with increase in trophic level for the diverse communities of the East China Sea (an oligotrophic sea with significant amounts of nitrogen fixation at the time of phytoplankton sampling, which brought the $\delta\ ^{15}N$ to near atmospheric levels), the Bering Sea (North Atlantic Ocean), Lake Ashinoko (freshwater lake), a paddy field (terrestrial system) in Konosu, Japan, and an intertidal zone. (A composite and modification of Figures 1 and 2 in Minagawa, M. and E. Wada, *Geochim. Cosmochim. Ac.*, 48, 1135–1140, 1984.)

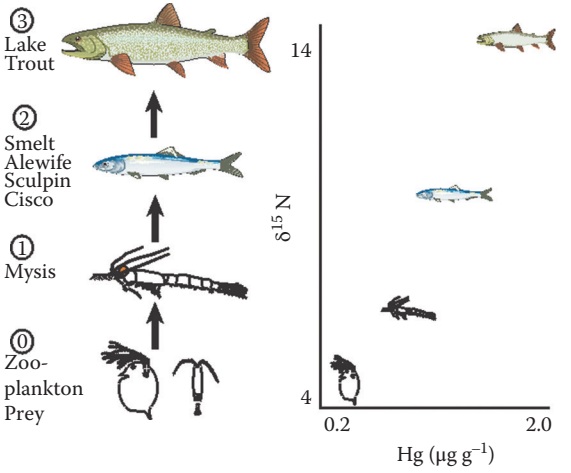

Figure 5.6 The increase in mercury from zooplankton to a zooplanktivorous shrimp (*Mysis relicta*) to pelagic forage fish to lake trout (*Salvelinus namaycush*). The trophic structure is quantified with $\delta\ ^{15}N$: its value increasing roughly 3.4‰ at each trophic exchange. A clear relationship is evident between mercury concentration and trophic status of individuals, indicating biomagnification of mercury. (Constructed using data and Figure 2 of Cabana, G. and J. B. Rasmussen, *Nature,* 372, 255–257, 1994.)

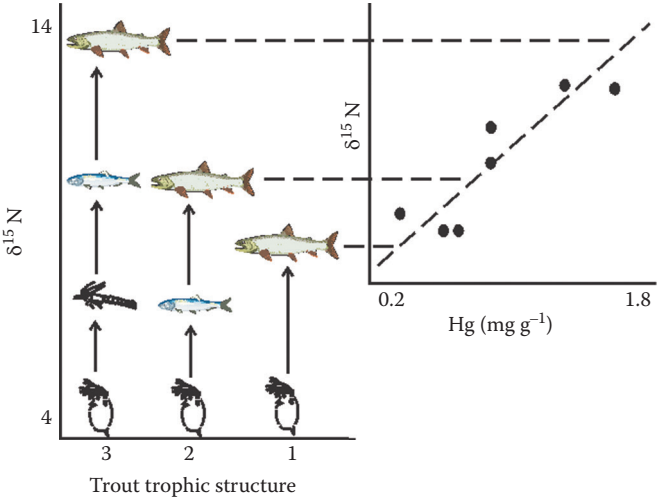

Figure 5.7 Correlation between mercury concentration and trophic structure (δ ^{15}N) for Canadian lakes with different trophic structure relative to lake trout (*Salvelinus namaycush*). In some lakes, shrimp and/or forage fish are missing, giving rise to various trophic structures relative to lake trout. Using a discrete assignment of trophic structure, 3 = same structure as shown in Figure 5.6 (zooplankton → shrimp → forage fish → lake trout), 2 = shortened structure without shrimp (zooplankton → forage fish → lake trout), and 1 = a simple structure with both shrimp and forage fish being insignificant. (Forage fish were predominantly alewife [*Alosa pseudoharengus*], cisco [*Coregonus artedii*], whitefish [*Coregonus clupeaformis*, *Prosopium cyclindraceum*], sculpin [*Myoxocephalus thompsoni ?*], and smelt [*Osmerus mordax*].) The panel on the upper right shows the actual mercury concentrations and δ ^{15}N values for lake trout from seven Canadian lakes. Note that trout from these lakes are shifted slightly to positions intermediate between the discrete trophic structure levels. (Composite and modification of Figures 2 and 3 of Cabana, G. and J. B. Rasmussen, *Nature,* 372, 255–257, 1994.)

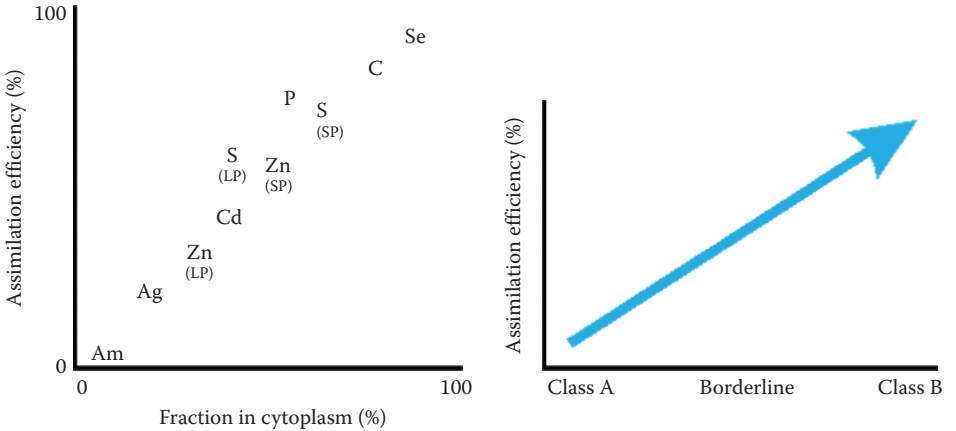

Figure 5.8 Assimilation efficiencies of elements contained in diatoms (*Thalassiosira pseudonana*) fed to zooplankton (*Acartia tonsa*, *Acartia hudsonica*, or *Temora longicornis*) plotted against the amount of each element associated with the cytoplasm of the diatoms (left panel). SP = data derived using stationary phase (senescent) diatom cultures and LP = results derived from diatom cultures in the log phase of growth. (Modified from Figure 1 of Reinfelder and Fisher [1991].) The right panel depicts the general trend in assimilation efficiency hypothesized relative to the Class B—borderline—Class A classification of metals.

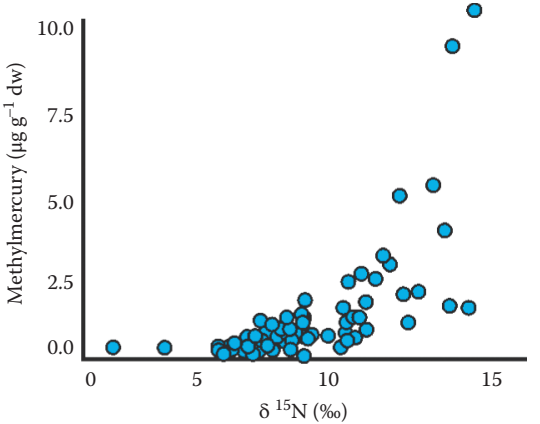

Figure 5.9 Methylmercury biomagnification in the South River (Virginia) is clear using δ ^{15}N values to indicate trophic position of biota in this river. (Data from Tom, K. R. et al. *Environ. Toxicol. Chem.*, 29, 1013–1020, 2010.)

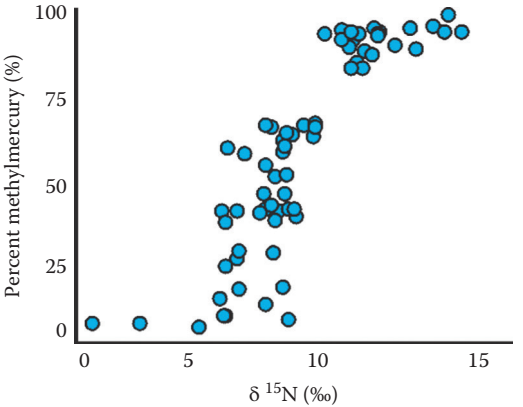

Figure 5.10 Increase in the percentage of the total mercury that is methylmercury in members of the aquatic food web of the South River below a source of inorganic mercury (Virginia). Biota sampled ranged from periphyton to invertebrates to forage fish to piscivorous fish. (Data from Tom, K. R. et al.*Environ. Toxicol. Chem.,* 29, 1013–1020, 2010.)

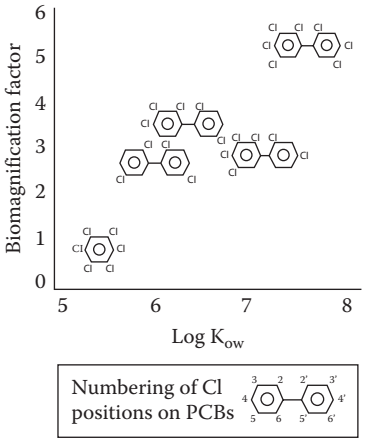

Figure 5.11 The increase in biomagnification factor (concentration in white bass/concentration in emerald shiner) with increasing log K_{ow} values for hexachlorobenzene (bottom left) and four polychlorinated biphenyls (PCBs), 2,2′,5,5′-tetrachlrobiphenyl, 2,2′,3,4,5′-pentachlorophenyl, 2,2′,3,4,4′,5-hexachlorobiphenyl, and 2,2′,34,4′,5,5′-heptachlorobiphenyl. (Modified from Figure 2 in Russell et al. [1995].) Note that a key to the numbering of chloride atoms attached to the biphenyl rings is provided at the bottom of this figure. The prefixes, tetra-, penta-, hexa-, and hepta-, refer to the total number of chloride atoms in the PCB molecule.

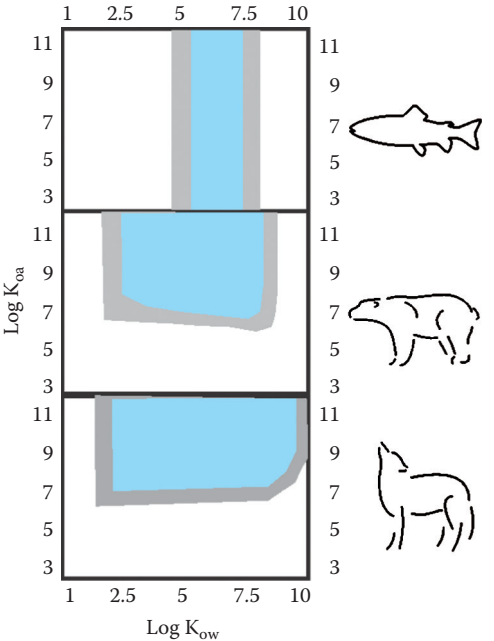

Figure 5.12 The influence of K_{ow} and K_{oa} on POP biomagnification in aquatic piscivore-focused (top panel), marine mammal-focused (middle panel), and terrestrial mammal-focused (bottom panel) food webs. Combinations of log K_{ow} and log K_{oa} associated with a biomagnification factor in the final web predator are shown: 2 or less (white areas), approximately >2 to 25 (grey area), and >25 (blue area). (This figure was drawn using information from three panels in Figure 3 of Kelly, B. C. et al. *Science,* 317, 236–239, 2007).

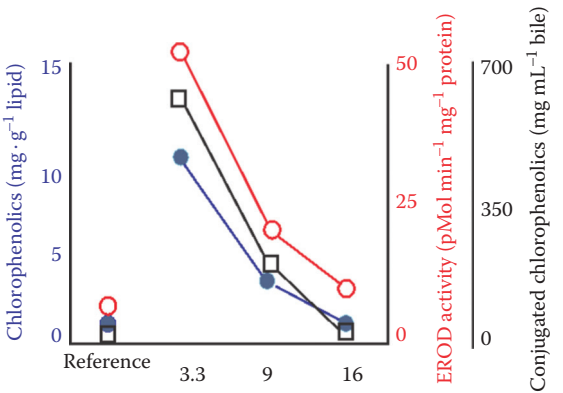

Figure 6.1 The response of biomarkers in juvenile whitefish (*Coregonus lavaretus*) to pulp and paper mill effluents. The concentration of total chlorophenolics in the gut lipids of this sentinel species (●) were elevated in whitefish taken 3.3 km below the discharge relative to the reference samples and rapidly decreased with distance from the discharge. Similarly, two biomarkers, EROD activity (○) and conjugated chlorophenolics in the bile (□), were highest near the discharge and decreased with distance from the paper and pulp mill effluent. (Generated by combining information from Figures 3, 4, and 5 of Soimasuo, R., et al. *Aquat. Toxicol.*, 31, 329–345, 1995.)

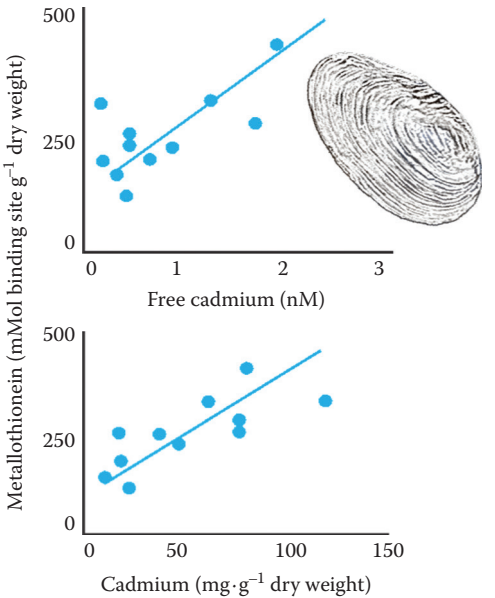

Figure 6.2 The relationships between free cadmium (Cd^{2+}) concentration in lake water (sediment-water interface) and metallothionein concentration in the freshwater mussel, *Anodonta grandis* (top panel), and cadmium concentration in the entire mussel and metallothionein concentration in this mussel (bottom panel). Each point represents samples from a different lake in the Rouyn-Noranda mining area of Quebec, Canada. (Modified from Figures 3 and 4 of Couillard, Y., et al. *Limnol. Oceanogr.*, 38, 299–313, 1993.)

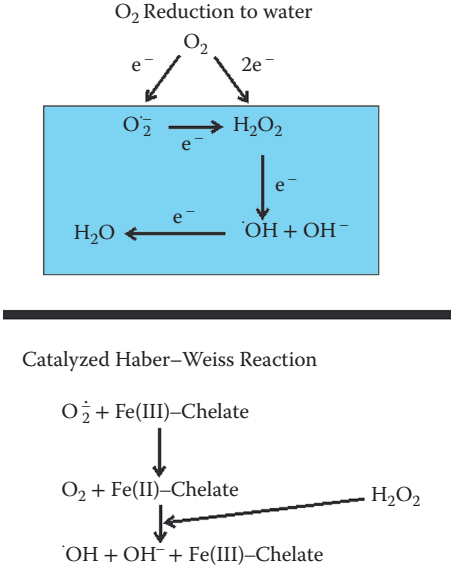

Figure 6.3 Reduction of O_2 to water during aerobic respiration ($O_2 + 4e^- \rightarrow H_2O$). Molecular oxygen can be converted to the superoxide radical ($O_2^{\cdot-}$) by adding one electron (e^-) or to hydrogen peroxide (H_2O_2) by adding two electrons. The superoxide radical can be converted to hydrogen peroxide by the addition of another electron. Hydrogen peroxide can then be reduced to the hydroxyl radical ($^{\cdot}OH$), producing a hydroxyl anion (OH^-). Water is produced with the addition of a fourth electron. Two highly reactive, free radicals are generated along this reaction sequence. Hydrogen peroxide is also produced and, through the **Haber–Weiss reaction** ($O_2^{\cdot-} + H_2O_2 \rightarrow {}^{\cdot}OH + OH^-$ as shown in the top panel in the box), generates oxyradicals. The **catalyzed Haber–Weiss reaction** is a greatly accelerated Haber–Weiss reaction catalyzed by metal chelates as shown in the bottom panel. Metals can also generate free radicals directly. As one example, chromium reacts with cysteine to produce thiol radicals (Leonard et al. 2004) which, in turn, can generate $O_2^{\cdot-}$.

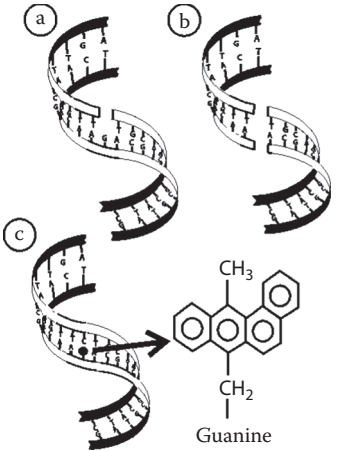

Figure 6.4 Various types of damage can occur to DNA due to toxicants. Toxicants or free radicals can produce (a) single- or (b) double-strand breaks. (c) Xenobiotics or their metabolites may react with bases to form adducts. Here, metabolism of 7,12-dimethyl-benz[a]anthracene leads to covalent bonding of its metabolite to guanine to form a DNA adduct. Interactions such as those with free radicals can also modify bases, i.e., oxidize bases such as thymine and guanine to thymine glycol and 8-hydroxyguanine, respectively. (From Di Giulio, R.T., et al. in G.M. Rand, [Ed.], *Fundamentals of Aquatic Toxicology: Effects, Environmental Fate, and Risk Assessment*, 2nd Edition, Washington, DC, Taylor & Francis, 1995.)

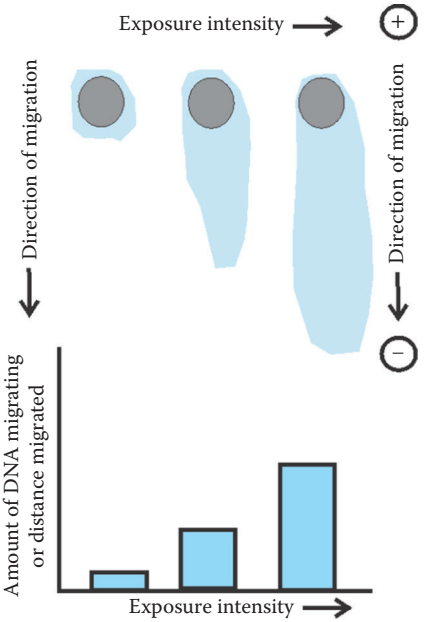

Figure 6.5 Comet electrophoresis for the detection of DNA strand breakage in individual cells. Cells are embedded in a gel, subjected to alkaline conditions, subjected to electrophoresis under alkaline conditions, stained to visualize DNA, and the amount of DNA in the resulting "comet" tail (blue) or the distance migrated by the DNA making up the tail is used as a measure of the amount of DNA breaks present. "Comets form as broken ends of the negatively charged DNA molecule become free to migrate in the electric field toward the anode. The ability of DNA to migrate is a function of both the size of the DNA and the number of broken 'ends' which may be attached to larger pieces of DNA but which can still migrate a short distance from the comet head" (Fairbairn et al. 1995). DNA patterns are depicted here for three cells that had different intensities of exposure and consequent differences in DNA breakage.

Figure 6.6 Steps in the synthesis of heme. Enzymes catalyzing each conversion are italicized and placed to the right of the reaction sequence. (Modified from Figure 1 of Woods, J.S., et al. *J. Toxicol. Environ. Health*, 40, 235–246, 1993.)

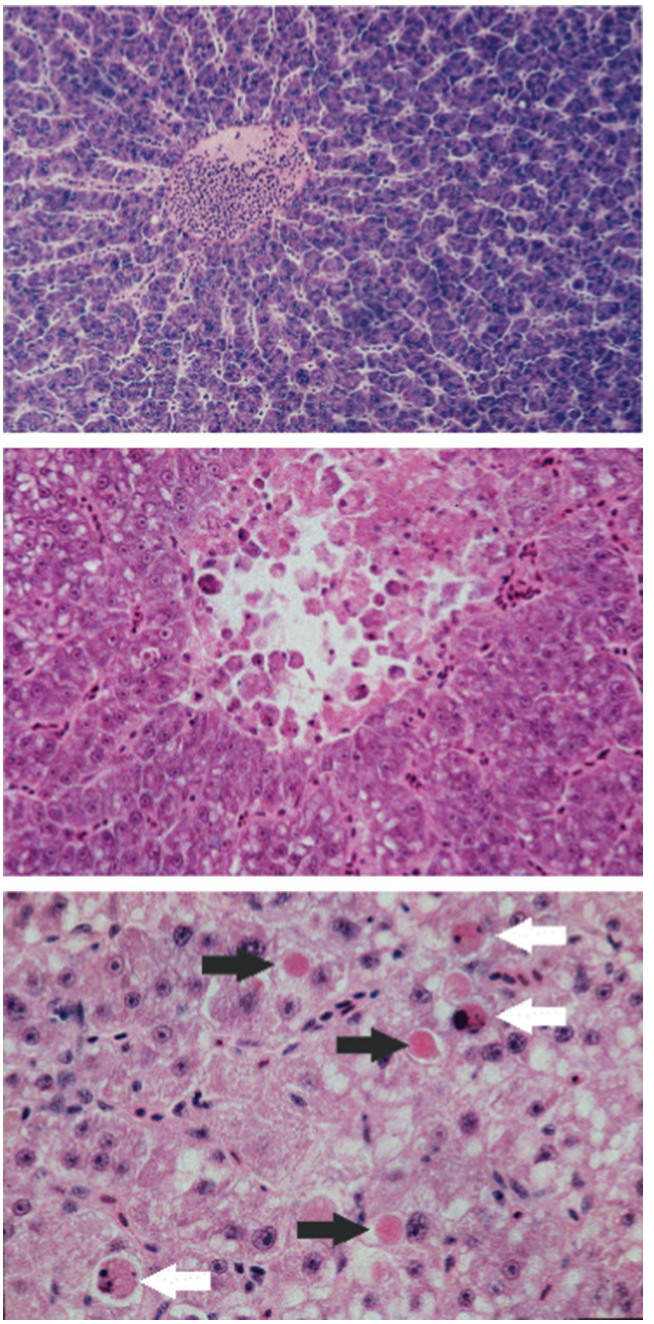

Figure 7.1 The top panel is a section through a normal *Fundulus heteroclitus* liver with branching hepatic tubules lined with hepatic sinusoids. Note that the hepatocytes are relatively uniform in size and shape. The middle panel is an example of necrosis in the liver. Notice the difference in staining between the living and dead cells. Dead cells show nuclear pyknosis and karyolysis, and loss of cell adherence. The bottom panel shows necrosis of individual cells, not a localized area as seen with the necrosis shown in the middle panel. Three necrotic cells are at the tips of the dark arrows. They are round or oval remnants that stain strongly with eosin. The basophilic chromatin remnants are visible in dead cells identified by the white arrows. (Color rendering of Figure 4.1 in Newman and Clements, 2008. Photomicrographs and general descriptions provided by W. Vogelbein, Virginia Institute of Marine Science.)

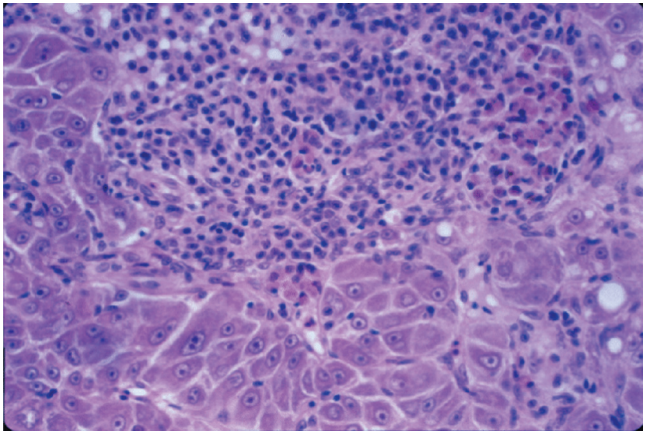

Figure 7.2 Inflammation in the liver of the estuarine fish, *Fundulus heteroclitus*. At the top center of the top photomicrograph is a focus of inflammation. (Color rendering of Figure 4.1 in Newman and Clements, 2008. Photomicrograph provided by W. Vogelbein, Virginia Institute of Marine Science.)

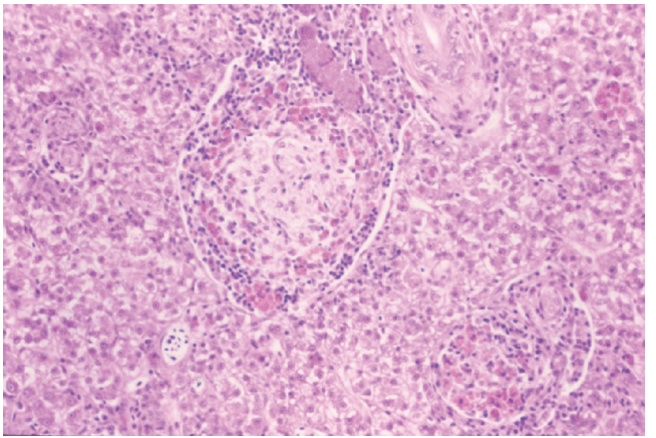

Figure 7.3 Macrophage aggregates are clumps of macrophages containing large amounts of ceroid/lipofuscin. Aggregates are surrounded by a fine capsule of connective tissue, are often associated with sites of inflammation, and, in mummichog (*F. heteroclitus*) from contaminated habitats, are greatly elevated in number and in size. Vogelbein and co-researchers suggest that this reflects the terminal stage of an inflammatory process in response to specific and nonspecific degenerative necrotic changes. (Photomicrograph and general description provided by W. Vogelbein, Virginia Institute of Marine Science.)

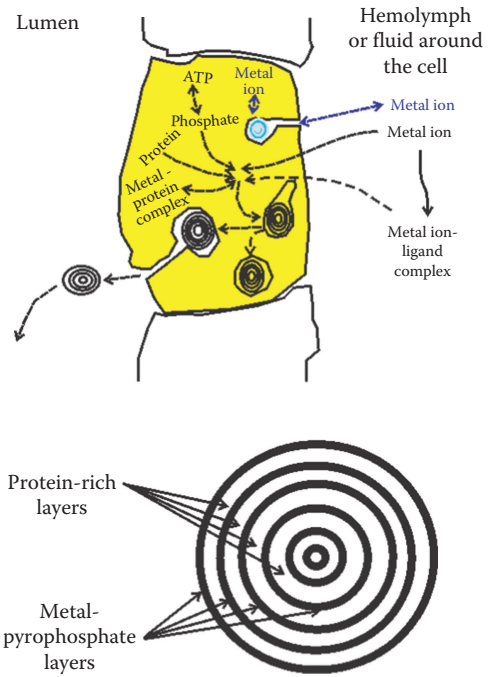

Figure 7.4 A simplified rendering of the role of intracellular granules in metal storage, detoxification, and elimination in invertebrate tissues. Two general types are shown here: calcium carbonate (blue) and calcium pyrophosphate (black/white laminated) granules. These granules are approximately 1–100 μm in diameter and are built up by concentric layers (Simkiss, 1981a). The calcium carbonate-based granules are involved in pH and calcium regulation, and are contained in vacuoles that can be connected to the cell's exterior via pores. The calcium (and magnesium) phosphate granules are usually smaller than 5 μm (Hopkin and Nott, 1979) and have concentric phosphate-rich layers separated by layers with much more protein. Metals such as cobalt, iron, lead, manganese, and zinc can accumulate to high concentration in these granules by combining with the phosphate, and in some cases, the proteins (Simkiss, 1981b). The presence and abundance of these granules can be very tissue-specific. Toxic metals can remain sequestered in calcium pyrophosphate granules within vacuoles or released from the cell. Some metals such as cadmium and mercury tend to remain more associated with proteins than granules in invertebrate tissues. (Simkiss, 1981b.)

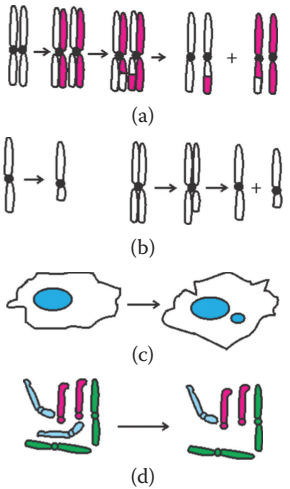

Figure 7.5 Damage to genetic materials can be assessed with a variety of cellular qualities. Increased rates of sister chromatid exchange (a) can suggest the rate of DNA damage although the exchange itself is not injurious. Beginning as a pair of homologous chromosomes (a **homolog**), four chromatids are formed. Sister chromatids in this **tetrad** (four chromatids paired as two homologs at metaphase) may exchange material. In the sister chromatid exchange assay, DNA is stained in the first round of cell division with 5-bromodeoxyuridine and the cells then synthesize unstained DNA in subsequent divisions. This results in stained and unstained chromatids that may exchange DNA in future cell divisions. This exchange is seen as chromatids with both stained and unstained segments. The rate of exchange is correlated with the frequency of DNA breakage. Chromosomes may be damaged (b, left) producing a chromosomal aberration. Viewed under the light microscope, these aberrations may appear as breaks or gaps in chromosomes. If only one chromatid in a homolog is broken, a chromatid aberration occurs (b, right). With a chromatid aberration, only one chromosome in one of the two daughter cells would be damaged. Failure of mitotic processes can produce micronuclei (c) or aneuploidy, a deviation from the usual ploidy (e.g., the usual 2*N* diploid number of chromosomes) (d).

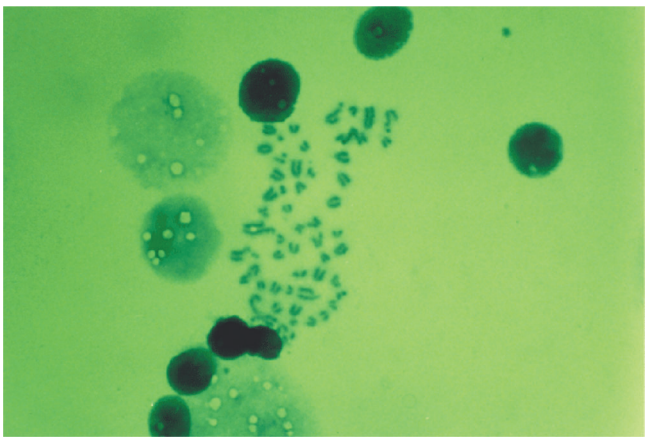

Figure 7.6 Metaphase chromosome spread from *Sigmodon hispidus* (hispid cotton rat) showing multiple chromatid breaks. (Photograph by Karen McBee.)

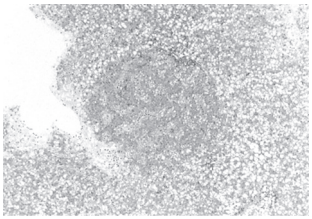

(a)

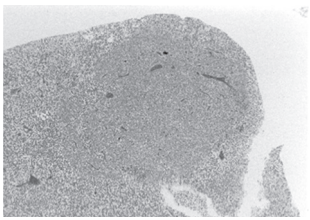

(b)

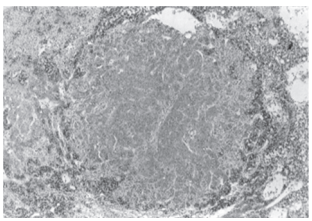

(c)

Figure 7.7 Progression of neoplasms in the medaka (*Oryias latipes*) initiated with the carcinogen, diethylnitrosamine. Fish had more rapid development of foci, and shorter times between exposure and realized effect (latent period) if they were fed the promoter, 17-β-estradiol in their diet. The top micrograph shows a basophilic focus of cellular alteration in the liver 25 weeks after exposure to diethylnitrosamine and provision of a diet containing estradiol (hematoxylin and eosin, X150, courtesy of Janis Brencher Cooke, University of California, Davis). The middle micrograph shows a solid basophilic adenoma in medaka liver exposed as already described for the top micrograph. (hematoxylin and eosin, X75, Courtesy of Janis Brencher Cooke, University of California, Davis). The bottom micrograph shows a hepatocellular carcinoma in medaka liver at 12 weeks of exposure. Note the distinct architecture of the cancer relative to the surrounding tissue (hematoxylin and eosin, X125, courtesy of Swee The, University of California, Davis).

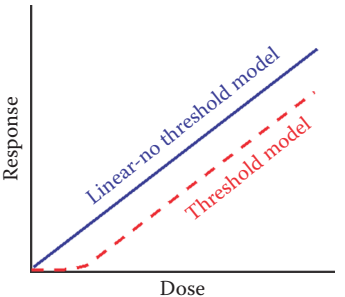

Figure 7.8 The linear-no threshold and threshold theories describe two dose-response models differing from each other at lower doses. The linear-no threshold model is described by a straight line and the threshold model is described by a "hockey stick" curve.

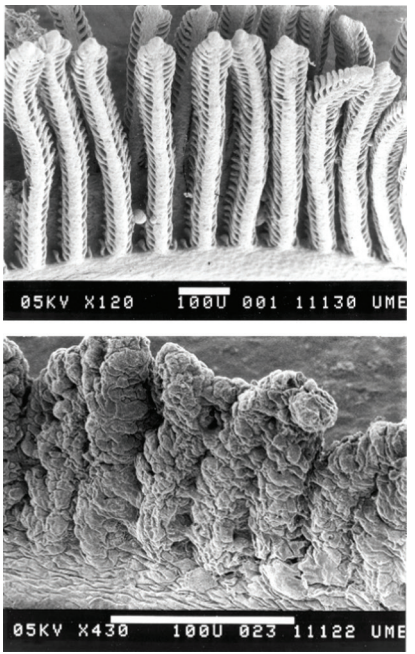

Figure 7.9 Electron micrographs of gills from Atlantic salmon (*Salmo salar*) fry. The top panel shows the normal gill morphology with primary lamellae extending (vertically here) from the branchial arch. Perpendicular to and on both sides of the main axis of each primary lamellae are the secondary lamellae. The bottom micrograph shows the gills of salmon fry after 30 days exposure to 300 $\mu g \cdot L^{-1}$ of aluminum. Note the extensive fusion of the secondary lamellae. (Courtesy of C. H. Jagoe, Florida A&M University.)

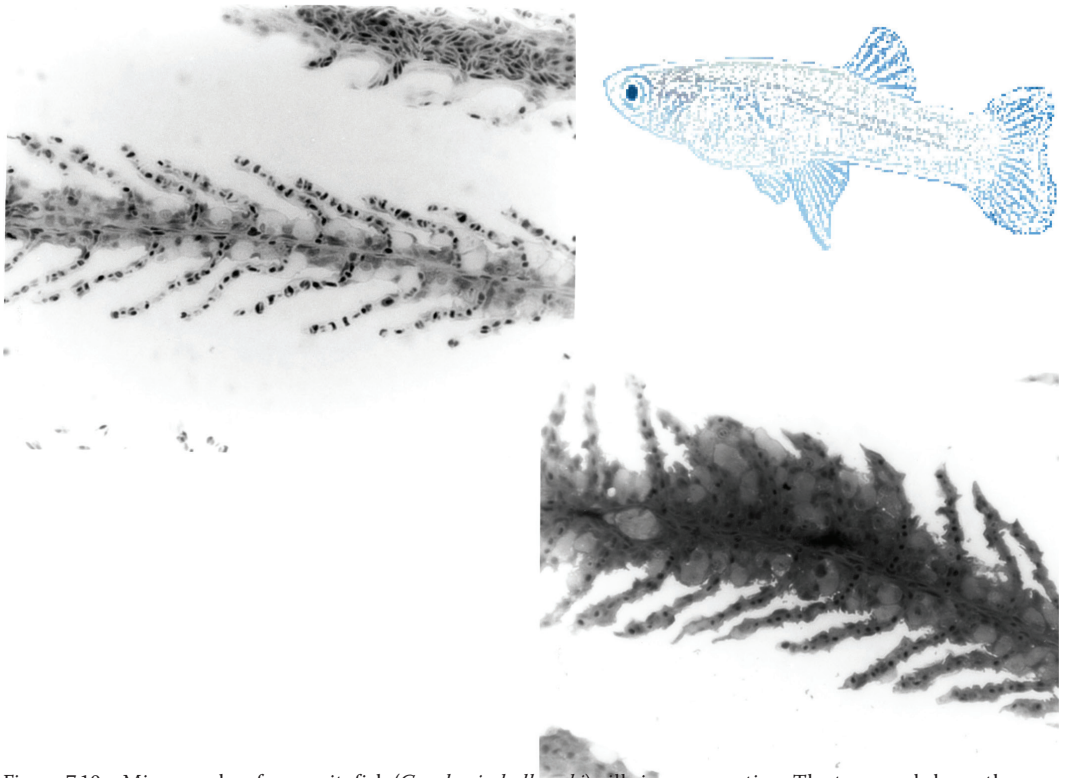

Figure 7.10 Micrographs of mosquitofish (*Gambusia holbrooki*) gills in cross section. The top panel shows the normal gill with secondary lamellae extending outward from the primary lamellae. Note the large chloride cells on the primary lamellae between the secondary lamellae. After exposure for 14 days to 60 $\mu g \cdot L^{-1}$ of inorganic mercury (bottom panel; see Jagoe et al. 1996), the primary lamellar epithelium began filling in the spaces between adjacent secondary lamellae. The chloride cells (large cells with lightly stained cytoplasm) were involved to a large extent in this hyperplasia, becoming larger (hypertrophy) and more abundant on the primary lamellae. The secondary lamellae appeared to shorten or disappear as a consequence. Although reported elsewhere in response to gill irritation with toxicants (e.g., Tuurala and Soivio, 1982), no necrosis, separation of epithelium from the secondary lamellae, or inflammation were noted. (Toluidine blue; distance between secondary lamellae at their base is circa 20 μm; Courtesy of C. H. Jagoe, Florida A&M University.)

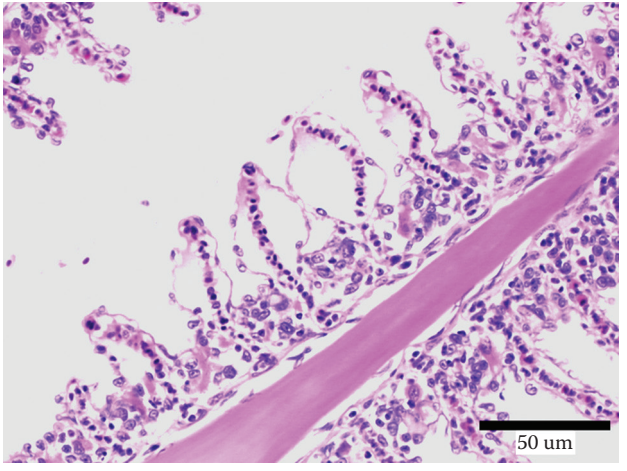

Figure 7.11 Gill epithelial lifting, indicative of edema between the outer epithelial layer and underlying blood sinusoid. (Photomicrograph and general description provided by W. Vogelbein, Virginia Institute of Marine Science.)

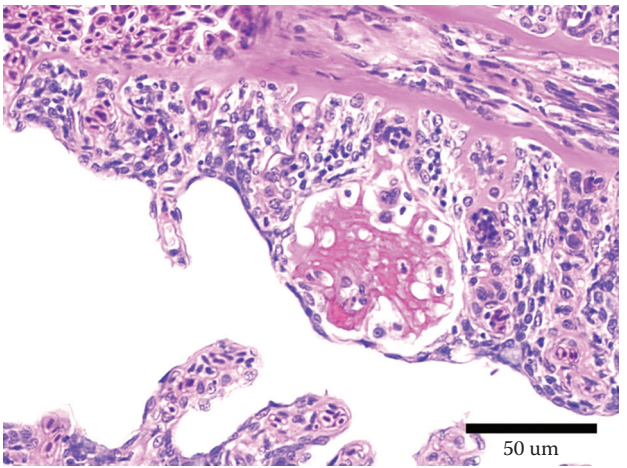

Figure 7.12 Mild hyperplasia and thrombosis if a lamellar sinusoid of mummichog (*Fundulus heteroclitus*) gill. (Photomicrograph and general description provided by W. Vogelbein, Virginia Institute of Marine Science.)

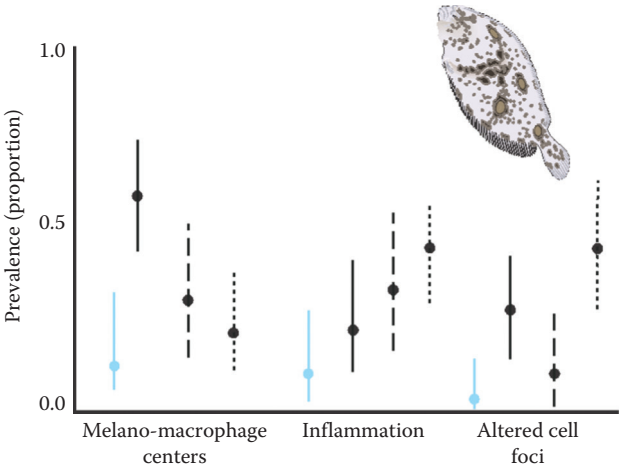

Figure 7.13 Prevalence of flounder liver lesions sampled in autumn from four British estuaries that differ in levels of pollution (Stentiford et al. 2003). Prevalence (proportion of examined fish livers) and sample sizes were extracted from Table 2 of the original publication to generate the 95% (asymmetric) confidence intervals via the Wilson method (Newcombe and Altman, 2000) for the observed proportion. Inflammation and altered cell foci have already been described as biomarkers. The melano-macrophage centers referred to here are centers of pigment-containing macrophages and leucocytes associated with chronic inflammation (Agius and Roberts, 2003; Leknes, 2007). (Alde: Solid blue 95% confidence intervals; Tyne: Solid black 95% confidence intervals; Tees: Long black dash 95% confidence intervals; Merser: Short black dash 95% confidence intervals.)

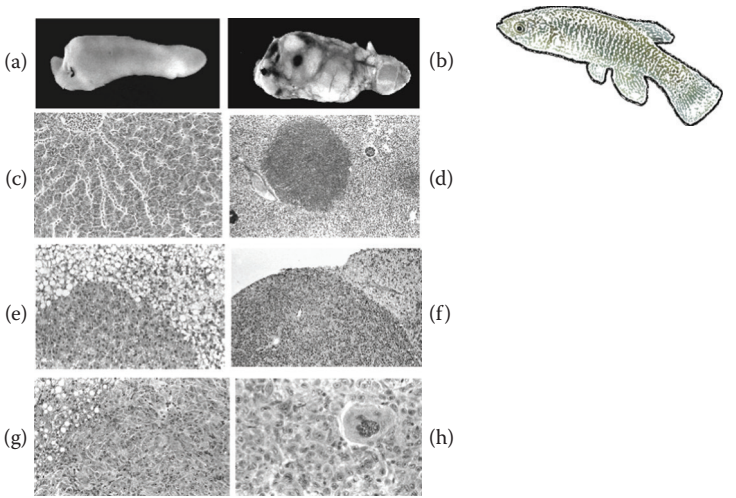

Figure 7.14 Gross and histopathologic anatomy of the liver of mummichogs, *Fundulus heteroclitus*, inhabiting uncontaminated and PAH-contaminated environments in the Elizabeth River, Virginia, United States. (a) Normal healthy liver of mummichog from uncontaminated environment. (b) Liver of mummichog from a PAH-contaminated habitat exhibiting multiple focal lesions, tumorous nodules and cystic lesions. (c) Histologic section of normal healthy mummichog liver showing typical tubulosinusoidal architecture (hematoxylin and eosin; X200). (d) Altered hepatocellular focus (eosinophilic focus) in liver of exposed mummichog (hematoxylin and eosin; X40). (e) High magnification of eosinophilic focus in Figure (d) showing subtle blending of the lesion border with surrounding normal tissue (hematoxylin and eosin; X150). (f) Large hepatocellular adenoma showing swelling of liver capsule and well-demarcated border with normal liver tissue (hematoxylin and eosin; X75). (g) Hepatocellular carcinoma showing sharp locally invasive border with normal liver tissue and cellular and nuclear pleomorphism of the tumor cells (hematoxylin and eosin; X200). (h) High magnification of a hepatocellular carcinoma showing cellular and nuclear pleomorphism typical of poorly differentiated highly malignant neoplasms (hematoxylin and eosin; X400).

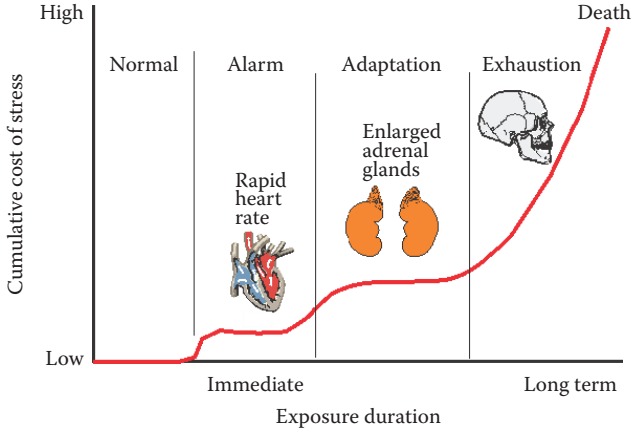

Figure 8.1 The three stages of the General Adaptation Syndrome (GAS). In the initial alarm phase, immediate responses to stress include increases in blood pressure and heart pumping rate. Cells of the adrenal cortex also discharge their granules into the blood. With longer durations of exposure, adrenal enlargement occurs and cells of the adrenal cortex may become rich in granules again (Selye, 1973). Finally, after sufficient exposure, the ability of the body to compensate for the stressor's effects is exceeded and the individual slowly becomes exhausted. If the stress continues, the individual will die.

Figure 8.2 Hugo Schulz (1853–1932). Pioneer in the study of hormesis.

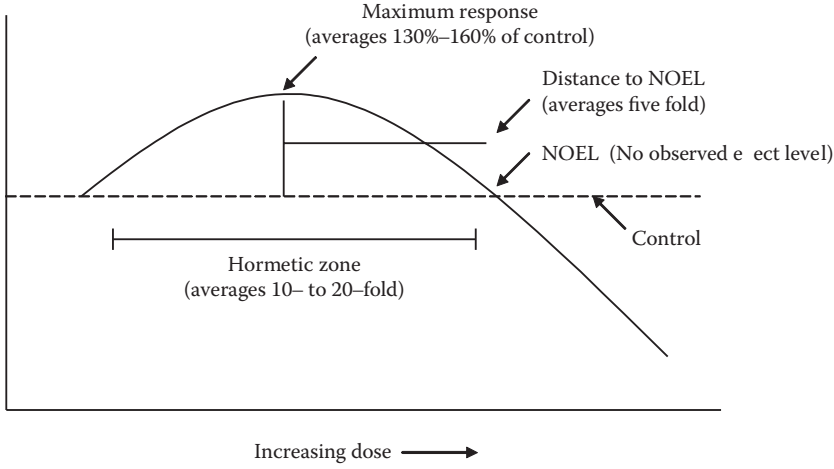

Figure 8.3 Dose–response curve depicting the quantitative features of hormesis.

Figure 8.4 Fish (*Fundulus heteroclitus*) exposed to no (top three individuals) or 10 mg·L^{-1} of Pb^{2+} (bottom two individuals) during development. The effect threshold is typically 1 mg·L^{-1} of Pb^{2+}. Note the failure of the exposed individuals to uncurl after hatching. (Courtesy of P. Weis, UMDNJ—New Jersey Medical School.)

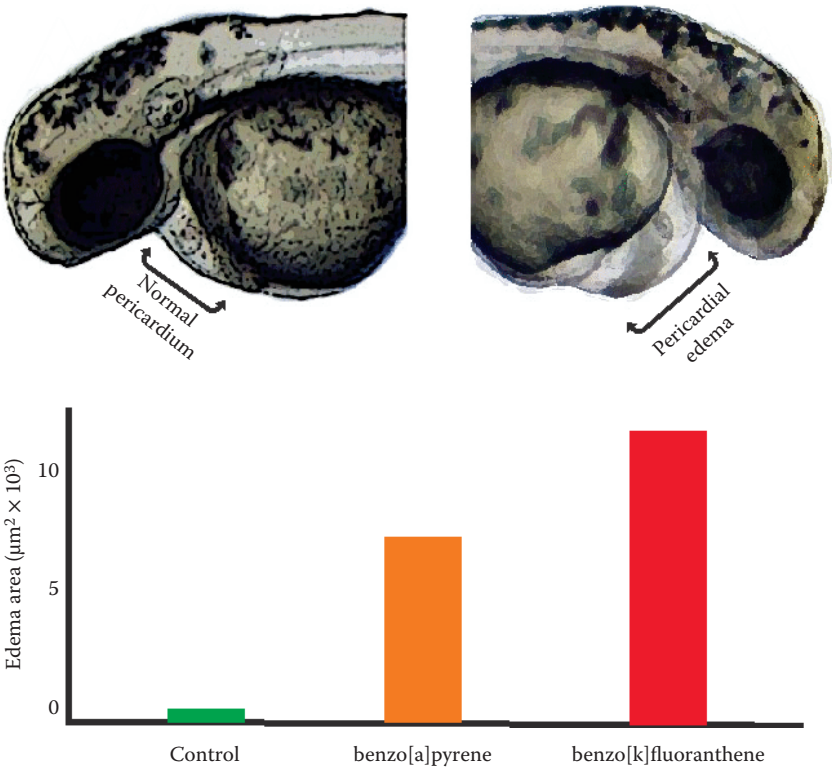

Figure 8.5 Pericardial edema of zebrafish (*Danio rerio*) larvae expressed as increased pericardial area for dosed larvae relative to controls (Incardona et al. 2011). Edema was measured after larvae were exposed from 4 to 48 hours postfertilization to control (green, dimethyl sulfoxide solvent only), 40 μM benzo[a]pyrene (orange), or 40 μM benzo[k]fluoranthene (red). Pencil sketch images show a normal pericardium (left) and an extremely edemic pericardium of a larva that had been exposed to benzo[k]fluoranthene. The difference in toxicity between the two 5-ring PAHs is a consequence of their interactions with the aryl hydrocarbon receptor discussed in Vignette 6.1 as being pivotal to cytochrome P450 induction in vertebrates. Exposure to these PAHs results in different tissue-specific inductions of CYP1A. Functional consequences were noted such as embryo heart rate that decreased from control (128 beats/minutes, bpm) to benzo[a]pyrene-exposed (120 bpm) to benzo[k]fluoranthene (93 bpm) treatment. (Original photographs from Figure 1A and D of Incardona et al. (2011) were digitized, modified electronically, and rendered to pencil sketches to produce the upper illustrations. The data shown in the lower histogram were visually extracted from their Figure 1E.)

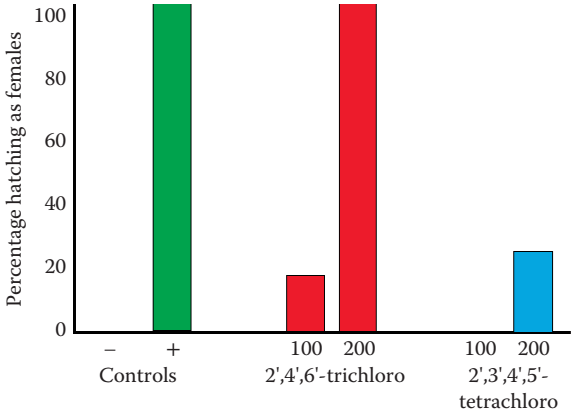

Figure 8.6 The percentage of hatchling turtles that are females after exposure to PCBs. Eggs were incubated at 26°C to 28°C that will cause all hatchlings to be males (negative control). Eggs in the negative control treatment (–) were spotted on their surfaces only with the solvent used for the other treatments (95% ethanol) and those in the positive control treatment (+) were spotted with the hormone, 17β-estradiol The two PCBs spotted onto eggs were 2′, 4′, 6′-trichloro-4-biphenylol (labeled 2′, 4′, 6′-trichloro) and 2′, 3′,4′, 5′-tetrachloro-4-biphenylol (labeled 2′,3′,4′,5′-tetrachloro). Both were dosed at 100 and 200 µg per egg as indicated above the PBC labels. (Modified from Figure 1 of Bergeron, J.M., et al. *Environ. Health Perspect.*, 102, 780–781, 1994. With permission.)

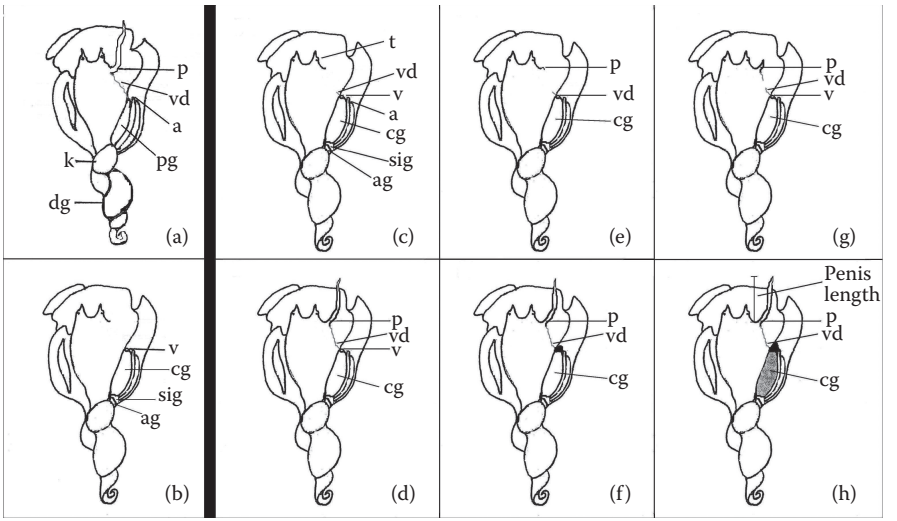

Figure 8.7 Anatomical features of (a) a normal male, (b) a normal female, and (c–h) the effects of imposex on the reproductive systems of female *Thais clavigera* at different vas deferens sequence index (VDSI) stages: (c) develops vas deferens at the region ventral to the genital papilla (stage 1); (d) penis development starts behind the bottom of right tentacle (stage 2) ; (e) develops distal region of vas deferens at the base of small penis (stage 3); (f) development vas deferens completes and the penis enlarges to the size similar to male (stage 4); (g) vulva is displaced by the overgrowth tissue of vas deferens and become invisible, blister like protuberances may appear around the site of papilla (stage 5); (h) lumen of capsule gland contains material of aborted egg capsule and formed a translucent or brown mass (stage 6). a, anus; ag, albumen gland; cg, capsule gland; dg, digestive gland; k, kidney; p, penis; pg, prostate gland; t, tentacle; v, vulva; and vd, vas deferens. (Modified from Gibbs, P.E., et al. *J. Mar. Biol. Assoc. UK*, 68, 715–731, 1988; Li,Z., The Incidence of Imposex in Hong Kong and the Value of *Thais clavigera* (Gastropoda: Muricidae) as a Bioindicator of TBT Pollution, PhD Diss., The University of Hong Kong, Hong Kong, 2000. With permission.)

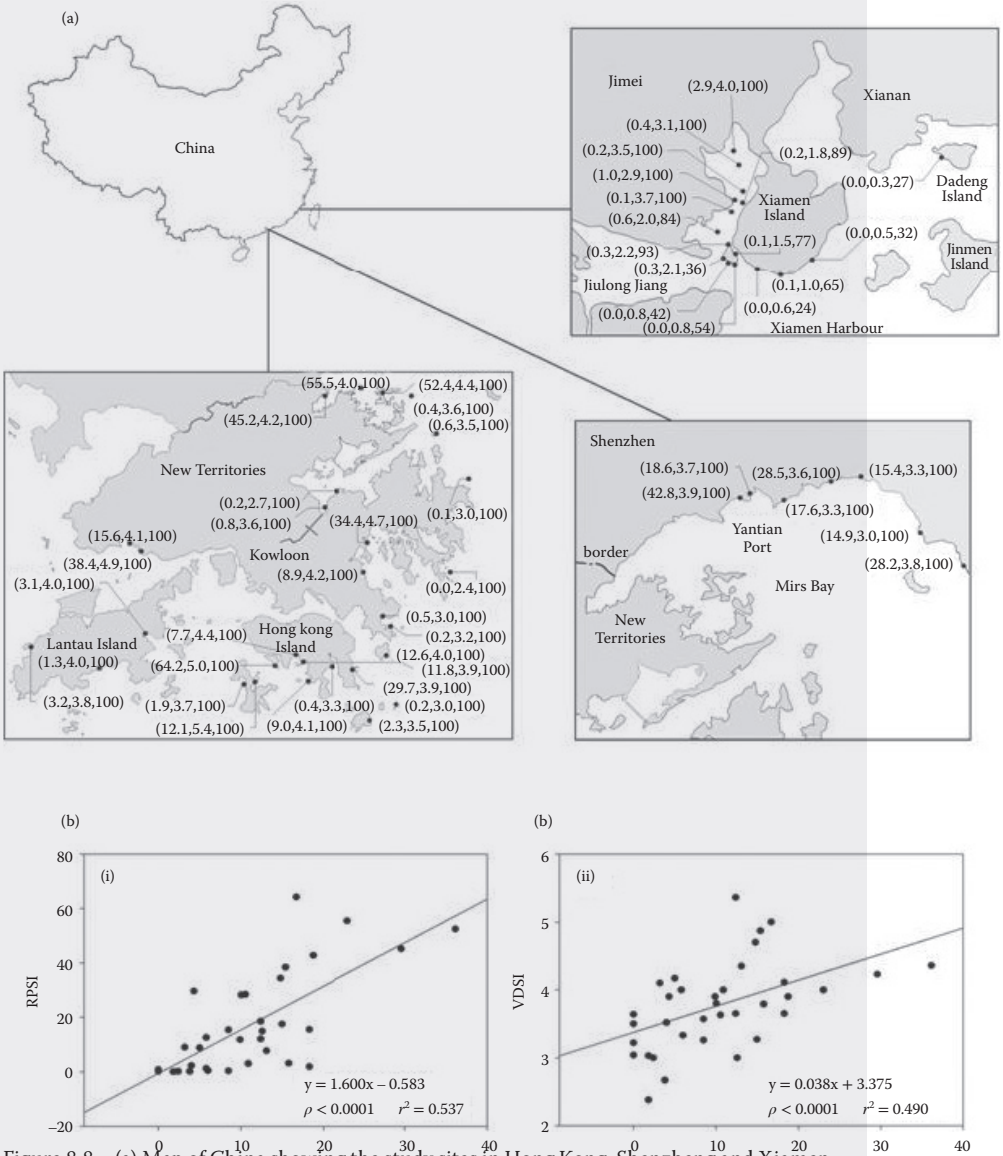

Figure 8.8 (a) Map of China showing the study sites in Hong Kong, Shenzheng and Xiamen. The figures in brackets are RPSI, VDSI, and percentage of imposex (%), respectively, in *Thais clavigera*. Data were extracted from Leung et al. (2006) (Hong Kong), Chan et al. (2008) (Shenzheng), Tang et al. (2009), and Wang et al. (2008) (Xiamen). (b) The relationship between (i) RPSI or (ii) VDSI and the tissue concentration of TBT in *T. clavigera*. Results of the regression analysis are also shown.

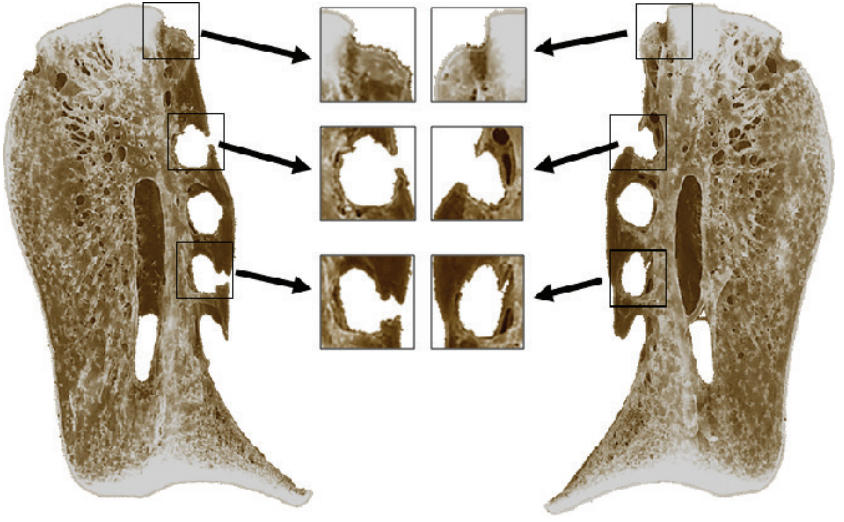

Figure 8.9 Example of fluctuating asymmetry: paired cranial bone *Ceratohyale* from Pacific herring, *Clupea pallasii*.

Figure 8.10 Leaf of seagrass *Halophila ovalis* (Alismatales, Hydrocharitaceae). Distances between vein interceptions and length of veins can be used for measuring fluctuating asymmetry. (From Ambo-Rappe, R., et al. *Ecol. Indic.*, 8, 100–103, 2008; Ambo-Rappe, R., et al. *J. Environ. Chem. Ecotoxicol.*, 3, 149–159 2011.)

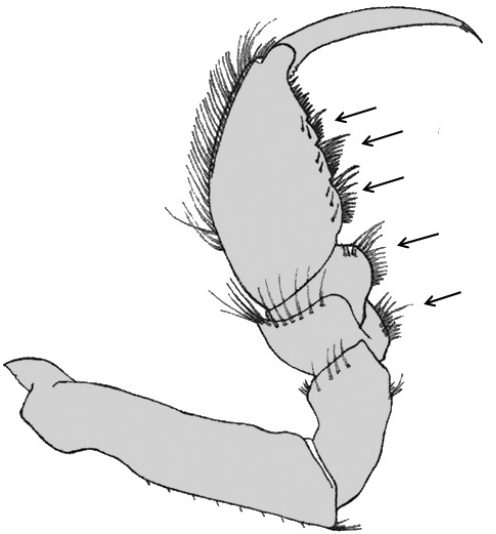

Figure 8.11 A thoracic leg of *Saduria entomon* (Crustacea, Isopoda) with characters (groups of chaeta on internal surface shown by arrows) convenient for analysis of fluctuating asymmetry. (Modified from Lajus, D.L., et al. *Ann. Zool. Fennici*, 40, 411–419, 2003. With permission.)

Figure 8.12 Bones of Atlantic salmon *Salmo salar* (Teleostei, Salmonidae) with landmarks used for analysis of fluctuating asymmetry. (From Yurtseva, A., et al. *J. Appl. Ichthyology*, 26, 307–314, 2010.)

Figure 8.13 Basal part of *Zostera capricorni* (Liliopsida, Zosteraceae) leaf. Distances between interceptions of median vein and lateral veins (arrowed) can be used for measuring translational fluctuating asymmetry. (From Ambo-Rappe, R., et al. *Environ. Bioindic.*, 2, 99–116, 2007.)

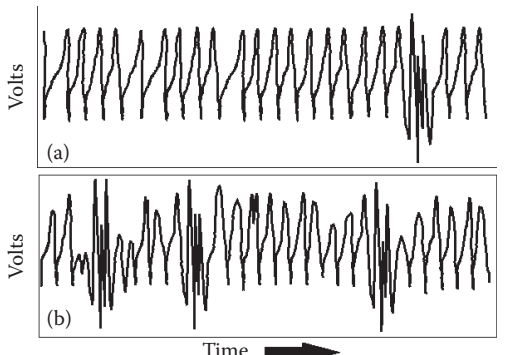

Figure 8.14 Patterns for ventilation and coughing for fish. In panel a, ventilation (small evenly spaced peaks) and coughing (strong, rapid cluster of peaks toward the right-hand side) are traced through time for a control individual. Ventilation frequency increases and amplitude decreases, and cough frequency increases often with exposure to contaminants (panel b).

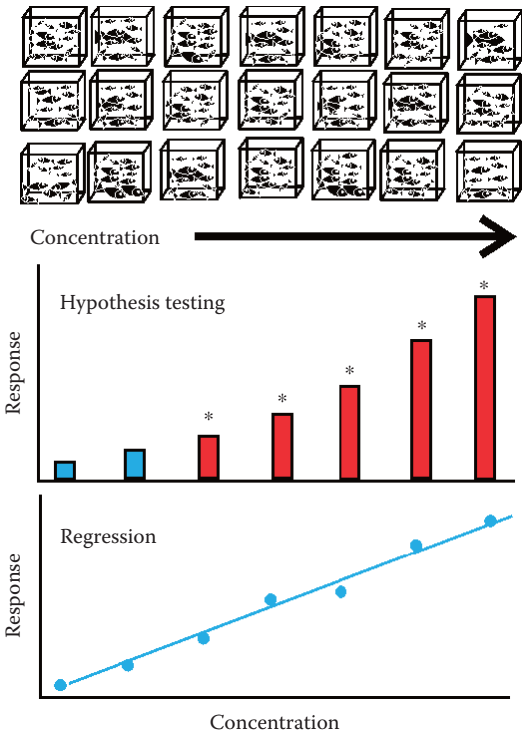

Figure 8.15 For regulatory testing, sublethal effects are most often analyzed using hypothesis testing methods. A series of tanks (seven sets of triplicates here) receiving increasing concentrations of contaminant are used to estimate the response for each concentration, including a control set of tanks. Data are then tested to determine if the response at each concentration was significantly different from that of the control. In the middle panel,* is used to indicate exposure concentrations with effects that are significantly different from the control. Here, the responses of the five highest concentrations (red) were significantly different from the control: the lowest exposure concentration was not significantly different from the control. These data can also be used in regression models to develop a predictive relationship between concentration and effect (bottom panel).

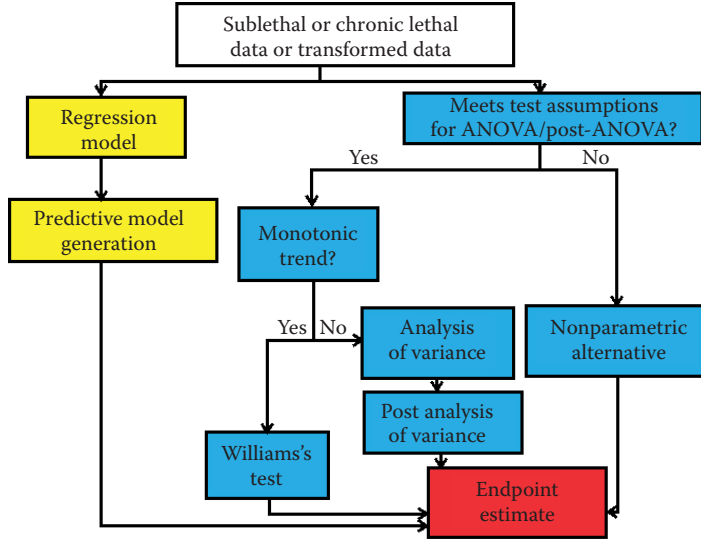

Figure 8.16 A flow diagram of conventional methods applied to analyze sublethal (and chronic lethal) effects.

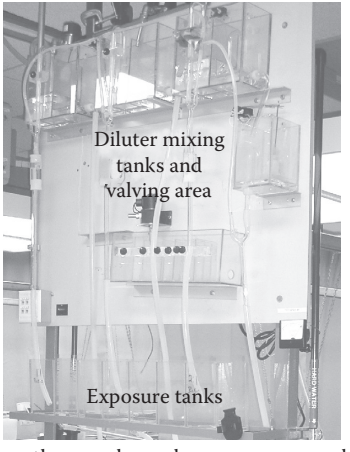

Figure 9.1 Proportional diluters, such as the one shown here, are commonly used to deliver a test water flow of a predetermined series of toxicant or effluent concentrations to replicate test tanks containing experimental organisms. Various proportions of dilution water and toxicant solution (or effluent) are mixed in the dilutor tanks and valving area. Waters with the resulting series of toxicant (or effluent) concentrations are then delivered to tanks (Exposure Tanks). Each exposure tank contains a specific number of experimental organisms.

Figure 9.2 An avian toxicity testing facility in which a series of doses are fed to subsets of mallard ducks so that lethal or nonlethal effects can be quantified.

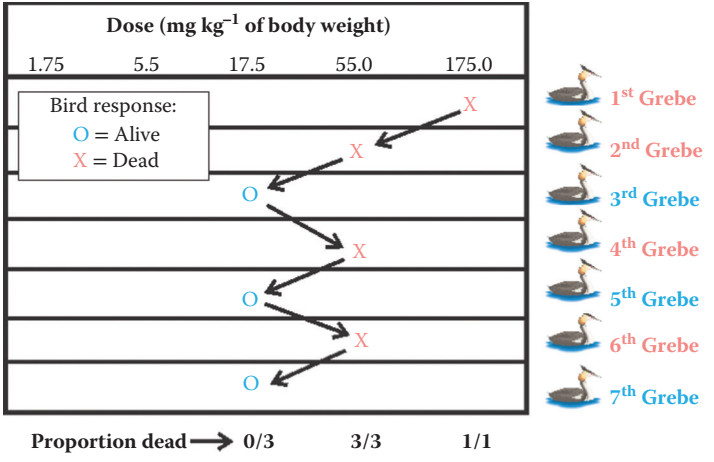

Median lethal dose = 29.6 mg kg^{-1}
Approximate 95% Confidence interval = 17.5 to 55.0 mg kg^{-1}

Figure 9.3 Up-and-down experimental design for estimating LD50.

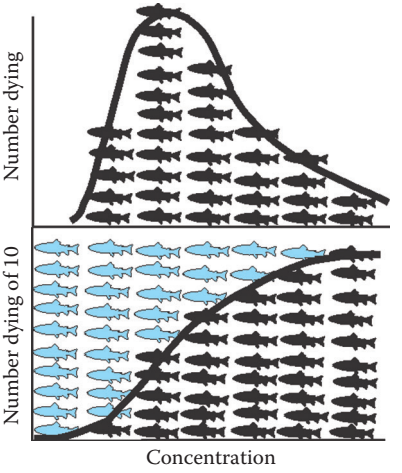

Figure 9.4 The individual effective doses (IED) concept and the analysis of dose–response lethality data. The top panel depicts the distribution of IEDs among 35 fish taken randomly from a population. Each individual's response was placed into a category (column) based on whether its IED fell into one of six different ranges of IED values. The distribution of such IED values within a population is thought to be log normal as evidenced by an asymmetric curve with a few very tolerant individuals. The bottom panel shows the results of exposing sets of 10 individuals from this same population to a series of doses for a set time. Surviving fish (blue) had IED values greater than the exposure dose and dead fish (black) had IED values less than or equal to the exposure dose. The result is a typical, sigmoidal dose–response curve.

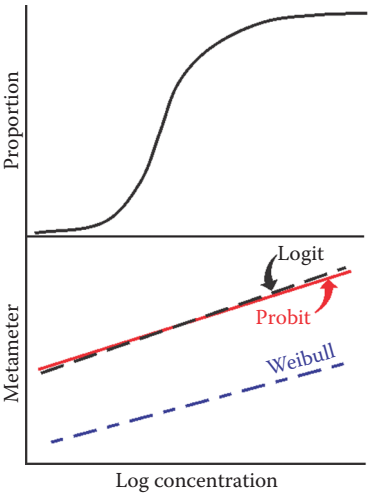

Figure 9.5 The typical sigmoid curve for concentration–response data (top panel) and lines resulting from the probit (solid black), logit (dashed black), and Weibull (dashed blue) transformations (bottom panel).

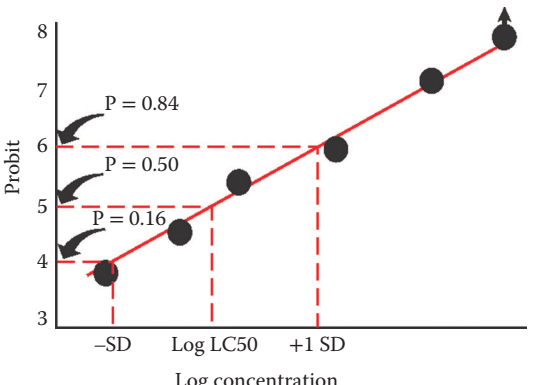

Figure 9.6 Based on a log normal model, probit methods can be used to generate a line from concentration-effect data. An estimate of the log LC50 ± one standard deviation can be approximated from such a graph. Note that a point with 100% mortality is often indicated by an arrow attached to the data point. This indicates that 100% mortality would likely have occurred before the time endpoint and some lower concentration likely would have produced 100% at exactly that time endpoint. Other, more rigorous methods discussed in the text provide better estimates.

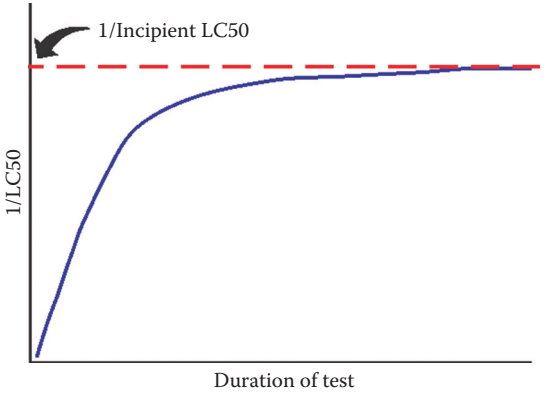

Figure 9.7 The incipient lethal concentration is estimated as the point at which the curve of 1/LC50 versus duration of exposure begins to run parallel to the *x* axis.

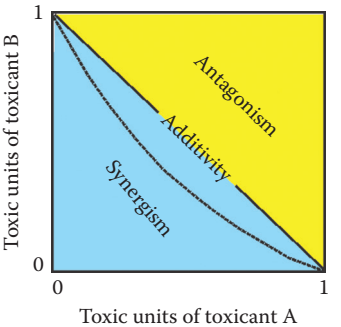

Figure 9.8 An illustration of the isobole approach. The solid line connecting 1.0 on both axes reflects additivity and deviation from additivity if a point lies to the lower left (synergism) or upper right (antagonism) of the figure. The dashed line represents a hypothetical hyperbole for two toxicants A and B displaying synergistic joint action.

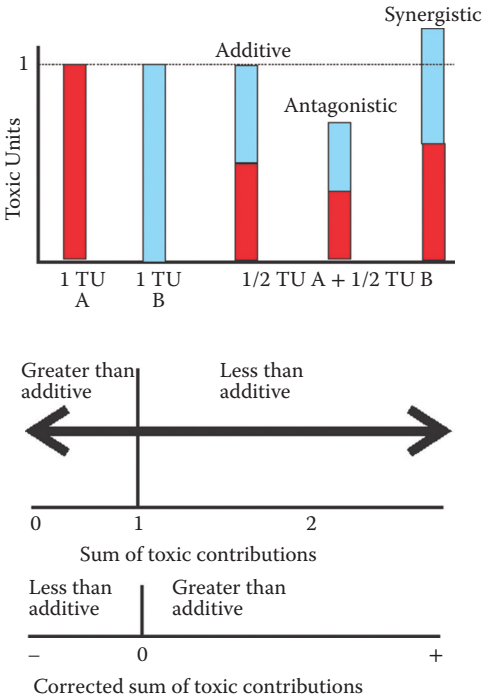

Figure 9.9 The combined effect of toxicants may be quantified by expressing toxicant concentrations in mixtures as toxic units (TU) (upper panel). If the realized effect expressed in terms of TU is less than the calculated sum of TU for both toxicants A and B in a mixture, the chemicals are said to be antagonistic. Their effect is synergistic if the realized effect is greater than the calculated effect based on their individual actions. The two scales include the nonlinear scaling of Marking and Dawson (1975) (middle) and additive index (lower), which is a linear scaling of combined toxicant effect.

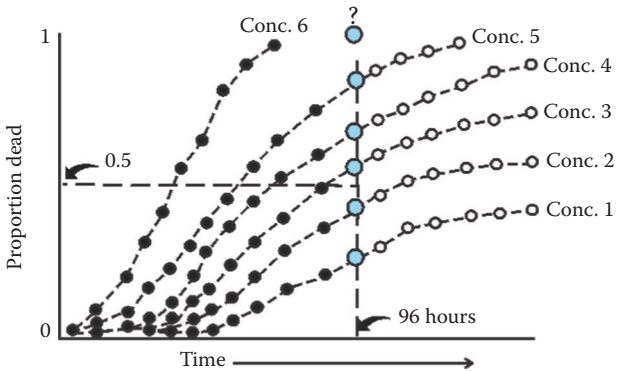

Figure 9.10 An idealized time course of mortality occurring at six different concentrations. Note that, if only data from 96 hours were used, only five points (blue) with perhaps some estimate of a sixth for Concentration 6 (blue with question mark) would be available to calculate the LC50. In contrast, many more data points (approximately 70 points) would be gathered by 96 hours if times-to-death for individuals were noted instead of the final proportion dying in each tank. For a more complete data set, observations could be made that noted mortality occurring at intervals before (black) and after (white) 96 hours.

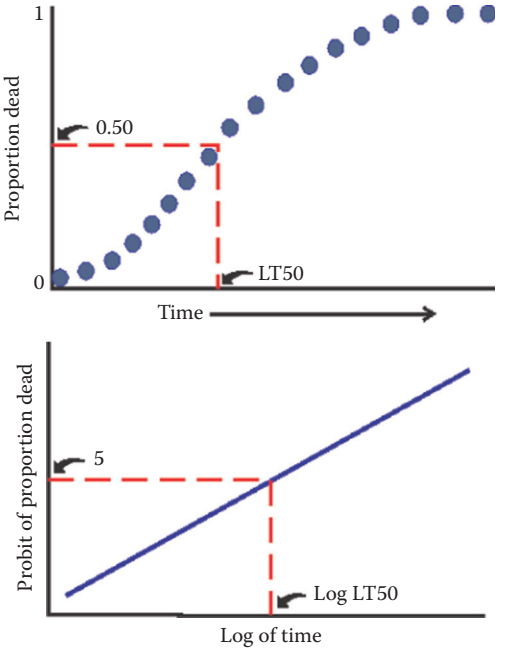

Figure 9.11 Linear transformation of time-to-death data assuming a log normal model. A sigmoidal curve is generated if the cumulative proportion of the exposed individuals that have died is plotted against exposure time (upper panel). Under the assumption of a log normal model, a straight line is produced (lower panel) if log time is plotted against the probit of the proportion dead. A curve which is not straight, but instead has a break in its slope, is called a **split probit**. Traditionally, a split probit is assumed to reflect either two distinct mechanisms of toxicity at the beginning and later in the exposure, or two distinct subpopulations of individuals in the exposed group that differ in tolerance to the toxicant. A third possibility exists, the log normal model is an inappropriate model for the data, but is rarely assessed.

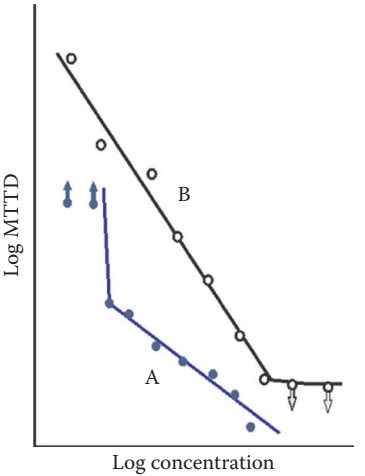

Figure 9.12 Incipiency for the time-to-death approach. Chemical A (blue circles) has a distinct incipient median time-to-death (MTTD). Below a certain concentration, 50% of exposed individuals will live indefinitely relative to the effect of toxicant A. Note that the two lowest concentrations resulted in less than 50% mortality regardless of how long the individuals were exposed. Some toxicants (B, black circles) may show no evidence of incipiency. There may also be a minimum time to get a response, e.g., individuals can only die so fast regardless of the toxicant concentration. Toxicant B in the diagram has such a threshold. (Arrows attached to a point signify that the "true" value is probably in the indicated direction from the point; e.g., the true log MTTD for the last point on curve B is less than the value of the last point.) (Modified from Figure 5 in Sprague, J. B., *Water Res.*, 3, 793–821, 1969 and Figure 4 in Newman, M. C., *Quantitative Methods in Aquatic Ecotoxicology,* Lewis Publishers, Boca Raton, FL, 1995.)

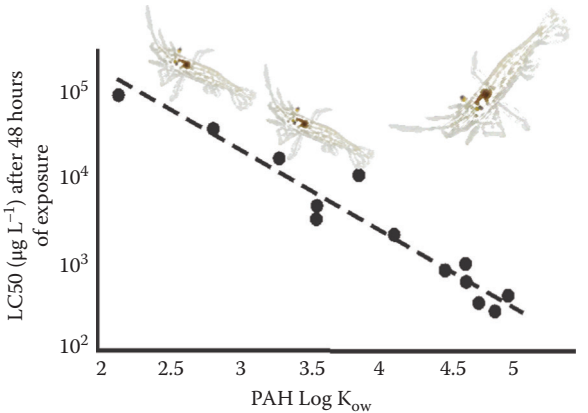

Figure 9.13 An illustration of lipid solubility effect on LC50 of grass shrimp (*Palaemonetes pugio*) exposed to a series of PAH, commonly associated with oil spills. (Data from Unger et al. *Environ. Toxicol. Chem.* 27, 1802–1808, 2008.)

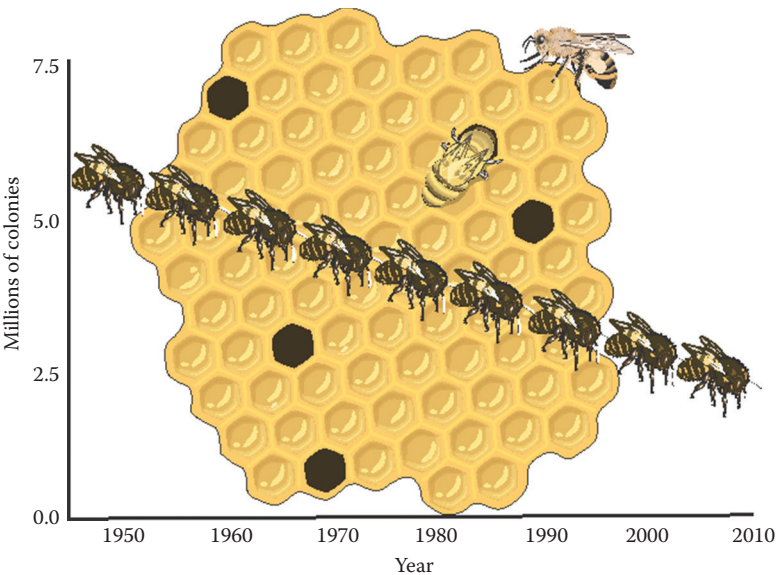

Figure 10.1 The decline in honey bee colonies in the United States as estimated by Pettis and Delaplane (2010) from National Agricultural Statistics Services records. (The line depicted with honey bees is the downward trend approximated from 1945 to 2008 data points in Figure 1 of Pettis, J.S. and K.S. Delaplane, *Apidologie,* 2010, 1–8, 2010.)

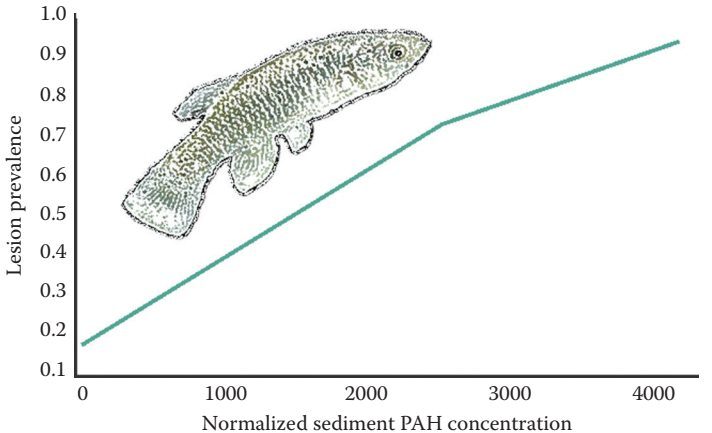

Figure 10.2 Prevalence of liver lesions for mummichog (*Fundulus heteroclitus*) inhabiting sites on the Elizabeth River (Virginia, United States) with different concentrations of polynuclear aromatic hydrocarbon (PAH) in sediments. Prevalence is expressed as the proportion of sampled individuals with lesions and PAH concentration was expressed as (milligram PAH per kilogram of dry sediment)/(sediment total organic carbon content/100). (See Vignette 7.2 for details.) Figure derived from Figure 6.1 in Newman, M.C., *Quantitative Ecotoxicology, 2nd Edition*, Taylor & Francis/CRC Press, Boca Raton, Florida, 2013.)

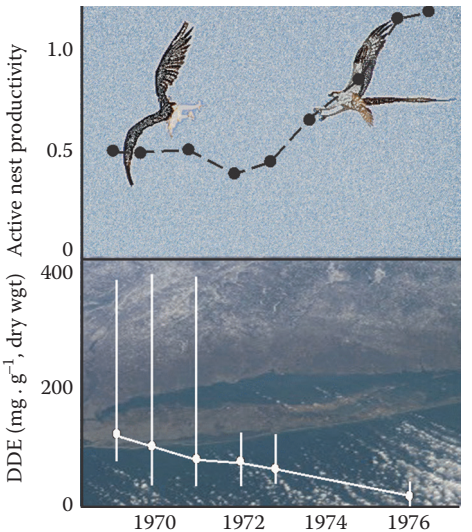

Figure 10.3 The gradual increase in active nest productivity (average number of young fledged per active nest) of Long Island Sound osprey. Nesting success was extremely low before the widespread banning of pesticides such as dichlorodiphenyldichloroethylene (DDE). The nest productivity slowly recovered (top panel) as DDE concentrations decreased in eggs from osprey nests (bottom panel), suggesting that DDE was a significant risk factor in nest failure. (Modified from Figure 1 of Spitzer et al. (1978), background images drawn from photographs of M. Newman and NASA.)

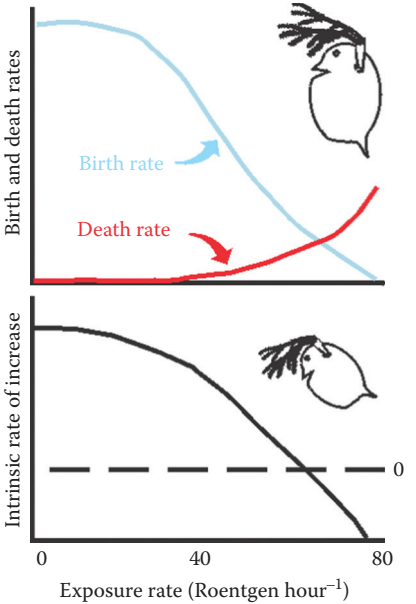

Figure 10.4 Birth, death, and intrinsic rate of increase for *Daphnia pulex* exposed continuously to different amounts of ^{60}Cobalt γ radiation. Age-specific survival (l_x) and fertility (m_x) rates were measured for females exposed to different levels of radiation, and the intrinsic rate of increase estimated by iterative solution of the Euler–Lotka equation. (Modified from Figures 1 and 2 of Marshall, J.S., *Ecology*, 43, 598–607, 1962.)

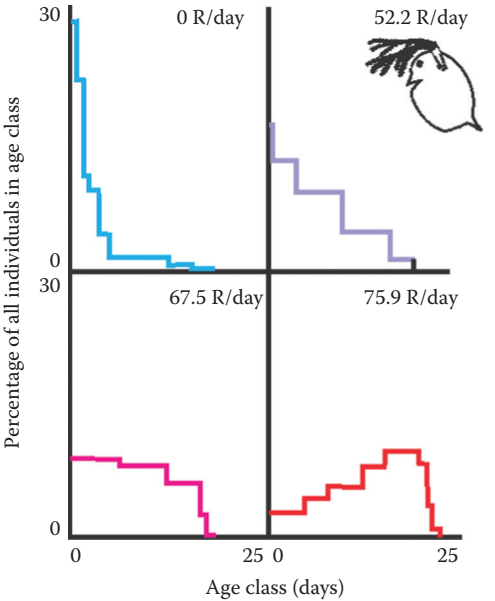

Figure 10.5 Stable age structures of *Daphnia pulex* exposed to 0–75.9 R·h^{-1} of ^{60}Cobalt γ radiation. Note the gradual trend toward a structure with few neonates as dose rate increases. (Adapted from Figure 3 of Marshall, J.S., *Ecology*, 43, 598–607, 1962.)

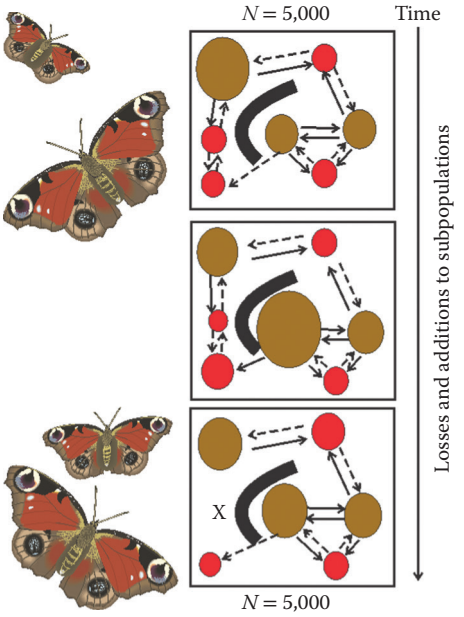

Figure 10.6 An illustration of metapopulation dynamics. A mosaic of population patches are present at the onset (upper panel) with some of the 5000 individuals in the composite metapopulation being in inferior patches (red) and others in good or superior patches (brown). Barriers to migration may exist such as that depicted with a black arch in the center of the panel. Some patches are net source (solid arrows) and sinks (dashed arrows) of individuals. Numbers of individuals in the subpopulation might fluctuate (or even drop to zero as depicted with a red X in the lower panel) but the general metapopulation size remains relatively constant here.

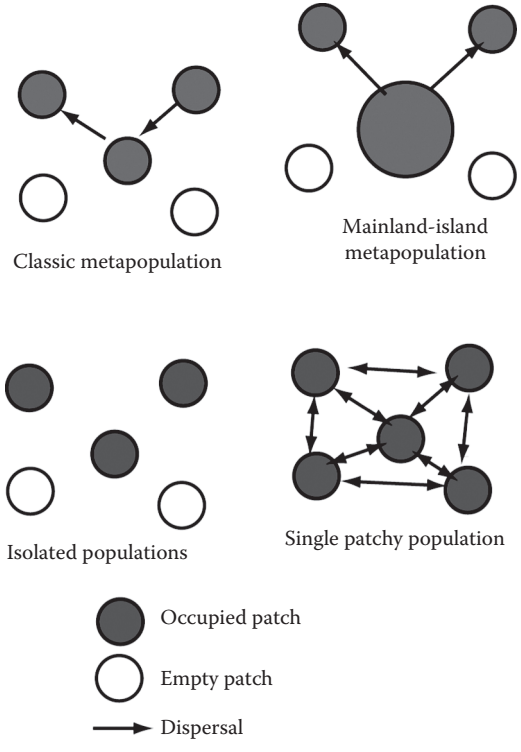

Figure 10.7 Kinds of patch structure in a patchy environment. The models described here generally fit the single patchy population with varying arrangements and distances between patches.

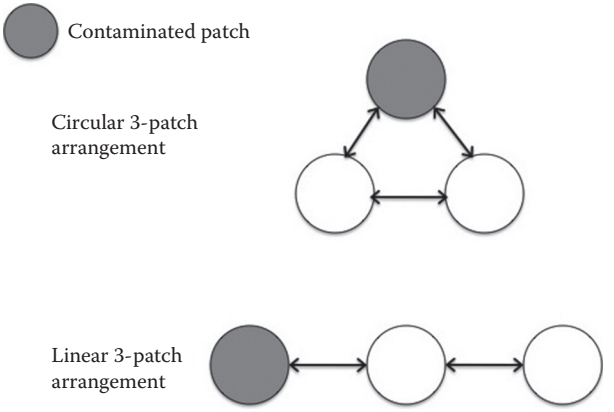

Figure 10.8 Arrangement of habitat patches in the patchy population models used in our studies. The contaminated patch could be in any position within the model landscape. Distances between the habitats could also be altered, changing the rate of migration between each habitat patch.

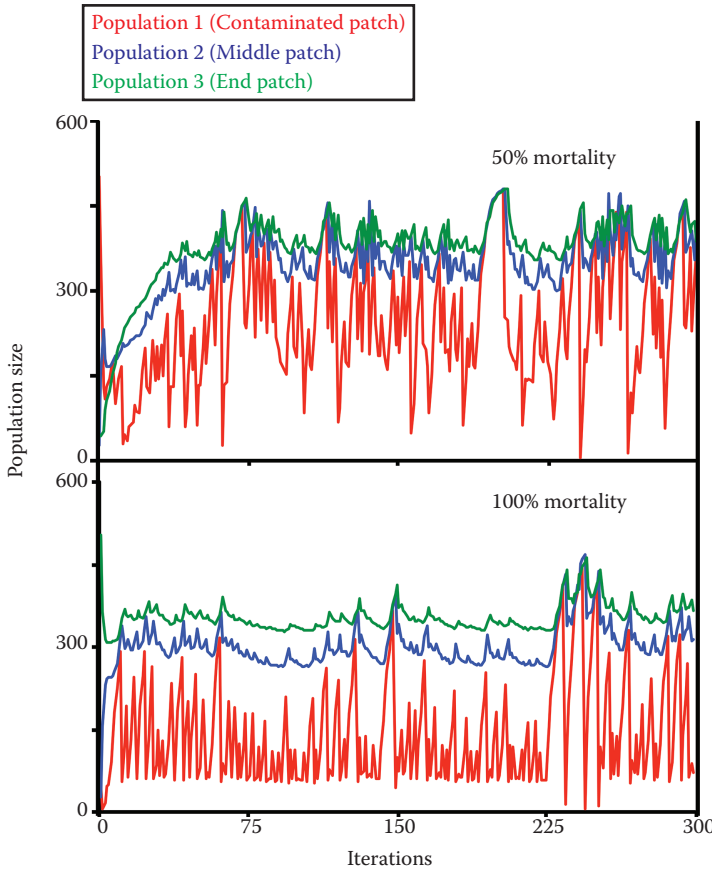

Figure 10.9 Action at a distance. In the three patch simulations where the end contaminated patch has a toxicant concentration equal to an EC50, (top panel) the dosed patch has wide fluctuations. However, there is an occasional overlap among all three populations. The populations in non-dosed habitat patches are below the carrying capacity of 500 and exhibit fluctuations. Even at an EC100 (bottom panel) in the dosed patch, organisms are still extant and occasionally reach numbers comparable to the non-dosed patches. In both simulations, the population in the dosed habitat patch is rescued by the other patches. The initial population size for each habitat patch was 100, and the distances between the patches are equal.

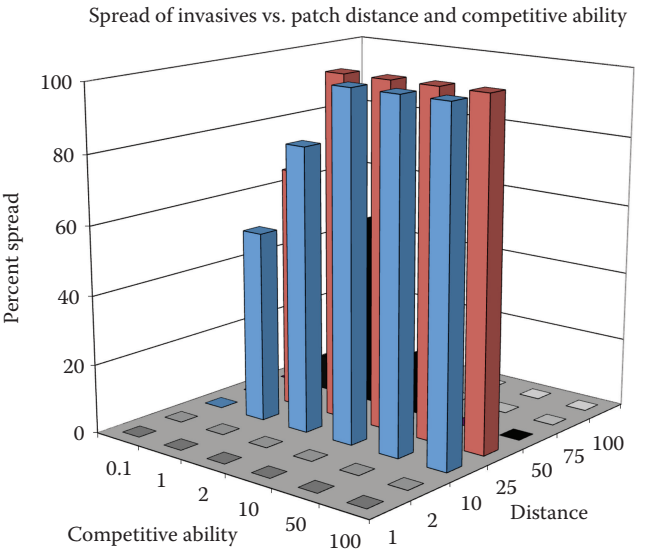

Figure 10.10 Interaction between distance between patches, competitive ability, and spread of the invasive. Note that a range of outcomes can occur depending on the specific distances and competitive ability in this system. Even at a competitive ability far above the native species invasion does not occur if the patches are either too close or too far away. At a distance of 50 units, the optimal competitive ability is actually twice that of the native.

Figure 10.11 Typical and melanic peppered moths, *Biston betularia cognataria*. At rest, the wings span 4–5 cm. (Photograph by Bruce Grant.)

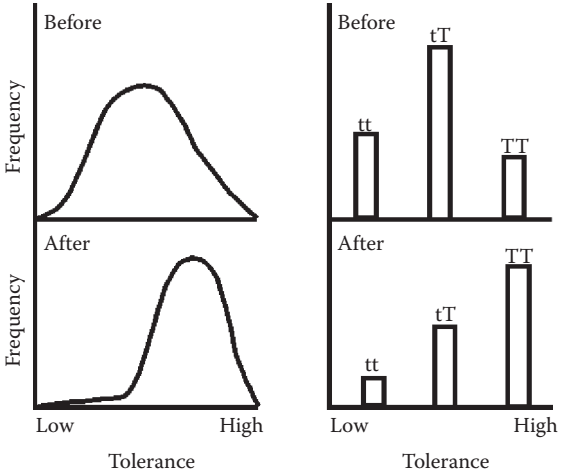

Figure 10.12 Shifts in tolerance expected under polygenic (left side of figure) or monogenic (right side of figure) control. With polygenic control, differences in tolerance will appear continuous as shown in the "before" selection panel on the left side of the figure. With selection, the mean tolerance will shift upward and the variation about this mean will narrow. With tolerance determined by a single gene (right side), the distribution of genotypes among homozygous for intolerance (tt), ance allele (T). In this illustration, the T allele is dominant to the t allele. (Modified from Figure 1 of Mulvey, M. and S.A. Diamond, in *Metal Ecotoxicology: Concepts and Applications,* Lewis Publishers, Chelsea, Michigan, 1991.)

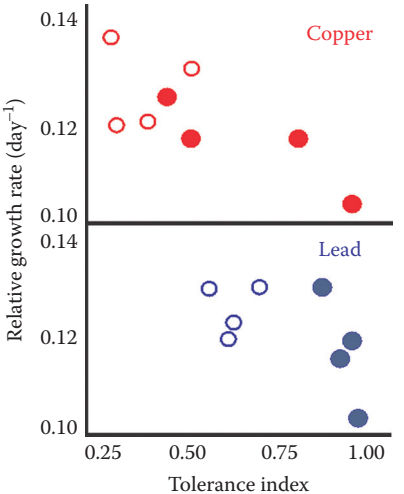

Figure 10.13 The cost in terms of growth rate for plant (*Agrostis capillaris*) strains with varying degrees of heavy metal tolerance. Plants were taken from reference locations (open circles) and areas with long histories of heavy metal mining in Wales (closed circles). Growth was measured in near-optimal media with heavy metal concentrations below those causing stress. Tolerance was measured as [2 (root length in heavy metal solution)]/[root length in a heavy metal solution + root length in a control solution]. Plants adapted to high metal concentrations (high-tolerance index) had generally slower growth under ideal conditions than nontolerant strains, indicating a trade-off associated with tolerance. (Modified from Figures 1 and 2 of Wilson, J.B., *Evolution,* 42, 408–413, 1988.)

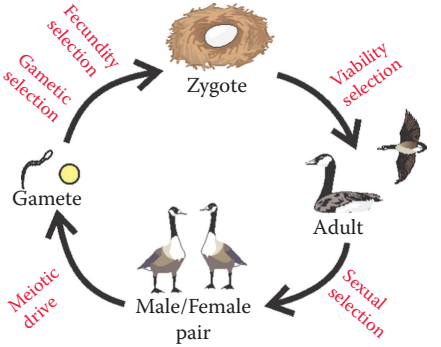

Figure 10.14 Components of the life cycle of an individual in which natural selection (selection components) can occur. Although rarely considered, selection components can be acted upon by contaminants. Please see the text for a detailed explanation.

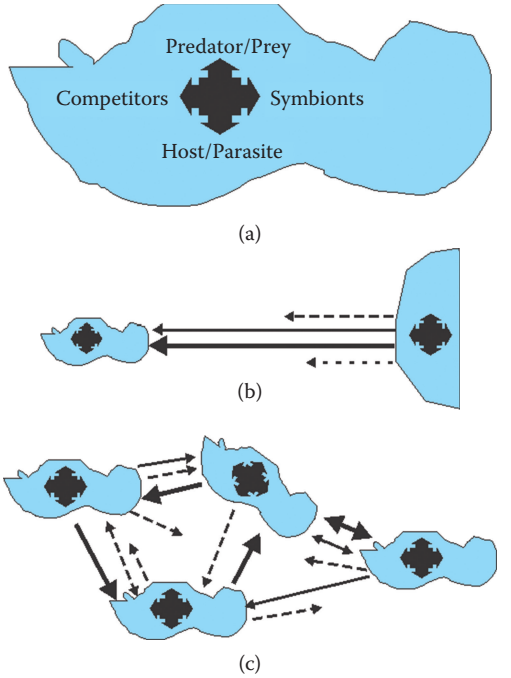

Figure 11.1 The metacommunity context includes species interactions and species migration dynamics among communities. Classic community ecology emphasizes species interactions such as those shown as (a) in influencing community structure and function. Classic MacArthur–Wilson theory emphasizes the likelihood of individuals of different species establishing or disappearing from an area such as a physical island (b). Metacommunity ecology combines both interspecies interactions and movements in a network of communities to suggest influence on structure and function (c).

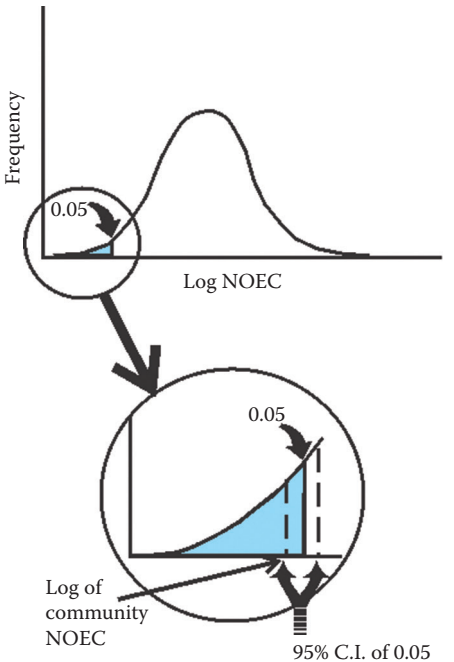

Figure 11.2 A pragmatic method of estimating a community-level NOEC. The 5% quantile is used to estimate the log concentration at which all but 5% of species would be protected. The concentration corresponding to the 5% quantile or the upper limit of the 95% confidence interval around this estimate could be used as the community-level no observed effect concentration. (From Van Straalen, N. M. and Denneman, C. A., *Ecotox. Environ. Safe.*, 18, 241–251, 1989; Wagner, C. and Løkke, H., *Water Res.*, 25, 1237–1242, 1991.)

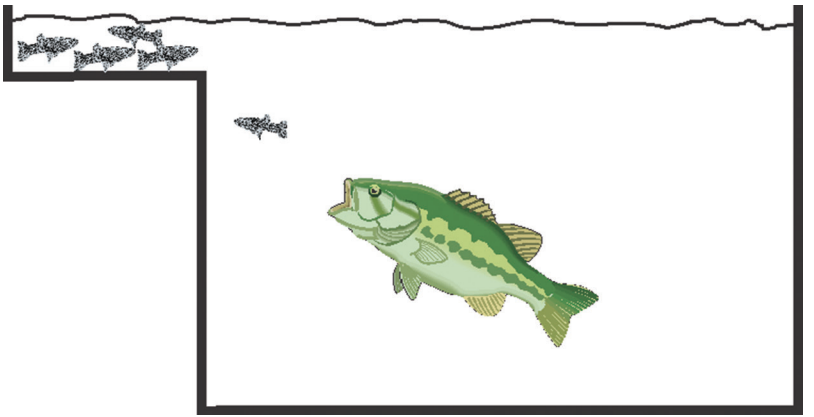

Figure 11.3 Experimental arena used to measure the effect of radiation (Goodyear, 1972) or inorganic mercury (Kania and O'Hara, 1974) on mosquitofish avoidance of predation by largemouth bass. The stressors diminished the ability of the mosquitofish to avoid predation by remaining in a shallow refuge.

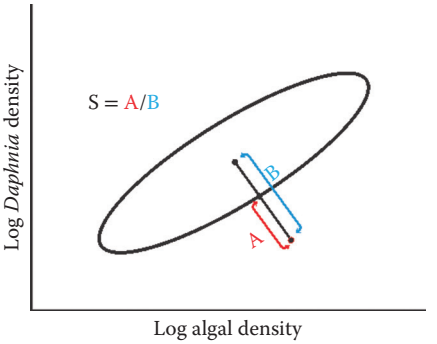

Figure 11.4 Calculation of normalized ecosystem strain as described by Kersting (1984). Strain is equal to A/B in this diagram. Ecosystem strain is measured relative to the normal behavior of the system as reflected by the 95% tolerance ellipse. These particular dimensions may be replaced by variables other than algal and grazing *Daphnia* densities. (Modified from Figure 4 in Kersting, K., *Ecol. Bull.*, 36, 150–153, 1984.)

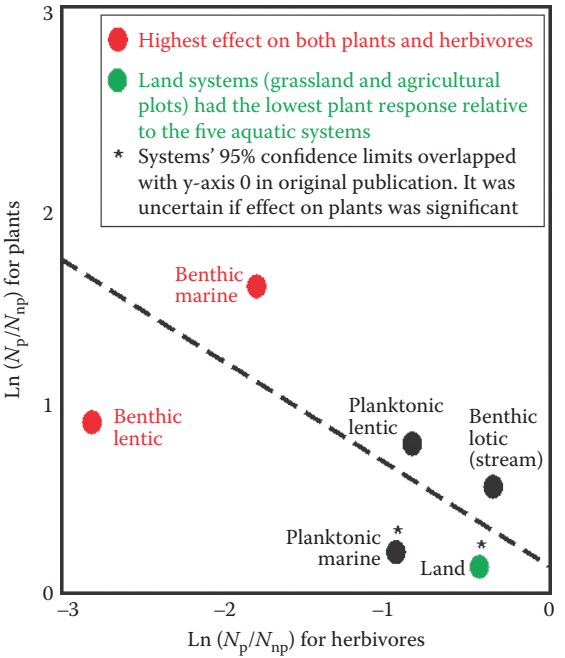

Figure 11.5 The influence of predator presence on plant biomass was expressed as the natural logarithm of the ratio of amount of biomass with (N_p) and without (N_{np}) the predator being present, ln (N_p/N_{np}). The same was calculated for herbivore biomass or density with and without the predator being present. Primary producers were periphyton (benthic lentic and stream), macroalgae (benthic marine), or grasses and forbs (land). Logarithm of quotients are plotted here for plants (*y* axis) versus herbivores (*x* axis). No predator influence of plant or herbivore biomass would be suggested if a point was 0 on the appropriate axis. The line passing through the points would have a slope of –1 if the influence was the same for plants and herbivores. The slope is actually shallower than –1. (Derived from Figure 1 in Shurin et al. *Ecol. Lett.*, 5, 785–791, 2002.)

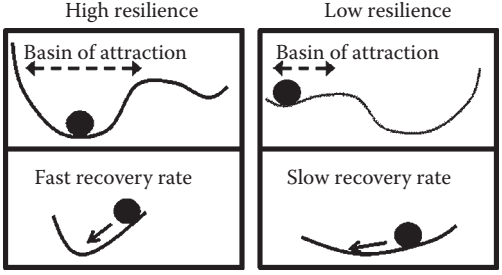

Figure 11.6 The relationship between resilience and recovery rate in communities. Size of the basin of attraction is a measure of the amount of disturbance a community can withstand before shifting to an alternative stable state. Communities recovering from previous exposure to contaminants generally will have a shallower basin of attraction compared to reference communities. (Modified from Van Nes, E. H. and Scheffer, M., *Am. Nat.*, 169, 738–747, 2007.)

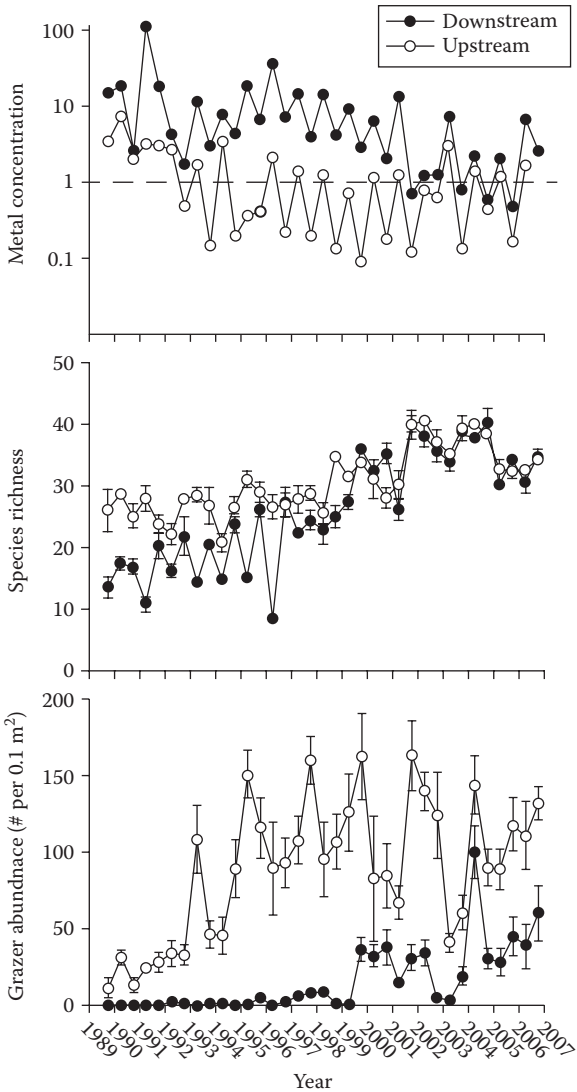

Figure 11.7 Long-term (1989–2006) changes in heavy metals, species richness and abundance of metal-sensitive grazers in the Arkansas River, CO. Horizontal line in upper panel is the U.S. EPA estimated safe metal concentration for Colorado streams.

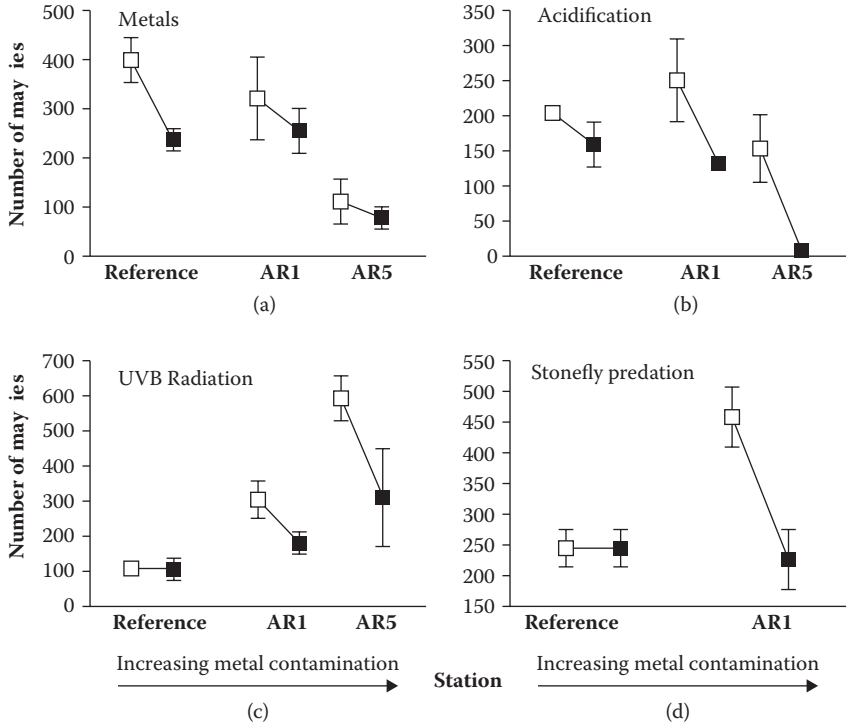

Figure 11.8 Results of stream mesocosm experiments showing effects of heavy metals (a), acidification (b), UVB radiation (c), and stonefly predation (d) on mayflies collected along a gradient of metal contamination. Results in each panel show abundance of mayflies in control (open symbols) and treated (closed symbols) mesocosms. The slope of each line reflects the relative impact of each perturbation.

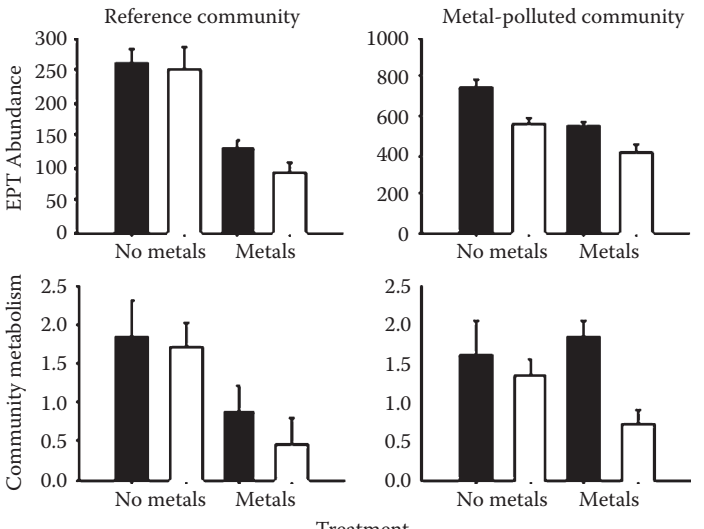

Figure 11.9 Individual and combined effects of metals and UVB on the total abundance of EPT organisms and community metabolism in stream mesocosms. Experiments were conducted using benthic communities collected from a reference site (left) and a metal-impacted site (right) in the Arkansas River watershed.

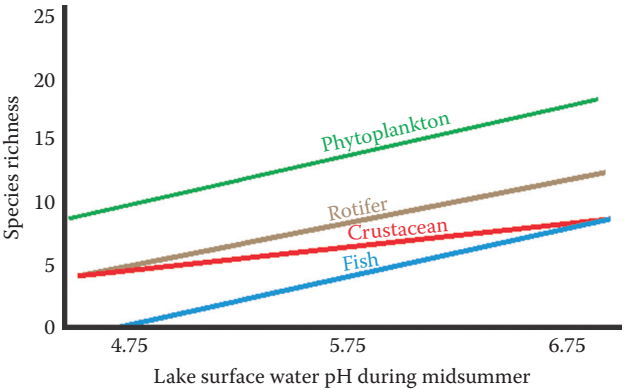

Figure 11.10 Species richness measured for 30 Adirondack lakes (New York) impacted to different degrees by acid precipitation. The lines show the general trends for phytoplankton, zooplankton rotifer, crustacean, and fish species from these lakes (lines from selected panels of Figure 1 of Nierzwicki-Bauer et al. [2010]). Clearly, lowered pH results in lowered species richness including the absence of fish in several low pH lakes.

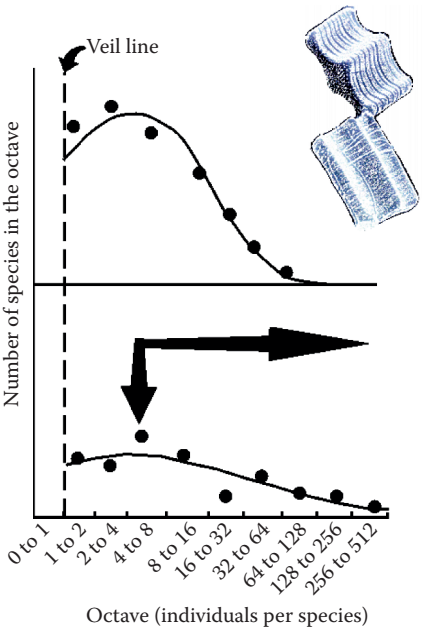

Figure 11.11 Species abundance curves (log normal model) before (top panel) and after (bottom panel) toxicant exposure. Note the transition from a common log normal distribution to a curve with a lowered mode and extended right tail. May (1976a) suggests that such a transition may reflect a reversion to an earlier successional stage when interspecies interactions were less important in shaping community species structure (i.e., away from the importance of species interactions toward an r-selection strategy).

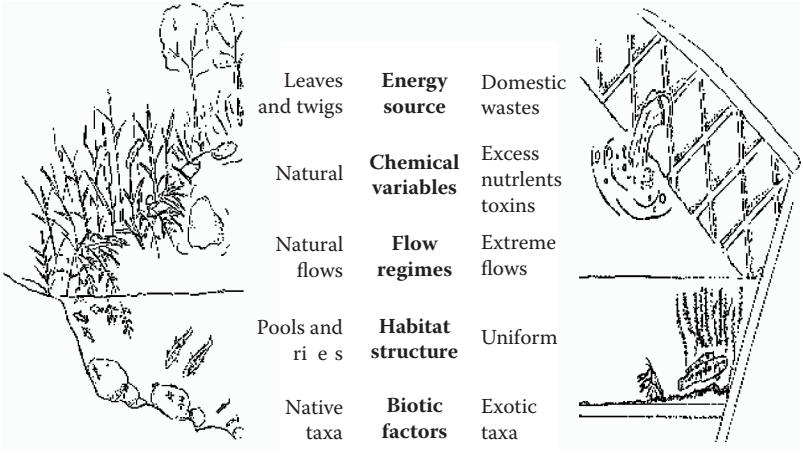

Figure 11.12 Five principle features, with examples, that determine river health. Left, a natural river; right, a modified river. (From Karr, J. R. and Rossano, E. M., *Ecol. Civil Eng.*, 4, 3–18, 2001.)

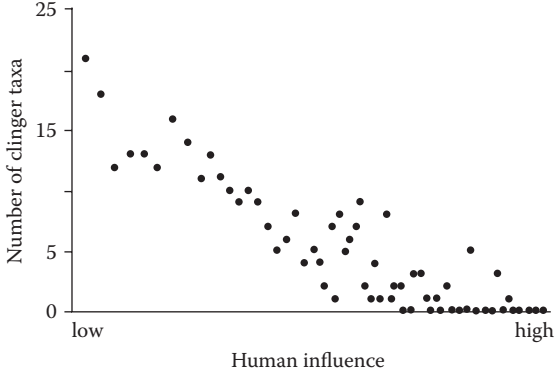

Figure 11.13 Dose-response curve for taxa richness of clingers—benthic invertebrates that cling to rocks enabling them to live in the interstitial spaces between rocks—in standard samples from 65 Japanese streams ranked according to intensity of human influence. (From Karr, J. R. and Chu, E. W., *Restoring Life in Running Waters: Better Biological Monitoring,* Island Press, Washington, DC, 1999.)

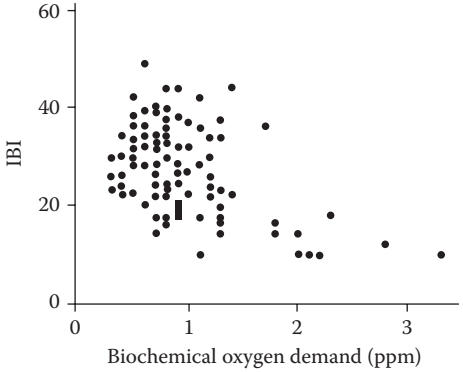

Figure 11.14 Index of biological integrity (IBI) compared with biochemical oxygen demand (BOD) for 100 sites from nine watersheds in Chugoku district, Japan. (From Karr, J. R. and Rossano, E. M., *Ecol. Civil Eng.*, 4, 3–18, 2001.)

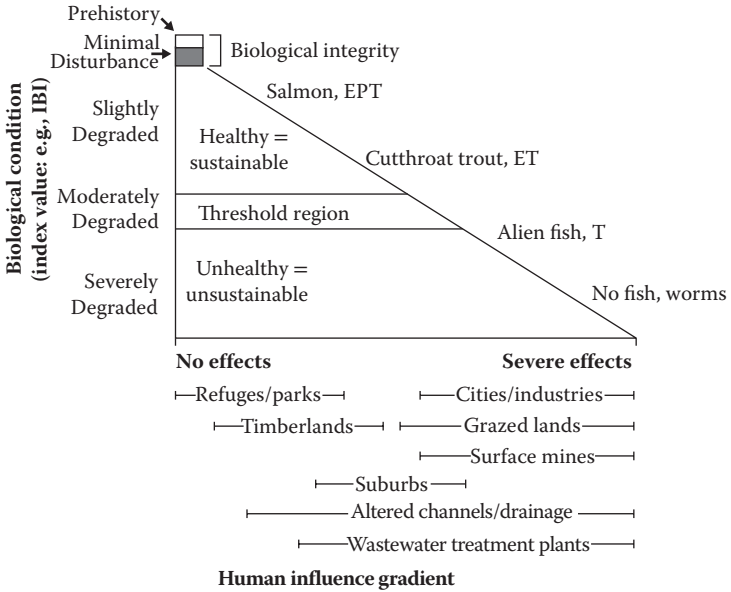

Figure 11.15 Relationship between biological condition and a hypothetical, multimetric measure of human activity, with examples. Different human activities result in biological changes such as different dominant organisms along a descending slope of biological condition. (Modified after Karr in Pimentel, D. et al. *Ecological Integrity: Integrating Environment, Conservation, and Health*, Washington, DC, Island Press, 2000.)

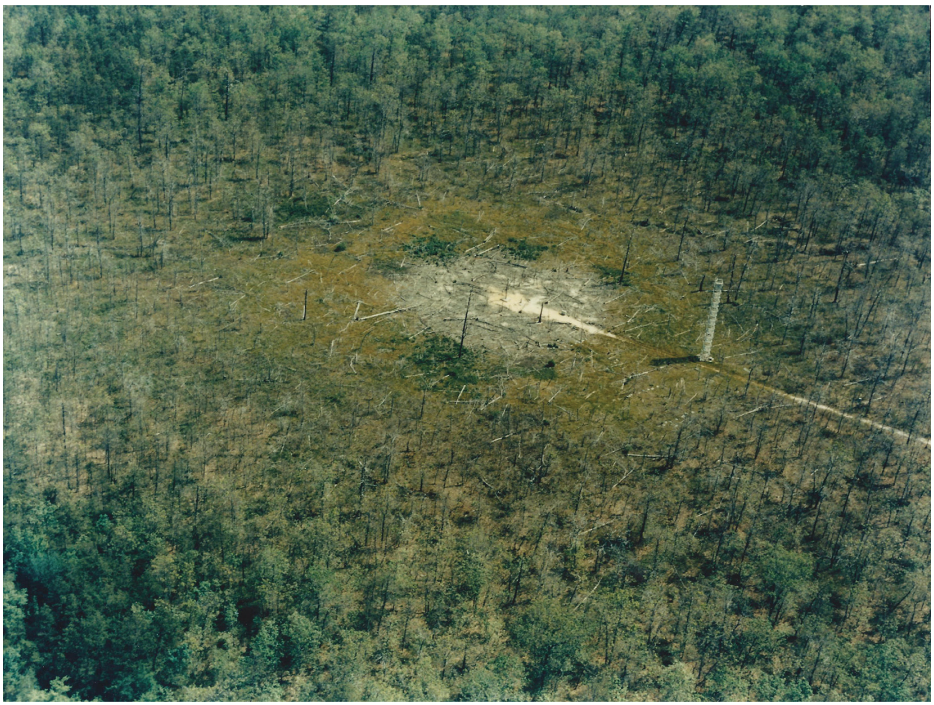

Figure 11.16 The Biology Gamma Forest at the Brookhaven National Laboratory (Long Island, New York) as it appeared in 1964. This eastern deciduous forest, which was dominated by white oak, scarlet oak, and pitch pine, was exposed to 9500 Ci of ^{137}Cs for approximately 6 months, beginning in 1961 (Woodwell, 1962, 1963). The radiation source was drawn up remotely from inside an underground pipe to expose the woodland. Exposure was many thousand roentgens at this γ source (center of barren spot) and decreased inversely with distance from the source. Zones composed of species of different tolerances ringed the source. Pitch pine (*Pinus rigida*) was the most sensitive with death occurring at 20 r day^{-1}. At the other extreme, sedge (*Carex pensylvanica*) was the most tolerant, surviving 350 r day^{-1}. (Courtesy of Brookhaven National Laboratory.)

Figure 11.17 Two types of mesocosms used to study fate and effects of contaminants. The top panel shows the indoor mesocosms of the Procter & Gamble Company's experimental streams facility (ESF). This system has the great advantage of more control over conditions (e.g., light and temperature) than normally afforded by outside mesocosms. Eight 12 m long channels allow replication of treatments and production of exposure concentration gradients. The top (head) section of each stream is paved with clay tiles for colonization by algae and microorganisms. Trays of gravel and sand are placed downstream of the tiles and afford substrate for invertebrates. (Courtesy Mr. John Bowling of Procter & Gamble, Co.) The bottom panel shows several outdoor, pond mesocosms used in similar fashion for examining pollutant effects. (Courtesy of Dr. Thomas La Point, North Texas University.)

Figure 11.18 Whole lake or split lake studies such as shown here afford *in situ* but expensive information on responses of aquatic communities to anthropogenic materials. Although not associated with a conventional toxicant, this particular split lake study of nutrient enrichment (Canadian experimental Lake 226: P, N, and C added to the bottom section and only N and C added to the top section of the lake) clearly shows the phytoplankton community response to an ecotoxicant. (Courtesy of Dr. Ken Mills.)

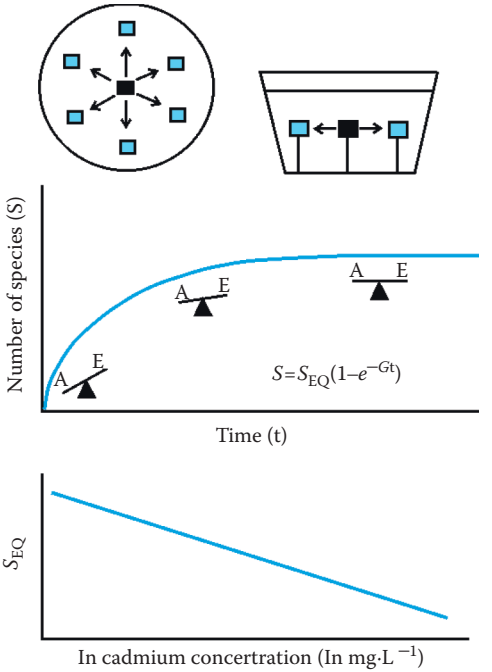

Figure 11.19 The protozoan community colonization assay developed by Cairns and coworkers (e.g., Niederlehner et al. 1985; Cairns et al. 1986). A polyurethane foam substrate (black square in top diagram) is allowed to accumulate species in a natural stream and then brought to the laboratory to serve as a source or epicenter for colonization of other, uncolonized foam substrates (blue squares in top diagram). The dynamics of species colonization on foam substrates is measured using the MacArthur–Wilson model for island colonization (center plot). This is done with substrates submersed in containers filled with different concentrations of toxicant (bottom plot) to determine the effect of toxicants on the process. (Modified from Figures 1, 2, and 4 in Cairns et al. *Environ. Monit. Assess.*, 6, 207–220, 1986.)

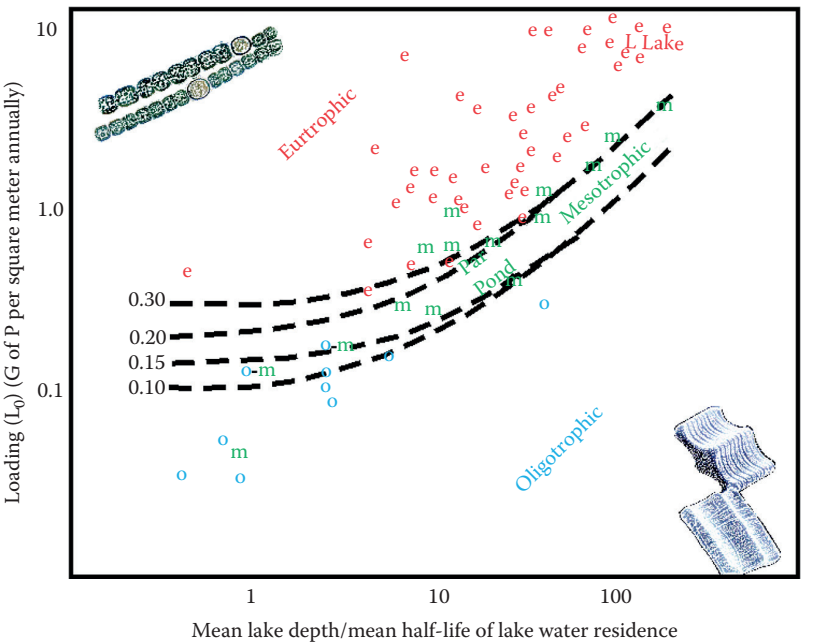

Figure 11.20 A simple Vollenweider plot of a series of European and U.S. water bodies using phosphorus loading and hydrology metrics. Lentic systems that were eutrophic, mesotrophic, or oligotrophic were coded as such with colored e, m, and o, respectively. Those transitional between mesotrophic and oligotrophic are depicted with an o-m. The position for Par Pond (recirculating cooling lake) and then-planned L Lake (once-through cooling lake) are also shown. Lines depicting the general trends for lakes with phosphorus loadings of 0.10, 0.15, 0.20, and 0.3 are also shown to suggest zones of transition between oligotrophic, mesotrophic and eutrophic water bodies.

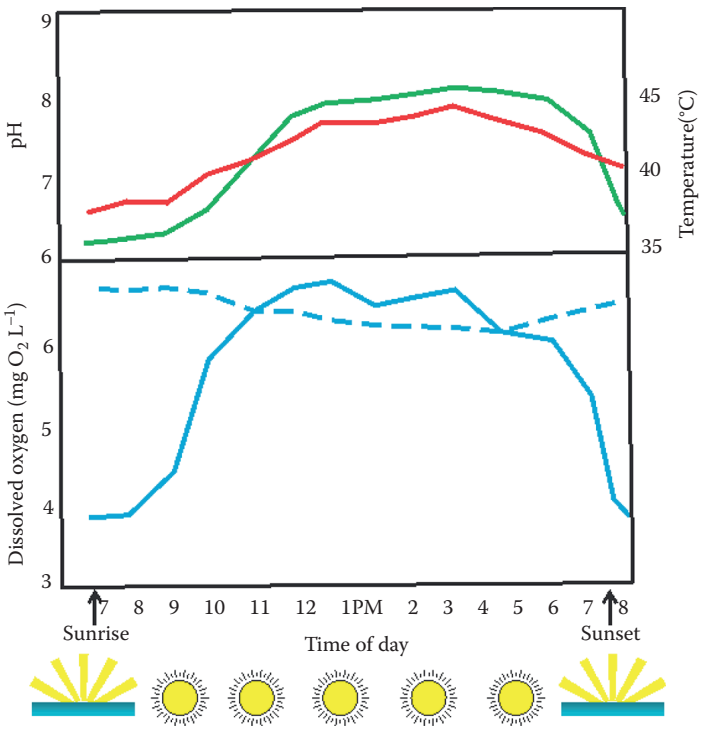

Figure 11.21 Daily shifts in water quality measured in a region of river swamp where the tree canopy had been removed due to past discharge of hot cooling waters (see lower photograph in Figure 2.35). The aquatic community shifted substantially with the destruction of the cypress and tupelo trees, and opening up of the canopy. On the day depicted here, warm nutrient-rich cooling water flowed over thick mats of blue-green algae (cyanobacteria) in this stream delta region of the swamp. The water temperature (red line) increased slightly and then decreased from dawn to dusk. Intense microfloral respiration had drawn dissolved oxygen concentrations (solid blue line) down to approximately 4 mg·L^{-1} until dawn when microfloral photosynthesis rapidly raised it above dissolved oxygen saturation (dashed blue line). Small bubbles of oxygen appeared in the algal mat at the most productive time of day. Strong shifts in microfloral respiration and photosynthesis created wide shifts in water pH (green line). (Figure drawn from data in Newman (1986) unpublished report.)

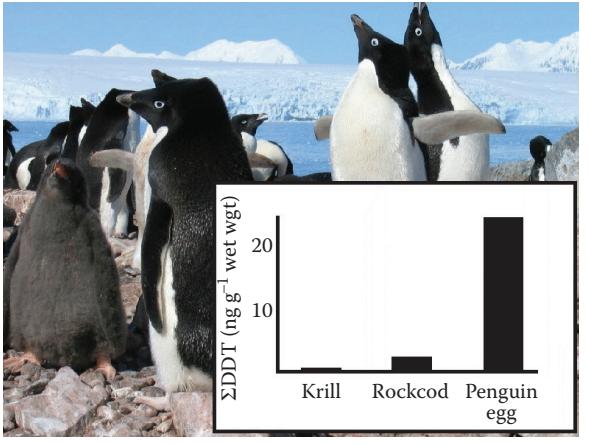

Figure 12.1 The accumulation of ΣDDT in Adelie penguin (*Pygoscelis adeliae*) eggs in the Antarctic. Diverse persistent organic pollutants (POPs) are found to accumulate to high levels in these and other polar species inhabiting regions distant from the use of the POPs, e.g., Bidleman et al. (1993), Kumar et al. (2002), Goerke et al. (2004), Vorkamp et al. (2004), and Corsolini et al. (2007). (Data from Table 1 of Corsolini, S. et al. *Environ. Pollut.*, 140, 371–382, 2006 and photograph courtesy of Heidi Geisz [College of William & Mary, VIMS]).

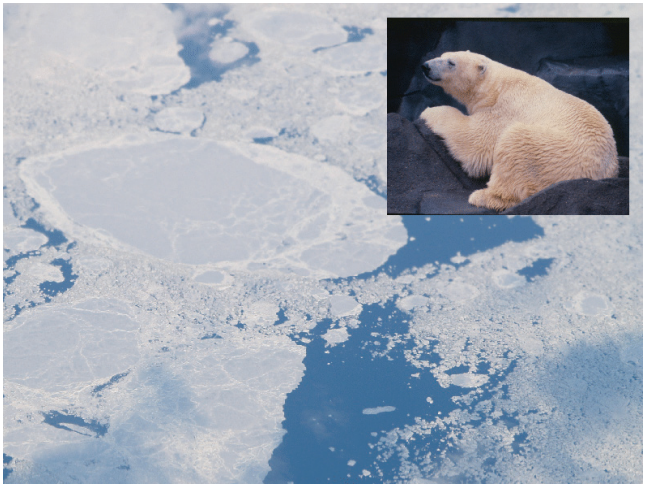

Figure 12.2 Pack ice in Ungava Bay of the Arctic Ocean (northeast Canada) as seen on July 1, 2007 during a historically thin summer polar ice condition. Pack ice melt is normally slow until mid-July when it accelerates in this part of the Arctic Ocean. Feeding by polar bears on seals is strongly influenced by pack ice dynamics. Scientist and Native American Inuit groups have begun to focus on potential impacts of global warming trends on the persistence of polar bear populations (Derocher et al. 2004; Wiig, 2005; Stirling and Parkinson, 2006). Some predictions indicate the potential for substantial thinning (Bluhm and Gradinger, 2008; Walsh, 2008) or even complete disappearance of summer ice (Kerr, 2007; Serreze et al. 2007; Stroeve et al. 2007). Like the penguins shown in Figure 12.1, polar bears can accumulate high concentrations of POPs (Kumar et al. 2002), which suggests a complex situation that exists for polar bears at this time. (Both photographs taken by M. C. Newman.)

Figure 12.3 In the top photograph, landscape modification by smelting and mining activities in Copperhill, Tennessee, is shown. Copperhill is situated in the Blue Ridge Mountains at the convergence of northern Georgia, western North Carolina, and southern Tennessee. The Ducktown Mining District began smelting circa 1854, and rapidly developed during the next four decades. Sulfuric acid and sulfur dioxide releases were greatly reduced after 1910. Tree growth, as measured from growth rings, was slowed from 1863 to 1912 in the nearby Great Smoky Mountains National Park (88 km upwind) because of the emissions from smelting (Baes and McLaughlin, 1984). This photograph was taken more than 70 years after emission reductions occurred (1982) and shows a desert-like landscape instead of the typical, forested landscape. In the bottom photograph, a similar situation is shown for the Mount Lyell copper mines and smelters near Queenstown, Tasmania. The Mount Lyell Mining and Railway Company began operations in 1893. Smelting ended in 1969, 39 years before this photograph was taken. (Photographs by M. C. Newman)

Figure 12.4 The Trans-Alaska Oil Pipeline as it passes across the taiga, a transitional community between the tundra and boreal forest communities. (Photograph by M. C. Newman)

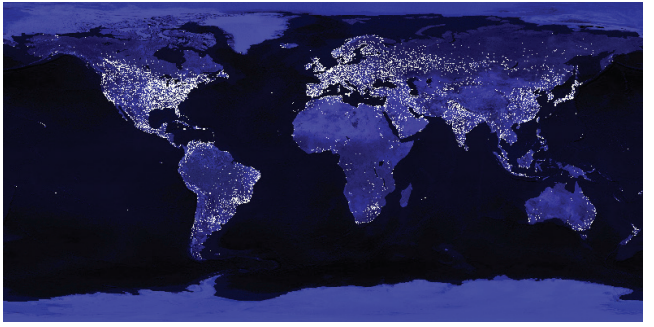

Figure 12.5 The global pattern of night lights visualized by compositing two hundred Defense Meteorological Satellite Program (DMSP) images (http://antwrp.gsfc.nasa.gov/apod/earth.html). (Courtesy of NASA, C. Mayhew and R. Simmon (NASA/GSFC), NOAA/NGDC, DMSP Digital Archive)

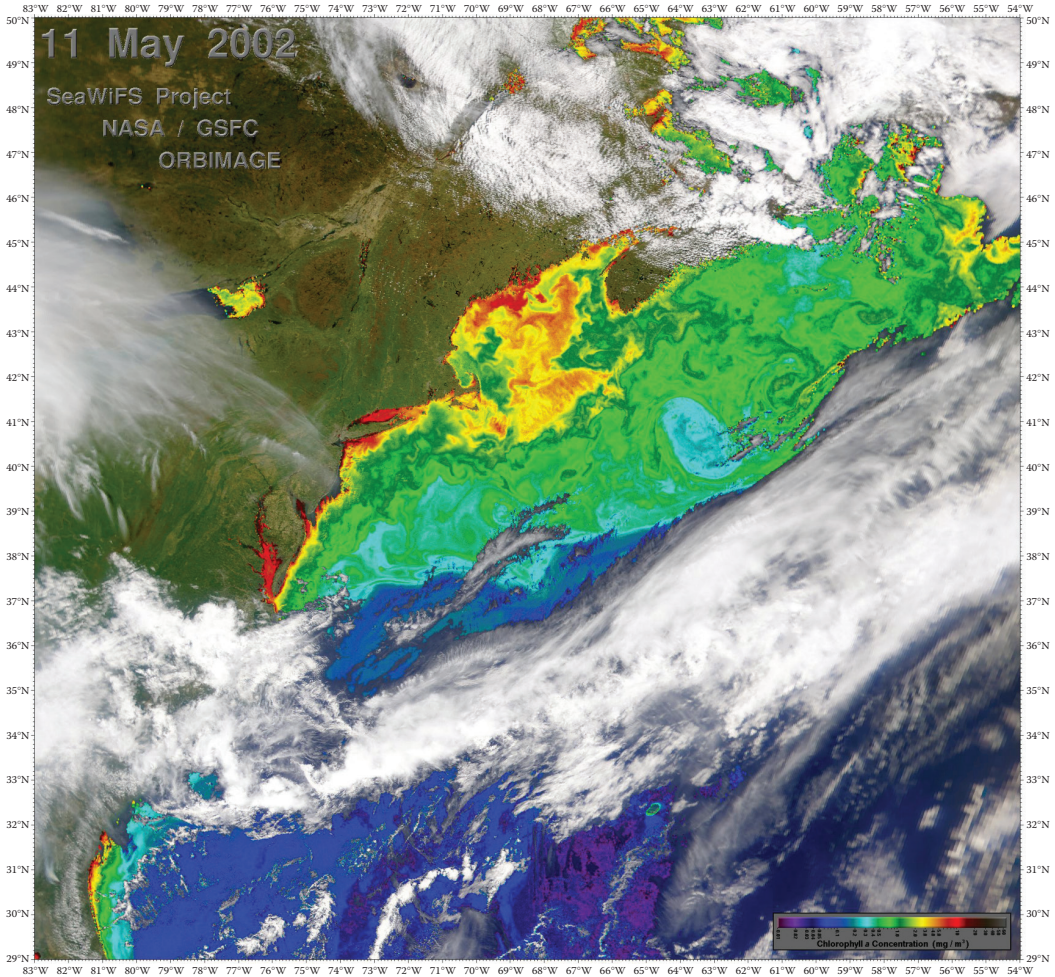

Figure 12.6 Chlorophyll (mg·M^{-3}) off the heavily developed east coast of the United States showing clearly high coastal productivity (e.g., red and orange reflect areas of approximately 10–50 and 2–10 mg·M^{-3}) with productivity being lowest offshore (blue areas have approximately 0.01–0.05 mg·M^{-3} of chlorophyll). Intermediate productivity areas of yellow (yellow areas are approximately 0.5–2 mg·M^{-3} of chlorophyll) to green are obvious as regions of mixing between the nutrient enriched coastal waters and the waters of the Gulf Stream. A low chlorophyll gyre is seen in this image as a mass of Gulf Stream water spun off into the more productive waters. Although increased nutrient-driven productivity is shown here only for a small area of the ocean, increased nutrient inputs to the world's oceans have produced a global crisis in which large expanses of the oceans called "dead zones" are experiencing chronic hypoxia (Diaz, 2001; Diaz and Rosenberg, 2008). (Courtesy of NASA SeaWiF Project, NASA/Goddard Space Flight Center and ORBIMAGE.)

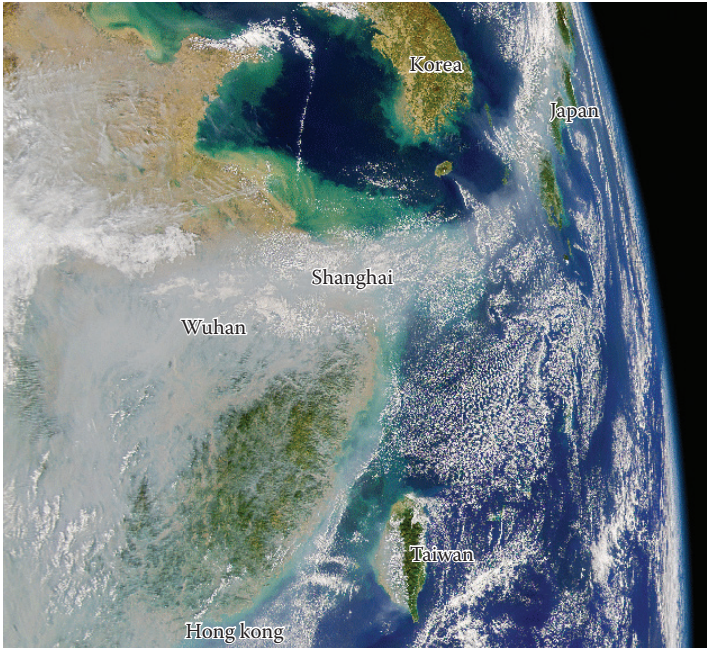

Figure 12.7 A mass of haze is seen in this SEAWiF image that originates in eastern China, passes over the large cities of Wuhan and Shanghai, and then between South Korea and Japan. The rapid industrial development of China that depends heavily on coal burning produces such a visible bank of aerosol haze as well as sulfur dioxide that is not confined by national borders. (Courtesy of NASA SeaWiF Project, NASA/Goddard Space Flight Center and ORBIMAGE.)

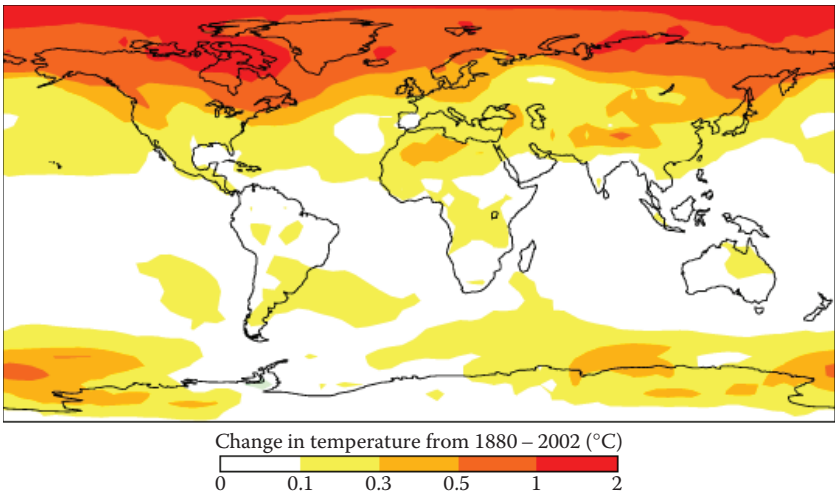

Figure 12.8 NASA estimation of the amount of the total increase in temperature that can be attributed to increases in soot generation globally. The period over which the change is calculated is 1880 to 2002. (Courtesy of NASA Goddard Institute of Space Studies.)

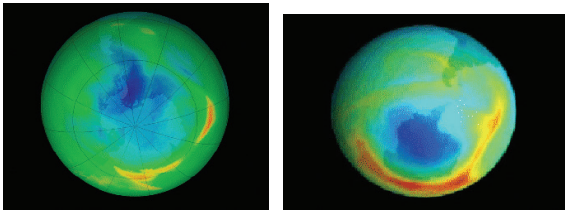

Figure 12.9 The Antarctic ozone hole as generated from data taken from August/September 1979, 1981, 2006, and 2012, showing the emergence of a hole extending outward to cover approximately 20 million square kilometers of the earth's surface. The hole reached its maximum size (26.6 million square kilometers) in 2006 and seems to have stabilized, notionally because of the Montreal Protocol. (Courtesy of NASA/Goddard Space Flight Scientific Visualization Studio. See http://www.nasa.gov/earth/lookingatearth/ozone_record.html and other related NASA webpages)

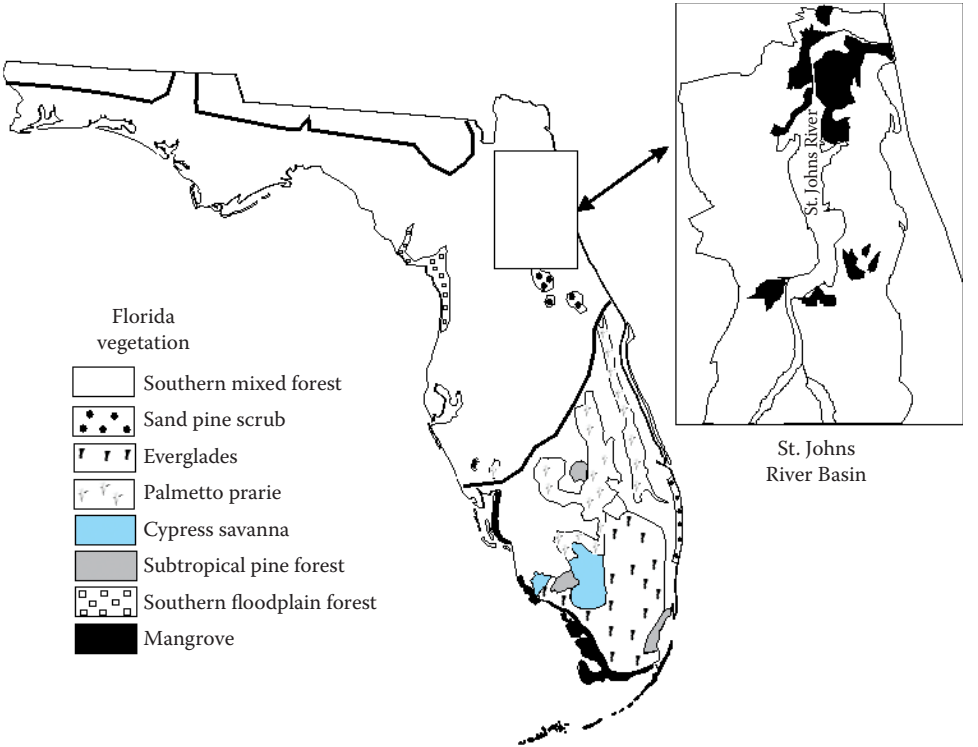

Figure 12.10 Three scales (river basin, vegetation type, and Type II ecoregion) of consideration for Florida. (Modified by combining spatial data from Figure 5 of Adamus, C.L. and M.J. Bergman, *Water Resour. Bull.*, 31, 647–655, 1995; an ecoregion map from Omernik, J.M., *Ann. Assoc. Am. Geogr.*, 77, 118–125, 1987; and a U.S. Geological Survey vegetation map [Sheet 90].)

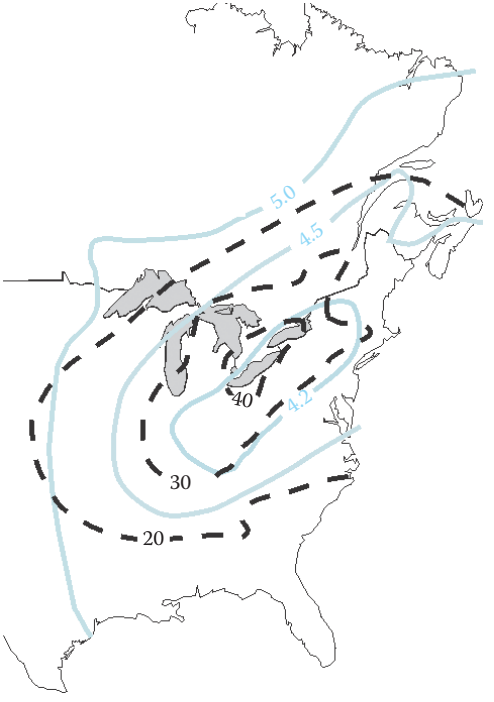

Figure 12.11 The pH (solid blue lines and numbers) and sulfate ion concentration ($\mu m \cdot L^{-1}$) (dashed black lines and open numbers) in precipitation measured in 1980. In general, pH and sulfate contours coincide with the spatial pattern of sulfur dioxide emissions reported by a joint U.S./Canadian working group. (Modified from Figures 2 and 3 of Barrie, L.A. and J.M. Hales, *Tellus*, 36B, 333–335, 1984.)

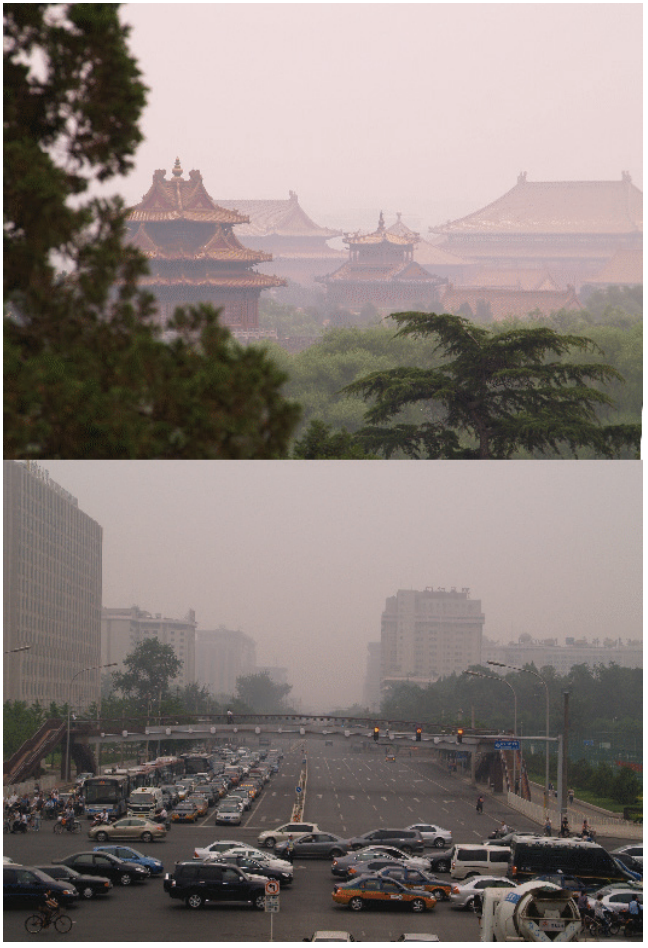

Figure 12.12 Intense air pollution in Beijing, People's Republic of China. The upper photograph of Beijing's Forbidden City was taken at 1:00 PM in the afternoon on June 11, 2010 from Beihai Gongyuan. These ancient buildings sit in a haze generated by automobile exhaust. If the air pollution was not present, the modern Beijing cityscape would be visible, filling the entire background of the photograph. The lower, street-level photograph showing the haze and automobile sources was taken 2 hours later at a busy Beijing intersection. (Photographs by M. C. Newman.)

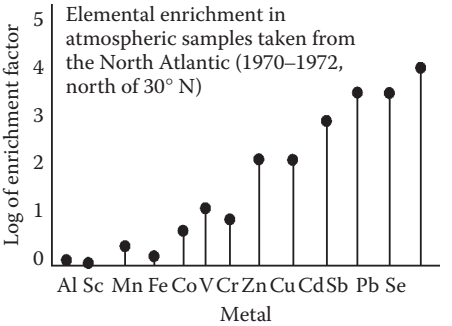

Figure 12.13 Metal particulate dispersal over the remote north Atlantic Ocean as evidenced by increased enrichment factors. The **enrichment factor** (EF_{crust}) for an element is its concentration (X) measured in air samples divided by that expected in the earth's crust: $EF_{crust} = [X/Al]_{air}/[X/Al]_{crust}$. Both air and crustal concentrations are normalized to aluminum concentrations. Aluminum is a ubiquitous element comprising about 8% of crustal material. Increases in EF_{crust} above 10^0 (= 1) imply enrichment from anthropogenic sources. (Modified from Figure 1 of Duce, R.A. and W.H. Zoller, *Science*, 187, 59–61, 1975. With permission.)

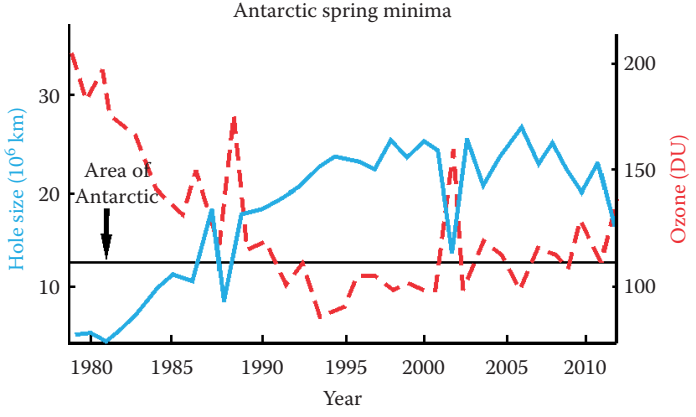

Figure 12.14 The increase in and then leveling off of the size of the Antarctic ozone hole (blue line) and also decrease in spring minima ozone concentration (red line). Ozone concentrations are expressed in **Dobson units (DU)**. One DU is the equivalent of 0.001 mm thickness of pure ozone at 1 atmosphere. To give some scale to this unit, if all of the ozone in the atmosphere were to be brought down to form a pure layer of ozone at sea level, it would be 3 mm thick (Bunce, 1991). (Data from NASA, http://ozonewatch.gsfc.nasa.gov/meteorology/ytd_data.txt.)

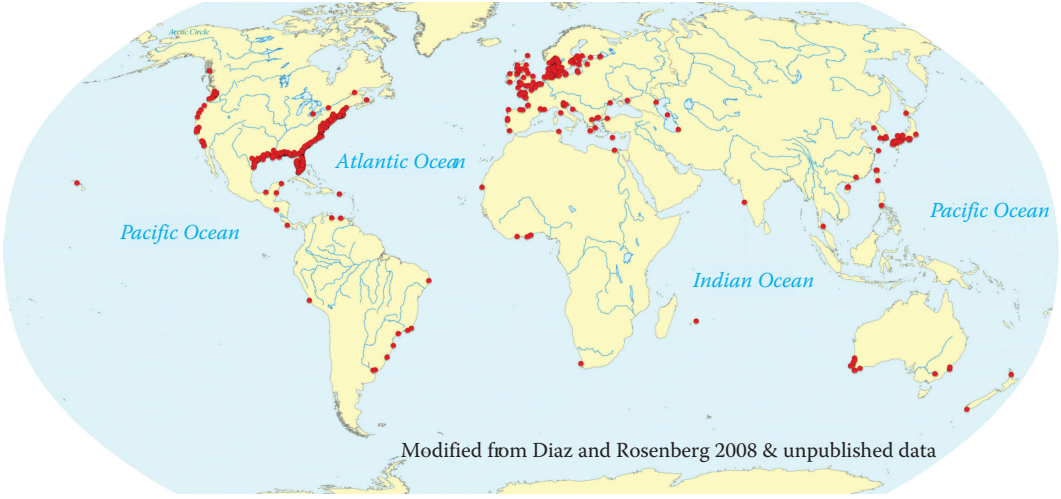

Figure 12.15 The global distribution of cultural eutrophication-associated anoxic dead zones reported in the literature by the end of 2008. This figure is an updated rendering of similar data shown in Figure 1 of Diaz and Rosenberg (2008) that correlated the spatial distribution of dead zones with that of human influence (i.e., the human "footprint") across the globe. (Courtesy of Robert Diaz, Virginia Institute of Marine Science, College of William & Mary, Virginia.)

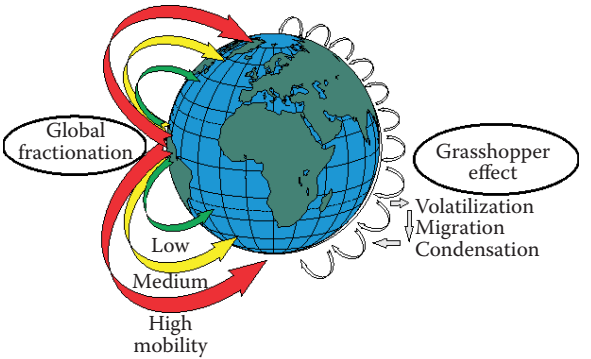

Figure 12.16 The movement of persistent organic pollutants on a global scale. (Modified from Figure 1 of Wania, F. and D. Mackay, *Environ. Sci. Technol.*, 30, 390A–396A, 1996. With permission.)

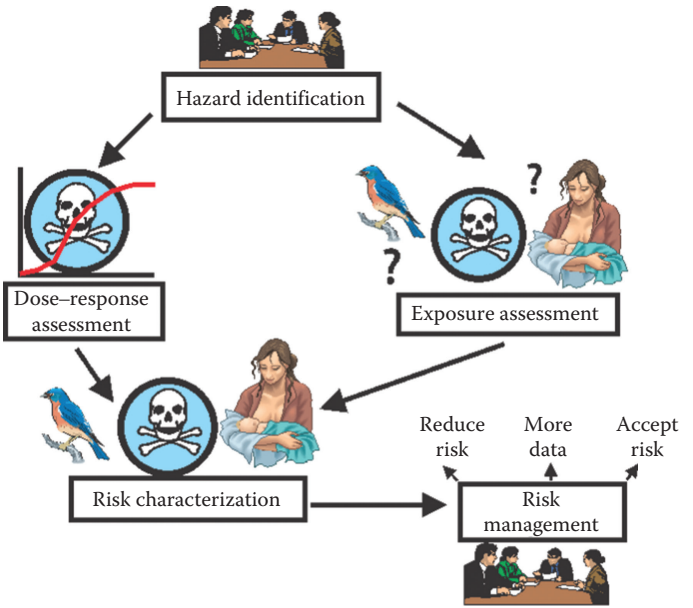

Figure 13.1 The National Academy of Science paradigm for risk assessment. The risk assessor identifies the hazard, assesses the potential for exposure (or current exposure) and the dose–response relationship for the relevant entities being protected and the relevant toxicants. This information is integrated to characterize the risk. At that point, the assessment is provided to the risk manager who then decides to accept or reduce the associated risk or, if insufficient information is available to make a good decision, to seek out more information.

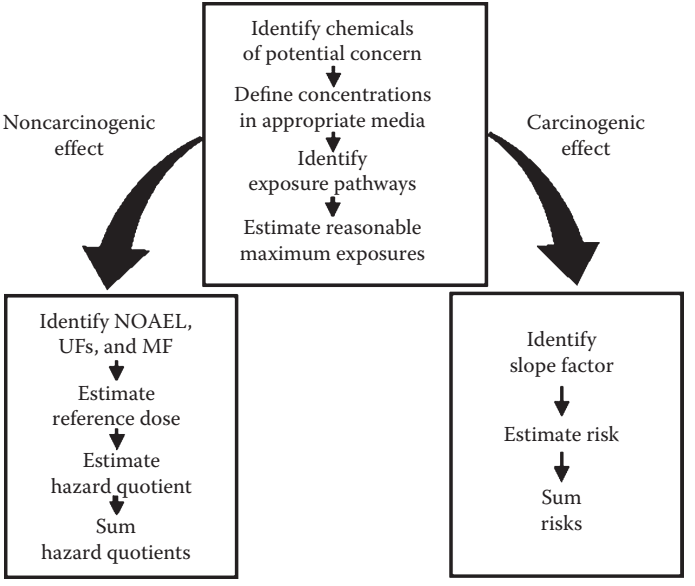

Figure 13.2 The general sequence of steps toward assessment the hazard/risk associated with noncarcinogenic and carcinogenic effects of contaminants. The final step of summing hazard quotients or risks for the individual chemicals or media may not be required or may not be appropriate (see text for more details).

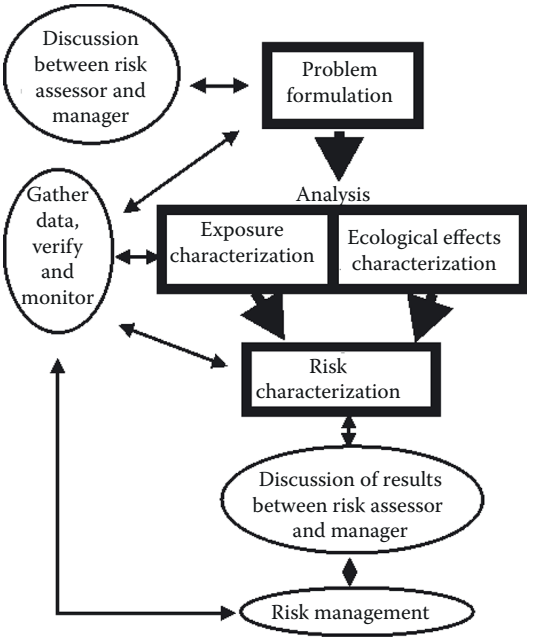

Figure 13.3 The general framework of an ecological risk assessment. The boxes and thick arrows reflect the risk assessment proper and is similar to the National Academy of Science paradigm (Figure 13.1). The narrow, two-way arrows reflect interactions between the risk assessor and the risk manager during the process. They also reflect the continual accrual and evaluation of information during the entire process. (Modified from Figure 2 in EPA, *Review Draft*, p. 564, 1994.)

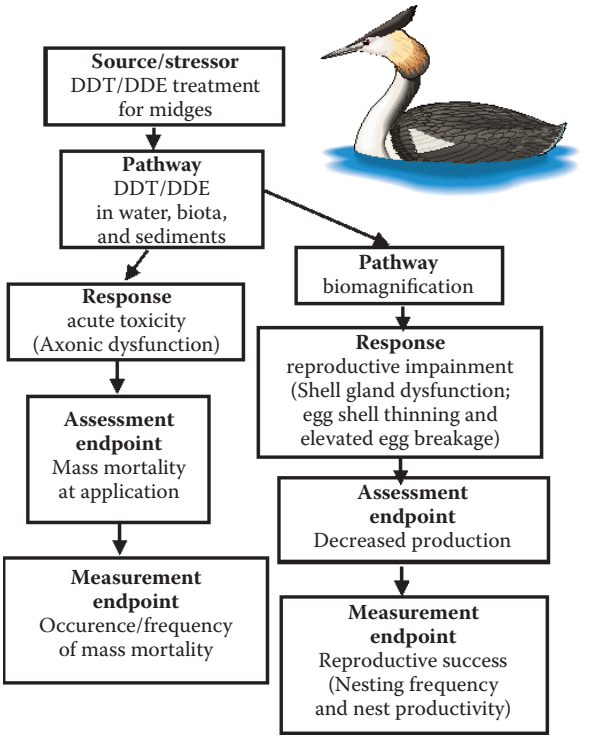

Figure 13.4 A conceptual model diagram for the pesticide spraying of nonbiting midges as described in Chapter 1 and depicted in Figure 1.2. Here, the assessment and measurement endpoints are separated for clarity. They could have been combined as the assessment endpoint. The valued ecological entity is the Western Grebe population.

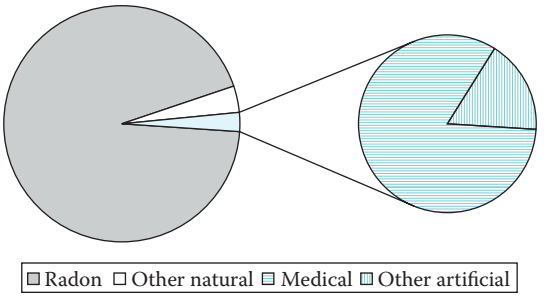

Figure 13.5 The estimated annual dose equivalent of ionizing radiations received by humans. (Data from Table 18.2 of Cockerham et al. [2008].) Most of the average annual dose equivalent is from radon (24.0 mSv) with a modest amount of additional natural dose from cosmic rays (0.27 mSv), terrestrial sources (0.28 mSv), and internal sources (0.39 mSv) such as radiopotassium in the body. The dose equivalent from cosmic sources depends on elevation and the value given here is for 0–150 m above sea level (Cockerham et al. 2008). Annual effective dose from artificial sources (0.64 mSv) is composed primarily of medical diagnosis *x*-rays (0.39 mSv), consumer products (0.10 mSv), and nuclear medicine (0.14 mSv).

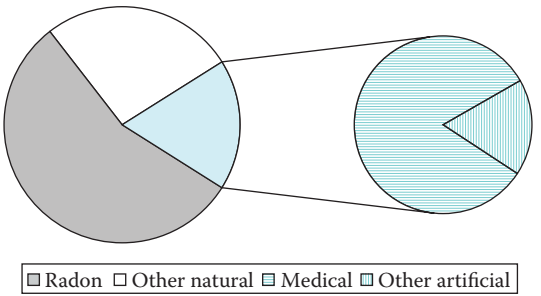

Figure 13.6 The expression of the doses shown in Figure 13.5 as effective dose equivalents. (Data from Table 18.2 of Cockerham et al. [2008].) Radon = 2.0 mSv, cosmic rays = 0.27 mSv, terrestrial sources = 0.28 mSv, natural internal = 0.39 mSv, medical *x*-rays = 0.39 mSv, nuclear medicines = 0.14 mSv, and consumer products = 0.10 mSv. Notice that radon (and its daughters) has an effective dose equivalent that accounts for a large portion of the human annual radiation dose. Radon's effective dose equivalent is different from its dose equivalent because its influence is heavily focused on pulmonary exposure.

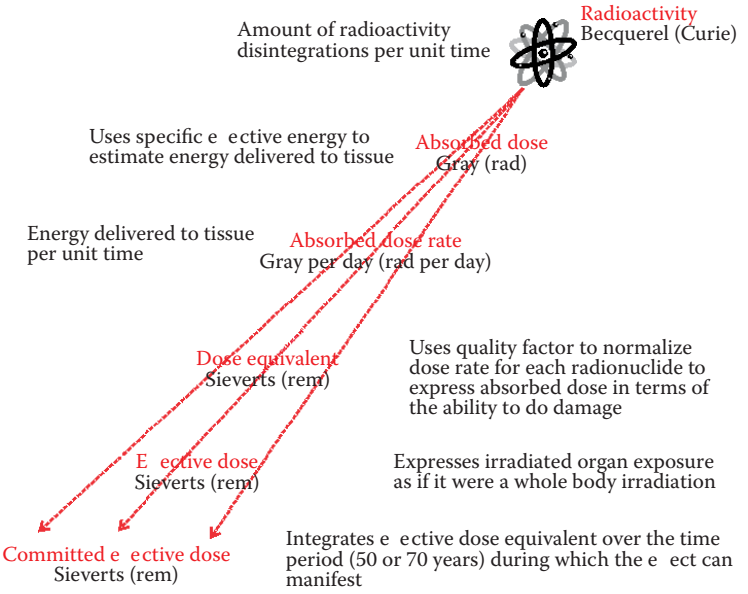

Figure 13.7 Summary of radiation dose and effect metrics. International System units are placed under each metric. Older, but still used, metrics are given in parentheses after the International System units (see text for details).